2005年8月 博士學位論文

초정밀가공기의 나노미터급 정밀도 향상을 위한 환경 및 운동오차 보상

郭 二 丘

2005年 8月
博士學位論文

초정밀 가공기의 나노미터급 정밀도 향상을 위한 환경 및 운동오차 보상

朝鮮大學校 大學院

精密機械工學科

郭　二　丘

초정밀 가공기의 나노미터급 정밀도 향상을 위한 환경 및 운동오차 보상

The Compensation of Environment
and Motion Error for nm Grade Accuracy Improvement
of Ultra Precision Turning Machine

2005年　　8月　　日

朝鮮大學校 大學院

精密機械工學科

郭　二　丘

초정밀 가공기의 나노미터급 정밀도 향상을 위한 환경 및 운동오차 보상

指導敎授 金 在 烈

論文을 工學博士學位 申請 論文으로 提出함.

2005年 4月

朝鮮大學校 大學院

精密機械工學科

郭 二 丘

郭二丘의 博士學位論文을 認准함.

委員長 朝鮮大學校 敎授 심 재 기

委員 朝鮮大學校 敎授 김 영 석

委員 木浦大學校 敎授 김 일 수

委員 韓國機械硏究員 博士 이 찬 홍

委員 朝鮮大學校 敎授 김 재 열

2005年 6月 日

朝鮮大學校 大學院

CONTENTS

LIST OF FIGURES ····· iv
LIST OF TABLES ····· vi
NOMENCLATURES ····· vii
ABSTRACT ····· ix

I. INTRODUCTION ····· 1
A. Motivation ····· 1
B. Objective and outline of this research ····· 5

II. LITERATURE SURVEY ····· 7
A. Review of related researches ····· 7
B. Domestic research trends ····· 9
C. International research trends ····· 11

III. THE ENVIRONMENTAL COMPENSATION OF THE OPTIC FIBER LASER ENCODER ····· 16
A. Principles of operation of the optical fiber laser encoder ····· 16
B. The system structure ····· 22
C. The environmental compensation of the optic fiber laser encoder ····· 24
D. The experiment for the environment error compensation ····· 29
E. Summary ····· 32

IV. THE STABILITY ANALYSIS OF UPCU USING A FEM ····· 33

A. Finite element formulation of 3-dimensional model ····· 33

1. Displacement function ····· 33

2. Strain matrix ····· 36

3. Elasticity matrix ····· 37

4. Stiffness, stress, and load matrices ····· 38

B. Compliance equations of flexure hinge ····· 39

1. In-of-plane compliance equations ····· 40

2. Out-of-plane compliance equations ····· 42

3. Precision of rotation ····· 43

4. Stress considerations ····· 44

C. Finite element modeling ····· 46

1. Mesh generation ····· 46

2. 3-dimensional Modeling ····· 47

3. The Measurement of three component cutting force ····· 49

D. Results and analysis of finite element interpretation ····· 50

1. Examination of stability depending on hinge type ····· 51

2. Examination of stability of micro stage depending on cutting force load ····· 55

3. Examination of stability depending on material change (Without PZT) ····· 58

4. Examination of stability depending on material change (Within PZT) ····· 61

E. Validity verification of stability analysis through an experiment ····· 64

F. Summary ····· 67

V. THE MACHINING PRECISION IMPROVEMENT DUE TO THE REAL-TIME COMPENSATION FOR THE MOTION ERROR BY UPCU ····· 68

A. The motion characteristics of the UPCU ····· 69

1. The motion error ····· 69

2. The driving mechanism of the UPCU ····· 75

B. The control algorithm ····· 79

C. The systematic structure and the error measurement ····· 81

D. The ultra-precision positioning performance of the UPCU ····· 84

E. The tracking error test for UPCU ····· 86

F. Summary ····· 89

VI. CONCLUSION ····· 90

REFERENCES ····· 92

APPENDIX A ····· 100

APPENDIX B ····· 105

LIST OF FIGURES

Fig. 3-1 Helium neon laser tube of laser encoder ····· 16

Fig. 3-2 Laser tube operation of laser encoder ····· 17

Fig. 3-3 Laser stabilisation and gain curve ····· 17

Fig. 3-4 Fibre optic coupling delivery of laser encoder ····· 18

Fig. 3-5 Basic principles of optical fibre beam delivery ····· 19

Fig. 3-6 Miniaturized homodyne(single frequency) interferometer ····· 20

Fig. 3-7 Homodyne(single frequency) interferometer ····· 20

Fig. 3-8 Laser feedback of optic fibre and components of environment compensation system ····· 23

Fig. 3-9 The data acquisition programing of laser optic fibre encoder ····· 23

Fig. 3-10 The environment for interferometry ····· 24

Fig. 3-11 The internal block diagram of environment compensation unit ····· 25

Fig. 3-12 A setting of laser encoder system ····· 30

Fig. 3-13 Zero point drift and temperature over time ····· 31

Fig. 3-14 Frequency stability comparison ····· 31

Fig. 4-1 A tetrahedral volume ····· 34

Fig. 4-2 Geometric configuration of a circular flexure hinge ····· 39

Fig. 4-3 Schematic representation of a flexure hinge with loading ····· 39

Fig. 4-4 FEM modeling of ultra-precision cutting unit ····· 48

Fig. 4-5 Cutting force of micro cutting machine ····· 49

Fig. 4-6 FEM analysis result of rectangular type (without PZT loading) ··· 53

Fig. 4-7 FEM analysis result of round type (without PZT loading) ····· 53

Fig. 4-8 FEM analysis result of rectangular (PZT loading) ····· 54

Fig. 4-9 FEM analysis result of round type. (PZT loading) ····· 54
Fig. 4-10 Deformation of rectangular type and round type ····· 57
Fig. 4-11 Max. shear stress distribution of micro stage ····· 60
Fig. 4-12 Displacement response of micro stage ····· 63
Fig. 4-13 Hysteresis curve of UPCU ····· 66
Fig. 4-14 The result of resolution experiment ····· 66
Fig. 5-1 Six motion error in a UPCU ····· 69
Fig. 5-2 Translational mapping ····· 70
Fig. 5-3 Basic flexure structure and its application
for 3- axis fine motion mechanism ····· 75
Fig. 5-4 Flexure structure of UPCU ····· 75
Fig. 5-5 Kinematic model of the UPCU ····· 76
Fig. 5-6 Block diagram of PID controller ····· 80
Fig. 5-7 Block diagram of PID controller in global servo for simulation ·· 80
Fig. 5-8 The structure of UP-2 ····· 82
Fig. 5-9 Schematic diagram of error compensation system ····· 82
Fig. 5-10 The straightness error of X-axis motion ····· 83
Fig. 5-11 The thermal displacement of spindle ····· 83
Fig. 5-12 20nm motion of UPCU (Vibroisolating table) ····· 85
Fig. 5-13 20nm motion of UPCU (3000rpm on spindle) ····· 85
Fig. 5-14 The tracking error of UPCU (3㎛) ····· 87
Fig. 5-15 The tracking error of UPCU (1.5㎛) ····· 88

LIST OF TABLES

Table 3-1 The performance of optical fibre encoder ····· 21

Table 3-2 Air sensor performance ····· 21

Table 3-3 Material sensor performance ····· 21

Table 4-1 Material properties of ultra-precision cutting unit ····· 47

Table 4-2 Boundary conditions of stability depending on hinge type ····· 52

Table 4-3 FEM analysis results depending on the hinge type ····· 52

Table 4-4 Boundary conditions depending on the cutting force ····· 56

Table 4-5 FEM analysis results depending on the cutting force ····· 56

Table 4-6 Boundary conditions on stability depending on the material change ····· 59

Table 4-7 Stress distributions depending on the material change ····· 59

Table 4-8 Boundary conditions on stability depending on the material change ····· 62

Table 4-9 Displacement responses depending on the material change ····· 62

Table 4-10 Displacement data of PZT, FEM and micro-stage ····· 65

Table 5-1 Performance of PZT ····· 77

Table 5-2 Control parameters of PID controller in micro servo for simulation ····· 80

NOMENCLATURES

$\overrightarrow{{}^{F}V_{A}}$: The position vector from the origin of the fitted coordinate to the discretionary position 'A' of the kinematic coordinate

$\overrightarrow{{}^{M}V_{O}}$: The vector of the kinetic coordinate from the origin

$\overrightarrow{{}^{M}V_{A}}$: The vector regarding the kinetic coordinate to the discretionary position 'A'.

$\overrightarrow{{}^{F}V_{R,O}}$: The objective position vector of the fixed focal point on the guide surface of the transfer table

$\overrightarrow{{}^{F}E_{A}}$: The stiffness of X, the surface translating error Y, and the yaw error ϕ_Z regarding the angular error

$\overrightarrow{{}^{F}D_{A}}$: The value of errors from the discretionary point 'A'

${}^{F}_{M}R$: The rotational matrix regarding the fitted coordinate respect to the kinetic coordinate

${}^{M}U_{p}$: The output positional change of the piezoelectric actuator

P_C : The compensated axis position

R_C : The compensated resolution

U_p : The input voltage of the piezoelectric actuator

U_{AMP} : Output of amplifier

W_C : The compensated wavelength of the laser in air

W_V : The vacuum wavelength of the laser

$A(s)$: The matrix of input and output of piezoelectric actuator

B : Matrix of deformation ratio

D : Matrix of material property

E : Young's modulus of elastic material

F : The interpolation factor

H : Current relative air humidity in %RH

P : Current air pressure in Pascal (N/m^2)

R : Radius of hinge

T : Current air temperature in ℃

h : Horizontal length of hinge

t : Thickness of hinge

n : Current refractive index (dimensionless)

ϕ_X : Roll error

ϕ_Y : Pitch error

ϕ_Z : Yaw error

f^e : Applied force vector

k^e : Matrix of element stiffness

y_β : Transfer function of P gain for PID controller

y_γ : Transfer function of I gain for PID controller

y_α : Transfer function of D gain for PID controller

$y(s)$: Output of transfer function

σ : Stress of PZT

$\hat{\sigma}$: Material stress

ν : Poisson's ratio

$\hat{\Psi}$: Displacement of FEM model

ABSTRACT

The Compensation of Environment and Motion Error for nm Grade Accuracy Improvement of Ultra Precision Turning Machine

Kwac Lee-Ku

Adviser : Prof. Kim Jae-Yeol, Ph.D.

Department of Precision Mechanical Engineering,

Graduate School of Chosun University

The ultra-precision products which recently experienced high in demands had included the areas of most updated technologies, such as, the semiconductor, the computer, the aerospace, the media information, the precision machining. For early 21th century, it was expected that the ultra-precision technologies would be distributed more throughout the market and required securing more nation-wise advancements. Furthermore, there seemed to be increasing in demand of the single crystal diamond tool which was capable of the ultra-precision machining for parts requiring a high degree of complicated details which were more than just simple wrapping and policing. Moreover, the highest degree of precision was currently at 50 nm for some precision parts but not in all. The machining system and technology should be at very high performed level in order to accomplish this degree of the ultra-precision. It was known that the products requiring the ultra-precision machining technology were applied only in some advance countries as measuring instrument, satellite observing systems, airplane observing system, and national defense weapon system and other special areas which all included

precision optics.

The technological manipulation of the piezoelectric actuator could compensate for the errors of the machining precision during the process of machining which lead to an elevation and enhancement in overall precisions. This manipulation is a very convenient method to advance the precision for nations without the solid knowledge of the ultra-precision machining technology. Moreover, there is an increasing demand of the highly responsive ultra-precision positioning control technology based on not only the piezo electric actuator for the non-axis symmetrical mirror machining, but also the delicate control of in feed rate application such as the ductile mode machining of the hardened-brittle Materials. Due to the facts mentioned above, the ultra-precision positioning technology manipulated by the piezoelectric actuator was regarded as the basis of this investigation. The main objectives of this thesis were to develop the Ultra-Precision Cutting Unit (UPCU) which enabled the 3-axis control by the manipulation of the piezoelectric actuator and to enhance the precision of the current lathe which is responsible for the ductile mode machining of the hardened-brittle material where the machining is based on the single crystal diamond.

There were 3 divisions of researches conducted to develop the UPCU for precision enhancement of the current lathe and compensation for the environmental errors, the Laser application instrument has been employed to measure the environment error and the operative error. Also, extensive developments in planning, safety analysis and control to complete UPCU application which was capable of collecting the series of errors mentioned earlier and providing real-time corrections, have been carried out.

The first, we are designed to measure and real-time correct any deviations in variety of areas to achieve a compensation system through more effective optical fiber laser encoder than the encoder resolution which was currently used in the existing lathe. The deviations for a real-time correction were composed of followings; the surrounding air temperature, the thermal deviations of the machining materials, the thermal deviations

in spindles, and the overall thermal deviation occurred due to the machine structures.

The second was in the process of developing UPCU, and the main objective was to manufacture the UPCU by applying the real machining condition and confirming the safety level with the FEM analysis.

Finally, we are to develop the UPCU and to improve the machining precision through the ultra-precision positioning and the real-time operative error compensation.

The ultimate goal was to improve the machining precision of the existing lathe through completing the 3 researches tasks mentioned above. The real-time error compensation result of UPCU had displayed approximately 50nm of the tracking error capability.

국 문 초 록

초정밀 가공기의 나노미터급 정밀도 향상을 위한 환경 및 운동오차 보상

곽 이 구 (郭 二 丘)

지도교수 : 김 재 열 (金 在 烈)

조선대학교 대학원 정밀기계공학과

최근 수요가 급증하고 있는 초정밀 제품은 반도체, 컴퓨터, 항공우주, 영상정보, 정밀기계 산업 등 첨단산업 분야에 광범위하게 사용되고 있으며, 21세기 초에는 그 사용분야가 급속히 확대될 것으로 전망되므로 초정밀 가공기술은 국가적으로 시급히 확보해야 할 첨단기술 분야이다. 또한, 요구되는 부품의 정도가 매우 높고 형상이 복잡하여 래핑이나 폴리싱만으로는 가공이 불가능하게 됨에 따라 초정밀 가공기를 사용한 단결정 다이아몬드 공구에 의한 초정밀 가공이 각광을 받고 있다. 또한 각종 정밀부품의 일부 정밀부품에서 요구되는 정밀도는 현재 최고 50 ㎚에 이르고 있다. 이와 같은 가공정밀도를 달성하기 위해서는 매우 높은 가공시스템의 성능과 가공기술이 요구된다. 그리고 초정밀가공기술이 요구되는 제품들은 약 10년전까지만 해도 일부 선진국에서만 정밀광학을 이용한 측정설비, 위성용 관측시스템, 항공기용 관측시스템, 국방관련 무기시스템 등 일부 특정한 분야에만 적용되어 왔다. 이와 같이 정밀 비구면 렌즈가 일부 한정된 분야에만 사용되어 그 수요가 많지 않았고 요구되는 정밀도 또한 크게 높지 않았기 때문에 70

년대까지만 해도 주로 숙련된 작업자의 수작업에 의해 가공되었다. 그러나 최근 들어 전자, 광학분야의 확대발전과 더불어 광학계에 대한 경량화 요구에 따라 비구면 광학계에 대한 수요가 급속히 증가하고 있고, 비구면 렌즈의 정밀도가 사용되는 광파장이 짧아짐에 따라 점차 높아지는 추세에 있어 이들 제품을 양산하기 위한 가공기술의 확보가 시급한 실정이다.

초정밀가공에서 압전엑추에이터의 응용기술의 중요성은 가공정밀도를 가공중에 오차를 보상함으로써 한 차원 높일 수 있어 우리나라와 같이 가공기 자체의 정밀도를 향상시키기 위한 기반기술이 취약한 국가에서는 매우 유용한 기술이다. 또한 압전엑추에이터를 이용한 고응답 초정밀 위치제어 기술은 비회전대칭 형상의 반사경 가공과 미소하게 절입량을 제어하여 가공해야 하는 경취성재료의 연성모드절삭등에 적용이 증대되고 있다.

이와 같이 본 논문에서는 압전엑추에이터를 이용한 초정밀위치결정기술을 기본으로, 이를 응용하여 3축 제어가 가능한 UPCU를 개발하고, 단결정 천연 다이아몬드를 이용한 경취성재료의 연성모드절삭에서 기존의 가공기의 가공정밀도를 한 수준 높이고자 한다.

본 논문에는 기존의 가공기의 가공정밀도를 한 수준 높일 수 있는 UPCU의 개발과 가공정밀도 향상을 위해 아래와 같은 3가지 연구를 진행 하였다.

첫 번째 연구는 기존의 가공기에서 사용된 엔코더의 분해능보다 월등한 광섬유 레이저 엔코더를 사용하여 변위를 측정하며, 공기의 온도, 가공물의 열 변형, 스핀들의 열 변형, 기계구조에 따른 열 변형 등을 실시간 측정 하여 보상할 수 있는 시스템을 구성하는 것이다. 두 번째 연구는 가공기의 스핀들과 그 외 기계 구조 전체에 대해 3차원 레이저 진동 측정을 하거, 진동특성 분석을 통해 기공기의 개선점을 제안한다. 세 번째 연구는 UPCU에 대한 설계단계이며, 가장 적절한 재질과 형상을 갖는 UPCU를 제작 하기위해 실제 가공조건을 적용하여 안전성을 FEM 해석을 통해 검토하는 것이다.

그 결과 실시간 오차보상을 하여 UPCU는 약 30nm의 추종오차 성능을 보여주었다.

I. INTRODUCTION

A. Motivation

As the world has entered to 21st century, the world announced for the knowledge based society which would bring revolutions to the existing industrial society. The world started to turn its focus on areas such as the information technology, the nano-technology, and the biotechnology. The nano-technology is applied in different manners and into different meanings towards variety of areas for example; the science, the industry, and the media. The nano-technology was initially applied to improve the limitations set in the semiconductors of the micro technology but its capability surpassed the initial expectations and applied to industries such as the electronics, the information network, the machining, the chemistry, the biology, and the energy and thus transformed the human life for the better [(1)~(3)].

In order to accomplish the nano-technologies mentioned above, the ultra-precision positioning was selected as the principle method to initiate the machining, the electronics, the optics, the control application, the prototype design, and the manufacturing processes. The ultra-precision positioning established the current physics technologies such as the STM (Scanning Tunneling Microscopy) or AFM (Atomic Force Microscopy) which could conduct the micro measurements and manipulation in the level of the single atom within the micrometer range. However, the current business industry which was deviated by following areas such as the ultra-precision machining, the ultra-precision measurement, the semiconductor wafer, the network devices, and the optical magnetic memory had ensured requirements of the ultra accuracy and the product amplification which required the development of the ultra-precision machining that was composed of a few hundreds long stroke while maintaining the maximum precision level

to nm range[4]~[8].

The ultra-precision products which recently experienced high in demands had included the large areas of most updated technologies, for example, the semiconductor, the computer, the aerospace, the media information, the precision machining. For early 21st century, it was expected that the ultra-precision technologies would be distributed more throughout the market and required securing more nation-wise advancements. Furthermore, there seemed to be increasing in demand of the single crystal diamond tool which was capable of the ultra-precision machining for parts requiring a high degree of complicated details which were more than just simple wrapping and policing. Moreover, the highest degree of precision is currently at 50 nm for some precision parts but not in all. The machining system and technology should be at very high performed level in order to accomplish this degree of the ultra-precision. It was known that the products requiring the ultra-precision machining technology were applied only in some advance countries until 10 year ago as measuring instrument, satellite observing systems, airplane observing system, and national defense weapon system and other special areas which all included precision optics. In 70s, the aspheric lens were required their presence in limited areas, ; thus the products were manufactured individually by experienced engineers. However, there were increasing demands in the aspheric optic technology since there were dynamic developments in the electronics and the optics and increasing preferences in lightweight. There should be the improvement in machining technology since the degree of precision in the aspheric lens increased as the optical wavelength had shortened[9]~[15].

In the case of the ultra-precision machining, the manipulation of the PZT (Piezo electric actuator) was able to compensate for any performance errors while the machining was in the process. This manipulation of PZT elevated the level of precision of the ultra-precision lathe technology domestically. Moreover, there had been increasing demands for ultra-precision positioning technology that were high response with the

PZT basis and there seemed to overgrowing applications of the non-axisymmetrical reflection machining and the ductile mode machining in the microscopic infeed rate with the hardened-brittle materials basis. Furthermore, the PZT application seemed to be used for the extensive manipulation of the vibration assisted machining which were based on the highly precise repetition activity of electrical actuator, where the vibration assisted machining was need to apply the micro pattern machining for the optic parts. The studies conducted in this investigation would promote the low level of machining technology to maximize the effects of the technological developments by investing small amounts thus there would be extensive impacts on the related areas to this technology.

The ultra-precision machining with the PZT upgrade was designed as the most updated machining technology to surpass the limits of the traditional ultra-precision machining technology and to enable the development of the mini sized precision machines with new meaning and the optic parts with all type of complicated formation. The consumers' view about the machine manufactured products would be revolutionized and it was expected that the highly precise products would be well-distributed among the consumers.

The ultra-precision lathe installed with single crystal diamond tool is largely dependent upon the operating activity of the general parts such as the main spindle, the feed mechanism which determine the precision degree of the machining. Therefore, there requires the enhancements in degrees of operating precision and the real-time compensations for any operating errors. Recently, the ultra-precision lathe had undergone enlargement in the diameter of the constructed figures of the possible products, which led to the stroke of each slide to elongate to a few hundreds mm range while maintaining the high precise nm resolution and need of the high precision degree in full stroke range. However, the mass of inertia in transporting range was observed to be too large which might not be able to attain the response speed to accompany any compensation techniques for operating errors. Due to this reason, the degree of precision

in equipment part can not be enhanced and the financial pressure in the lathe development starts to rise. Thus, the certain limitation in degree of precision may apply due to the presence of a few m intensity of axial motion errors in spindles, motion errors in transferring, and the variation occurring in the constructed figures.

In order to overcome these problems, there are ongoing researches on the ultra-precision cutting unit which was finely activated with mini-sized cutting tool and tool holder supported from the precisely and accurately measured spindle and degree of precision using PZT.

B. Objective and outline of this research

The technological manipulation of the PZT could compensate for the errors of the machining precision during the process of machining which lead to an elevation and enhancement in overall precisions. This manipulation is a very convenient method to advance the precision for country without the solid knowledge of the ultra-precision machining technology. Moreover, there is an increasing demand of the highly responsive ultra-precision positioning control technology based on the PZT for the non-axis symmetrical mirror machining as well as the delicate control of in feed rate application such as the ductile mode machining of the hardened-brittle materials. Due to the facts mentioned above, the ultra-precision positioning technology being manipulated by the PZT was regarded as the basis of this investigation. The main objectives of this investigation were to develop the UPCU (Ultra-Precision Cutting Unit) which enabled the 3-axis control by the manipulation of the PZT and to enhance the precision of the current lathe which was responsible for the ductile mode machining of the hardened-brittle material where the machining was based on the single crystal diamond. There were 3 divisions of researches conducted to develop the UPCU for precision enhancement of the current lathe and compensation for the environmental errors as shown below.

(1) The real-time feedback and the environment compensation of the optical fibre laser encoder
(2) The UPCU safety verification through the FEM analysis
(3) The overall machining precision enhancement through real-time compensation of the motion error by the UPCU application

In this research, there was the laser application instrument in order to measure had measured the environment error and the operative error and there were extensive developments in planning, safety analysis and control to complete UPCU application which was capable of collecting the series of errors mentioned earlier and providing real-time corrections.

The first research was designed to measure and real-time correct any deviations in variety of areas to achieve a compensation system through more effective optical fibre laser encoder than the encoder resolution which was currently used in the existing lathe. The deviations for a real-time correction were composed of followings; the surrounding air temperature, the thermal deviations of the machining materials, the thermal deviations in spindles, and the overall thermal deviation occurred due to the machine structures.

The second research was in the process of developing UPCU, and the main objective was to manufacture the UPCU by applying the real machining condition and confirming the safety level with the FEM analysis.

The third research was to develop the UPCU and to improve the machining precision through the ultra-precision positioning and the real-time operative error compensation.

The ultimate goal was to improve the machining precision of the existing lathe through completing the 3 research tasks mentioned above.

II. LITERATURE SURVEY

A. Review of related researches

There are ongoing researches on developing milli structures or the micro machine among the advanced countries, and the development of micro machining technology is one of the most important leading areas which exceptionally perceives as the intensive component. The currently applied micro machining technology could be differentiated to the semiconductor manufacturing technology such as the lithography and etching and the general machining technology such as cutting, grinding, and the electro-spark machining. The former could be restricted by the thickness in material or its quality. The other might have the relatively adequate manufacturing range in areas of cutting and electro-spark machining but experience difficulty in achieving excellent quality of the machined surface. Thus, the machining with higher cutting technology which is excellent in productivity as well as the modifiability would be sufficient in some cases. This might be suitable to achieve machined surface that is high quality by applying the ultra-precision machining technology, however there are not sufficient amount of examples in micro parts being developed by the lathe. Therefore, there are ongoing researches on milling procedures using the single crystal diamond tool to produce the ultra-precision micro parts based on the 3-dimensional formation[(16)~(19)].

The ultra-precision machining technology is mainly composed of the micro drilling technology being 0.1 mm or less, the micro end milling technology, and the single diamond bite and the serve micron unit based ultra-precision mirror surface machining. These technologies were upgraded to the ultra micro and precise machining technology by the applications of the micro drill of several tens microns, the 0.2mm diameter level of the end milling and the diamond tool in several tens of nanometer order manufactured

for the micro machining purpose.

Moreover, the recent issues of applying the ultra-precision high speed machining technology and the environment friendly machining technology had largely affected the theme of development and directions of ultra-precision machining technology[20]~[23].

There had been extensive technical developments towards the fundamentals of the machining technology such as machining status and its formation even with the rapid changes in technological environment. Most noticeably, there seemed to be huge changes occurring in the ultra-precision parts which were directly applicable as practical usages.

Examples of typical practical applications are the ultra-precision high performance optic products such as the aspheric surfaces, the non-axisymmetrical aspheric mirrors, the micro lens, and the diffraction gratings. Second examples include developments of the ultra-precision micro machining technology of typical micro parts to meet the needs of the ultra micro part formations such as the milling machine and the micro machine. Among these recent applications, there are extensive developments and researches to enhance the MEMS technology which has heavy emphasis on the energy production, the electrics, or the chemical production or the semiconductor technology where there was the nm level of high precision required as well as the machining techniques[24]~[25].

The limitation of the surface roughness was in the range of 0.005~0.01㎛ to quantitatively describe the changes occurring periodically. However, the form accuracy which described for the degree of precision could be perceived one level elevated range of 0.05~0.1㎛[26]~[30].

Additionally, the enhancement of one precision level usually takes about 25~30 years, so it was expected that the degree of machining would develop up to the detail grating gap, ; thus from upcoming years posterior to 2000, there should be neo-technology development for ultra-precision machining down to the level of atomic arrangement.

B. Domestic research trends

KIMM (Korea Institute Machinery & Materials) is able to authorize and evaluate the technologies in developing 50~100㎛ of micro drills. It enables perforating the old equipments with the machining systems substituted with the staffing monitor. Also, KIMM had developed the ultra-precision mirror surface machining through the ultra-precision machining procedures and conducted related researches of the typical ingredients and material formation in the ultra-precision machining procedures. Moreover, KIMM is in the procedure of accomplishing the milli-structure or the part of micro machine through the ultra-precision machining(81).

The FTS for ultra-precision machining which developed from the institute for advanced engineering had improved to 5~10 times the degree in precision machining of the ultra-precision lathe with 0.7㎛ p-v of the form accuracy as well as 10nm p-v of the surface roughness. DaeWoo Machinery is expected to pronounce the introduction of the intranationally highest quality model of the ultra-precision lathe which was installed with the large aspheric mirror performing at 0.7㎛ p-v and 40nm p-v for the form accuracy and the surface roughness, respectively(82).

Samsung electronics has manufactured variety of the ultra-precision optic parts which were empowered by the highest intranational ultra-precision mirror surface machining. Recently, Samsung electronic had a huge success in developing the authorized procedure for the productions of F-0 Lens that was composed of the curved surface-like aspheric surface for the laser printers.

The ultra-precision mirror surface machining was installed to Korea Basic Science Institute (KBSI) in 1998 and there are ongoing developments in typical ultra-precision parts and metallic moulds machining technology (83).

However, these intranational developments were mostly dependent upon the foreign

equipments and technologies, ; thus they are still at the level of not being able to establish the micro machining technologies to be pronounced as the unique. Therefore, there should be more efforts in enhancing the ultra-precision concept of the micro machining technology to develop specific parts for the micro machines to dominate in 21th century.

C. International research trends

Japan provides the most updated micro machining technology internationally. Japanese IMSE (Institute of Mechanical Systems Engineering) had researched to accomplish the micro factory where the smallest micro lathe in the world was created. The micro lathe was weighed 100g in 32×25×30.5mm of the physical dimension and its manufacturing procedures were focused highly on the XY driving unit based the laminated PZT and the main spindle device incorporated within the micro motor. The main spindle device had 1.5W of the driving capacity with 1/50 of the regular lathe size, 1/10,000 of the weight, and 1/1,000 of the required energy. This lathe had its performance comparable to other lathe as the performance evaluation had displayed that, the bass bong with 2 mm diameter was undergone the cutting machining procedure and its corresponding product was observed with 1.5㎛ (Rmax) of machining roughness and 2.5 ㎛ for the roundness. It was also detail enough to handle up to 60 ㎛ of the most minimum sized workpiece and capable of handling materials such as the aster resin bong [33)~(34)].

Generally, the micro machining was limited to the lithography machining of the brittle material such as Silicon Oxide, ; however, the current production lines required the introduction of the metal materials to the micro machining and the micro mechanism.

As the information devices and the technology of the relative areas had advanced dramatically, the corresponding components or devices become more precise and mini, ; thus Tokyo University supported ongoing researches in micro mechanism machining, developing and manipulating. The micro lathe installed with the hyper-speed spindle that had 100,000rpm as its maximum speed was newly designed and undergone developing the experimental procedures with 10㎛ diameter size of micro structure. Moreover, in order to enable machining of 3-dimensional formed micro construction figures, the micro machining machine was newly developed with the ultrasonic motor to observe the

vacuum chamber of the SEM without any negative interference. Furthermore, there are ongoing researches to develop a specialized model of SEM to observe the 3-dimensional figures.

A 200㎛ diameter ranged micro drill was commercially developed by the Hitachi company. The Saico company had manufactured an 80㎛ diameter ranged micro drill for the machining of the ultra mini motion in time watches.

There had been co-developments of the sharp tip for FIM (Field Ion Microscopy) purpose to achieve the micro lathe with 5㎛ radius between Japanese Nagoya national industrial research institute and Colorado University of USA. Aside from this, there are ongoing researches concerning of the mechanical micro machining through precision, the diamond lather tuning, and the micro precision of the general machining technology. More importantly, there seem to be extensive developments of the micro metal formation based on the 3-dimensional structure.

Japanese FANUC company had developed the ultra-precision micro machine called "ROBOnano Ui", which could proceed complex machining up to 3-dimensional formation machining in lather turning. This machine enables mechanical lithography of the diffraction gratings of the free curve surface formation and machining of the metallic structure for aspheric lens. As a unique characteristic of this machine, there is the constant air pressure based Non-fiction servo system which was composed of a 200mm of feeding distance and a 1nm of resolution and 2㎛ error range of the feeding motor track.

In the case of the United States, the development of the micro machining technology mostly focused on the beam machining and the tradition machining. Thus, there are not rapid developments in areas of the micro mechanical machining. Followings are the typical researches related to this area[(40)(43)].

There are ongoing researches for the accurate diagnosis on electric discharge status and the electrode feeding control in Pur due American University. Rochester University and

Moore Tool company had co-developed the joint applications of the cutting and the ultra-precision machining called "Nanotech150AG", which required for every 10mm diameter range of the aspheric surface micro lens, 1nm of the roundness, 1-2nm range of the defect class in the machining surface. Moreover, the Nation Jet company was successful in developing micro drilling machines and drills to conduct 2.5㎛ of precise machining on 25㎛ of a hole.

Ever since the introduction of the single diamond tool by Union Carbide in 1966, the competitions in developing the ultra-precision lathe technology among research facilities such as LLL, CUPE and commercial companies such as Moore, Pneumo Precision, and Philips had more emphasis in the areas of the semiconductors, electronics, and the optical industry.

The Pneumo company, since the late 1970s, the specialized manufacturer of the ultra-precision lathe had developed following commercial products; the MSG-325 which was the 2 step control CNC lathe featuring 300mm limit aspheric surface, the MGS-500 which was the polygon mirror lathe, the MGS-700 featuring the 14" limit face lathe for the magnetic disc machining purpose. In year 1988, the aspheric surface lathe, ASG-2500 which was the ultra-precision lathe installed with the cutting function was introduced and dominated the world marketing of the ultra-precision. Recently, the newly designed NANOFORM 600 was proposed targeting 1990s marketing. The detail specifications of NANOFORM 600 were listed as following; the granite materials for the bed, the principal axis installed with the aerostatic gas bearing, the guide surface featured with 0.25㎛/300mm as the positioning determinant using the hydrostatic method, the resolution with 1.25nm performance rate, and the maximum workpiece input value of 600x300mm. The NANOFORM 600 had test results of the aspheric surface machining for the 75mm of OFHC metalloid was within the 0.1㎛ formation range and the 0.01nm Rmax as the maximum surface roughness.

CUPE had proposed the ultra-precision lathe to manufacture the aspheric mirror

(1400mm as the maximum longitude, 600mm as the maximum length) for completing the macro-sized X-lined astronomical telescope. This lathe had a contract with British Science and Engineering Research Council to manufacture the inside rotational parabolic wall and the out side rotational hyperbolic surfaces which would act as utility in the X lined telescope. The product specifications were proposed as following; the artificial granite was applied for the bed ingredient, 0.5 arcsec/1100mm motive range to X direction, 0.1㎛ of rotating degree of the rotary table utilizing the gas bearing, and 876N/㎛ of the radial directed forces. The result of 300mm length application to manufacture conical shaped part was 0.2㎛ of the Straightness and 0.4㎛ of the roundness for applying 300mm length.

The Union of European Countries is currently developing the micro system related technologies to become financially stable enough to compete against the States and East Asia Countries. The developments new line of products through constructing mini-sized for the parts and the equipments was legitimate since such production would induce the energy savings and prohibit mass production of industrial wastes for advanced European countries who were the pioneers of creating Earth friendly environment[(40)(43)].

The KUGLER company of Germany, the Micro Tuning M/C (Model Type: D75/150) was developed and distributed. The air baring was selected and enabled machining of objects such as the plane surface, the spherical surface, the conical shape and the aspheric formation. It also allowed supplementing the C shaft (Air Baring selected) for the rotary table. The machining was completed with 150mm of the motive distance for X shaft which enabled constructing 50mm of diameter of the workpiece as well as 5nm(Ra) level of roughness on the machining surface. As general examples, the machining of the contact lens, and the micro emission metalloid for cosmetics had become possible.

The Fraunhofer research firm in Germany had manufactured the structural parts for micro components through applying the micro cutting and milling machining and the

micro shaft by machining with the ultra micro lathe. There were overall adequate qualities for the developed product featuring 50㎛ for larger diameter, and 8㎛ for smaller with approximately 10nm (Ra) of the surface roughness as shown in the picture.

The DATRON Electronics in Germany had developed 3 shafts CNC micro machining center of maximum 70,000rpm of spindle rotation speed in order to establish the ultra-precision high quality machining.

The ISR research firm of Swiss had developed the micro stick & slip actuator which was applicable in the complex mini structures and it is in the study process of extensive enhancement.

In Summary, the developments of the milli structure or the micro structure had become major components of technology among the advanced nations. The current level of the ultra-precision machining technology in the nation is not comparable to the technologies of the foreign advanced countries. The intranational research firms such as KIMM, Samsung Electronics, or KBSI are currently developing all types of the ultra-precision parts and the metallic machining technologies but they are heavily dependent upon the foreign equipments and basic technologies. Japan had induced the most efficient research developments in the micro machining technologies. The Rank Pneumo Precision co. or CUPE had also developed the ultra-precision lathe and European countries are currently developing to attain more efficient micro systems to strengthen their future technological competition.

The development in parts for micro machine governed by the micro machining technology in 21th century in the nation must be extensively engaged with more efforts in order to compensate for the current weak status of the micro machining technologies.

III. THE ENVIRONMENTAL COMPENSATION OF THE OPTIC FIBRE LASER ENCODER

A. Principles of operation of the optical fibre laser encoder

The He-Ne laser was selected as the main laser for the fibre optic laser encoder unit. A laser beam was achieved as a form of gas in a vessel when the high electric pressure connected the negative polarity and the positive polarity as shown in Fig. 3-1. The laser beam was amplified when it resonated between the gap of two mirrors, and only the small amount of the laser light was output through bipolar mirror. The output light represented the laser beam[42].

The laser beam consisted of two modes (Red and Blue), these modes were composed of relatively similar frequency except in the case of polarizations as shown in Fig. 3-2. The two modes could measure the intensity, and the balance was established through modifying the length of the laser vessel along with the heat as shown in Fig. 3-3. The intensities of the two modes are measured, and balanced by controlling laser tube length with a heater. So it is important to keeps the laser frequency less than 0.05ppm.

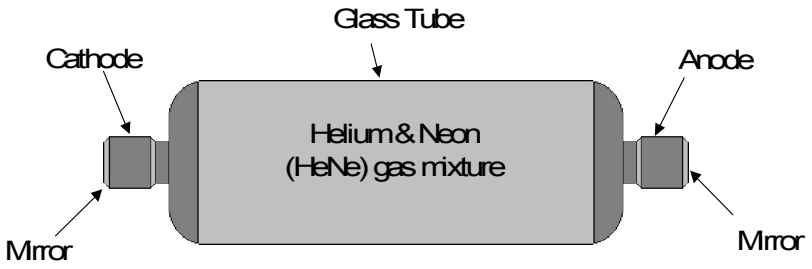

Fig. 3-1 Helium neon laser tube of laser encoder

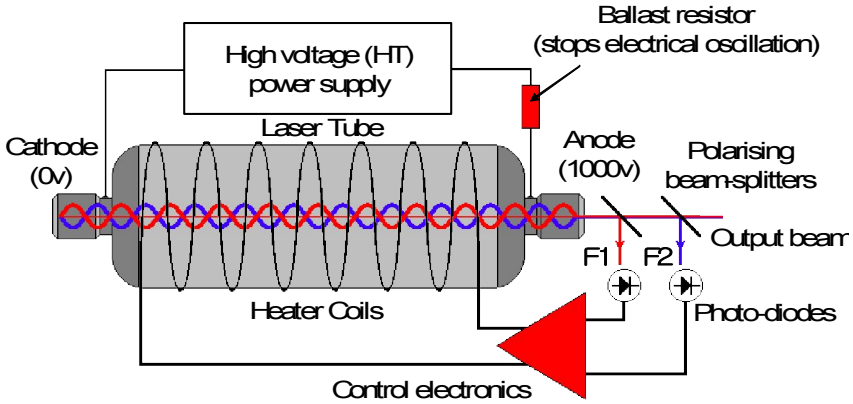

Fig. 3-2 Laser tube operation of laser encoder

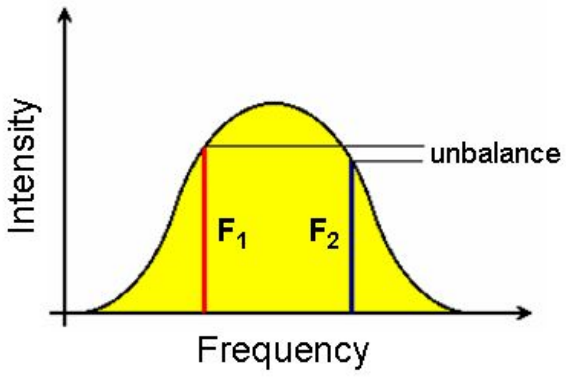

Fig. 3-3 Laser stabilisation and gain curve

The output laser beam is split by a polarising beam-splitter into the two modes (shown in red & blue) as shown in Fig. 3-4. Each beam is then focused with a lens into the core of a single mode polarisation preserving optical fibre. In this case, these two modes were measured through the minimum power supply and avoiding the waste-like maximum power supply.

Moreover, there were 2 different types of optical fibres made; the central part of lens with the high reflex index and the lens coated with the low reflex index. The total reflection governed and maintained the light movement in the inner center of the barrel. The laser beam was emitted from the one end of the optical fibre. The inner lens of the barrel controlled the focus, in order to output 3 mm diameter of the beam.

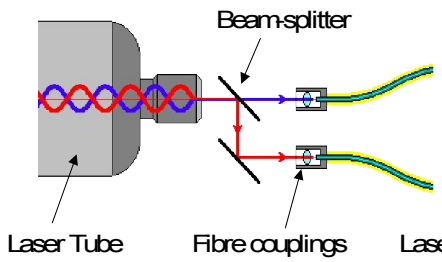

(a) Split by a polarising beam-splitter

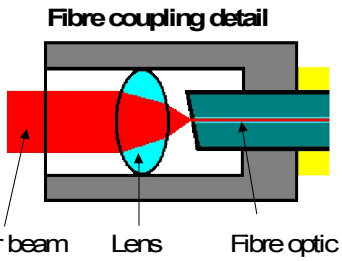

(b) focussing of a lens into the core of a single mode

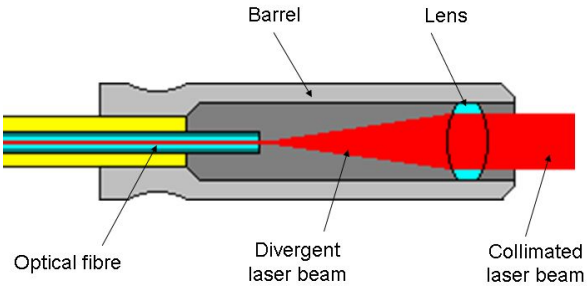

(c) Collimated by a lens inside the barrel to form the 3mm diameter output beam

Fig. 3-4 Fibre optic coupling delivery of laser encoder

Optical fibre is made from two types of glass. A high refractive index glass core is surrounded by a lower refractive index glass cladding. Light traveling inside the core is kept inside by total internal reflection, and cannot escape. As Shown in Fig. 3-5, single mode fibre preserves the coherence of the light. Coherent laser light is required by the interferometer.

Both modes are used to avoid wasting optical power, this maximises the beam power for measurement.

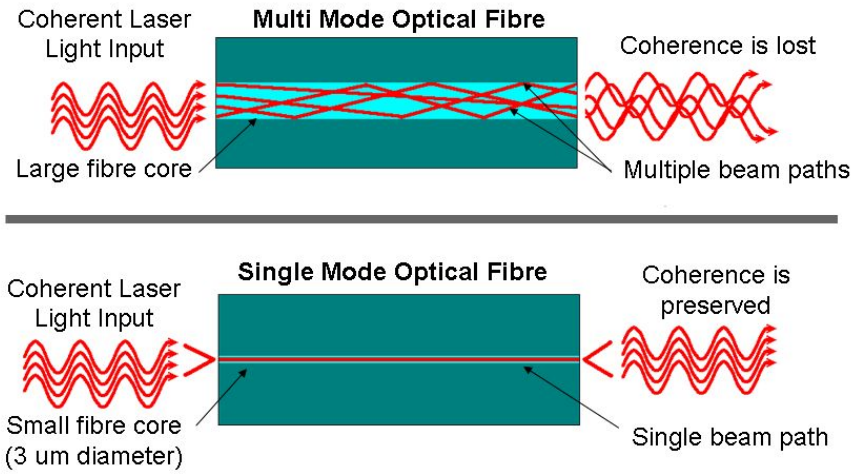

Fig. 3-5 Basic principles of optical fibre beam delivery

The michelson interferometer was known as the generally used laser interferometer and it was not suitable for the machining system due to its complex arrangement. This research had used the laser detector displayed in Fig. 3-6 which was the minimized version as of the optical system as shown in Fig. 3-7.

After passed the shutter, the laser beams are split by the beam-splitter into the reference and measurement arms. The beams are reflected by the plan mirrors and recombined at the beam-splitter where they interfere. Multiple photo-sensors

detect the interference and generate 0º, 90º, 180º and 270º electrical phase signals.

Table 3-1 ~ 3-3 displayed the performance of optical fibre encoder, air temperature sensor and material temperature sensor.

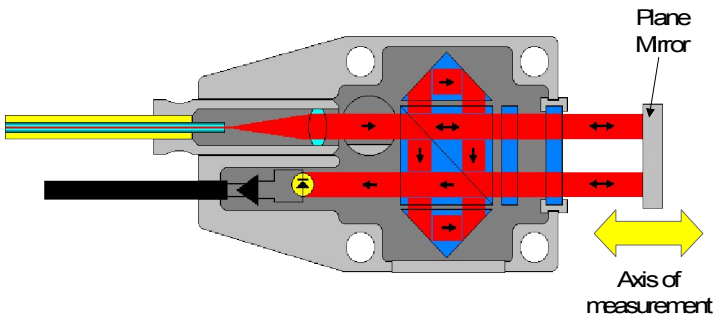

Fig. 3-6 Miniaturized homodyne(single frequency) interferometer

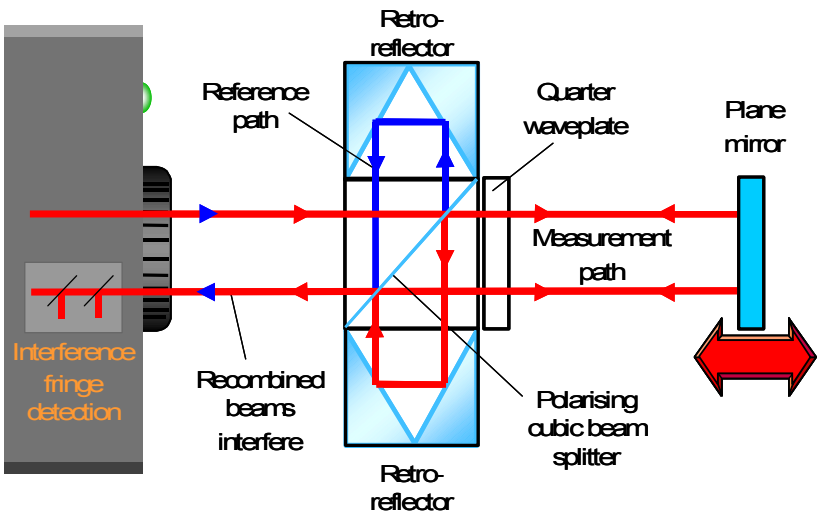

Fig. 3-7 Homodyne(single frequency) interferometer

Table 3-1 The performance of optical fibre encoder

Input resolutions	10 nm to 5㎛ (digital input)
Output resolutions	Digital 10 nm to 5㎛ Analogue 20, 40 and 100㎛
Accuracy	±1 ppm (Refractive index compensation only) ±2 ppm (With 10ppm/deg C material compensation)
Maximum velocity	5m/s Resolutions >400nm, 0.2m/s at 10nm resolution
Compensation update rate	100 ㎛
Delay through compensator	<2μs (digital input - digital output)
Output update rate (digital)(Selectable)	20 MHz (50ns)(minimum edge-edge separation) 10 MHz (100ns), 5 MHz (200ns), 2.5 MHz (400ns)
Output update rate (analogue)	10 MHz (100ns)
Input bandwidth (Selectable)	20 / 10 / 5 / 2.5 MHz

Table 3-2 Air sensor performance

Accuracy	± 0.2°C (Within 13 months of calibration)
Measurement range	0°C - 50°C
Resolution	1/128°C
Update rate	1 Hz
Voltage Range	4.5 to 5.5 Volts
Current	20mA (max)

Table 3-3 Material sensor performance

Accuracy	± 0.1°C (Within 13 months of calibration)
Measurement range	0°C - 50°C
Resolution	1/128°C
Update rate	1 Hz
Voltage Range	4.5 to 5.5 Volts
Current	20mA (max)

B. The system structure

In order to retrieve a correct displacement information, the fibre optic laser encoder system and the environmental compensation unit was capable of compensating for the air reflective index and the temperature.

The fibre optic laser encoder system was designed such a way which enabled measurement for the displacement of the high precision and the positional control. The main components were the fibre optic laser encoder unit and the fibre optic laser detector head as shown in Figs. 3-8 and 3-9. Inside of the laser encoder unit, there was a pair of the flexible fibre optics transferring the laser light into the detector head. Then the fibre optic laser detector head returned the laser light being reflected on the plane mirror back to the encoder unit and induce the feedback signal which was needed for the positional control.

The external formation of the fibre optic laser encoder unit had to maintain absolute stability on the vertical, the horizontal, or every direction surfaces it was installed. The installed surface should not have more than 0.5mm of the degree of even as an acceptable error. The fibre optic laser encoder unit had internal composites of the laser source (He-Ne) and the electric circuit capable of the 2-axial displacement.

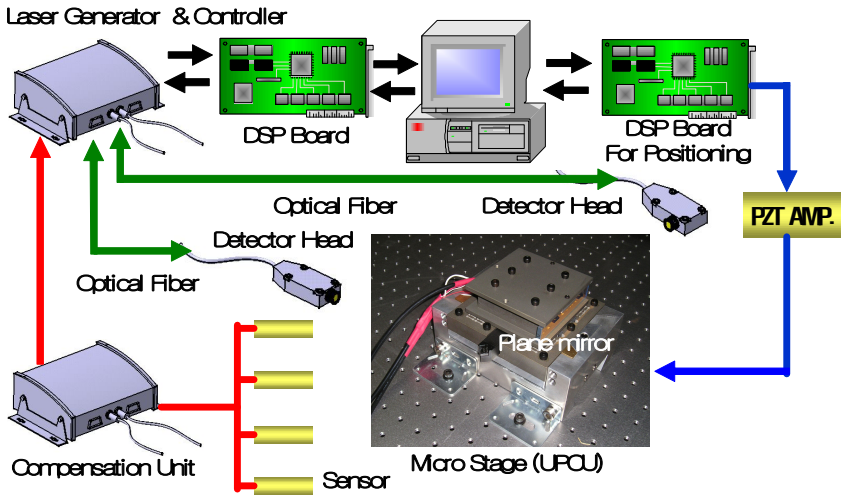

Fig. 3-8 Laser feedback of optic fibre and components of environment compensation system

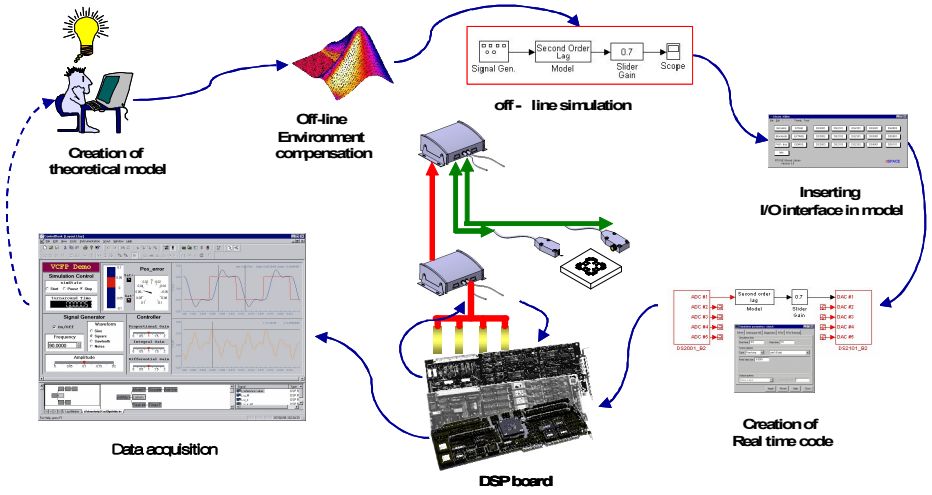

Fig. 3-9 The data acquisition programing of laser optic fibre encoder

C. The environmental compensation of the optic fibre laser encoder

The measuring environment would largely affect the measuring results. The measuring environment mainly consisted of the vibration and the air drift, and the temperature. In order to evaluate the environmental effect, the deviation of the light interference signal was coincided with the temperature change while the optical system was maintained stay put and the vibration and the air drift were in the shielded condition. Fig. 3-10 demonstrated the measuring environment for the unaffected measuring environment as the above. However, the industrial environment was unable to measure up to the same condition as shown in Fig. 3-10. Therefore, the vibration, the air drift, and the temperature change should be experimented and simulated respect to the compensation followed by applying the suitable compensation in respect to the measuring of the measuring environment.

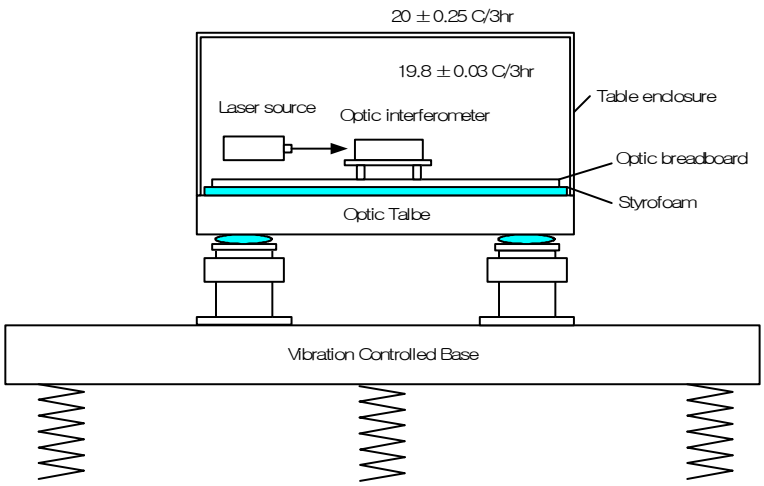

Fig. 3-10 The environmental for interferometry

This investigation had compensated the air reflective index at the real-time by measuring the air pressure and the temperature when the laser beam had passed though the air and applying the environment compensation unit which could compensate for the thermal expansion of the material and the device structure. The environmental unit was designed to output the digital signal and analog signals of various resolutions by receiving input of the differentiated digital quadrature signal of RS422 format on the basis of the high performance DSP technology. In this investigation, the digital signal was selected. Fig. 3-11 shows the functional block line mapping of the environmental compensation unit.

The wavelength of laser varies very slightly depending on the refractive index of the air it travels through. The refractive index of the air depends primarily on it's temperature, pressure and humidity. Any of the following changes in the air will increase the laser wavelength by 0.25ppm (part per million).

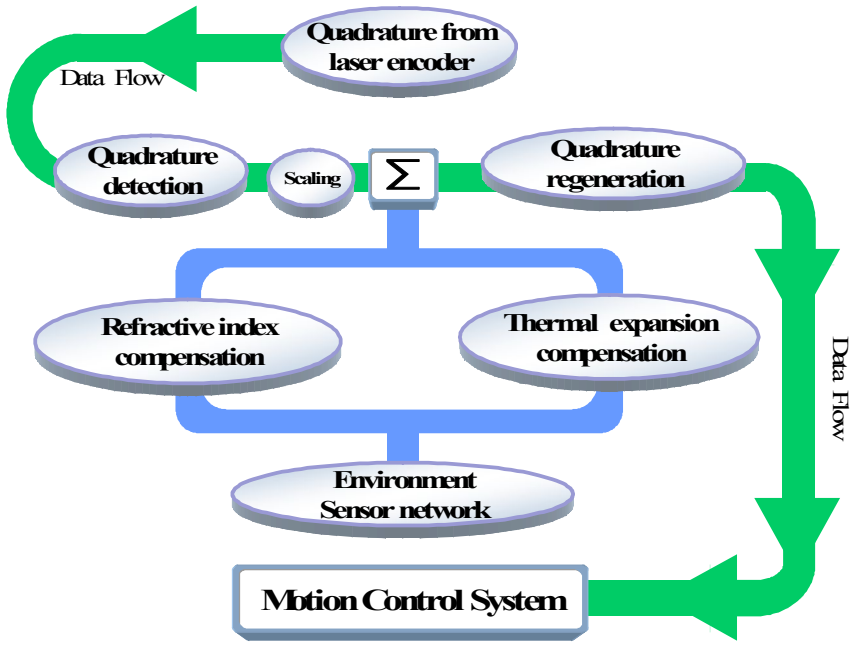

Fig. 3-11 The internal block diagram of environmental compensation unit

~ 0.26 ºC increase in air temperature (= +0.96ppm/ºC)*

~ 0.93 millibar decrease in air pressure (= -0.27ppm/millibar)*

~ 29% increase in %RH (= +0.0085ppm/%RH)*

* : These sensitivities are based on changes from a nominal atmospheric environment of 20ºC, 1013.25millibars and 50% RH

Although the effect on the laser wavelength is small, if high accuracies are required, then air refraction compensation should be performed on the laser position feedback.

The Laser Encoder is supplied with wavelength values which are correct in air at a pressure of 1,013.25millibars, temperature 20ºC and humidity of 50% RH. Changes in the weather will alter atmospheric pressure over a range of ~100 millibars. These will alter the laser wavelength by up to ~25 ppm from the supplied value. Air pressure falls with increasing altitude. This will increase the laser wavelength by ~0.030ppm/metre of altitude above sea level. (This error is easily eliminated by using a an altitude corrected wavelength). Air temperature and humidity can be controlled. The remaining error can be calculated from the sensitivities given on the previous slide. Note that the laser wavelength is more sensitive to humidity at higher temperatures.

The air reflective index, n was determined by the Edlen's equation (3-1) through following data; the pressure (P, Pa), the temperature (T, ºC), the relative moisture (H, %)[42].

$$n = 1 + \frac{7.86 \times 10^{-7} \times P}{(273 + T)} - 1.5 \times 10^{-11} \times H \times (T^2 + 160) \qquad (3\text{-}1)$$

The compensation of the air reflective index would be relative to the air temperature and the data received from the pressure sensor. For the systems with this compensation absence would bring 1 ppm of error in measuring the environmental change.

$$\text{1ppm for every} \quad \begin{cases} 1℃\,(\approx 1.8°\mathrm{F}) & Change\ in\ Air\ Temperature \\ 3.3mb(\approx 0.1\ \ in/Hg) & Change\ in\ Air\ Pressure \\ 30\,\%RH & Change\ in\ Relative\ Humidity \end{cases}$$

The air temperature sensor had monitored the temperature from the transferring route of the measuring beam, and it deduced the internal temperature change of the machine limit. The moisture could be relatively estimated infinitely and the fixed value could be set up discretionarily. After multiple applications of the Edlen's equation (3-1), the air reflective index could be compensated based on these data retrieved from the sensors.

The compensation of the thermal expression of the material would be applied based the information obtained from the temperature sensor but varied depending on the material quality. In other words, the thermal coefficient of the specific materials would be applied for the compensation along with the temperature change occurred from the axial position of origin temperature 20ºC (68°F). The thermal expansion played vital role in the positional error. The standard position should be cautiously selected by considering the material being expanded.

The compensated wavelength of the laser in air W_C (in nm), is then calculated from the air refractive index n and the vacuum wavelength of the laser W_V (in nm), as follows;

$$W_C = \frac{W_V}{n} \tag{3-2}$$

The compensated resolution R_C (in nm) of the laser encoder is then calculated by dividing by the interpolation factor F, which is normally 1, 2, 4, 8,16, 32 or 64 (depending on the amount of interpolation in use).

$$R_C = \frac{W_C}{F} \tag{3-3}$$

If the axis home position is where the optics are close together, then the compensated axis position P_C (in mm), is given by multiplying the encoder pulse count C by R_C.

$$P_C = C \times R_C \times 10^{-6} \tag{3-4}$$

D. The experiment for the environment error compensation

This experimentation confirms the validity of environmental error compensation through measuring the frequency and zero point of laser encoder in accordance with environment conditions.

It is thought that the error factors with environment conditions are thermal expansion of UPCU macro stage to the temperature variation, thermal deformation, air reflective index, temperature, and humidity of spindle and environment error of laser. The thermal deformation of spindle is compensated through real-time measurement inputting signal to UPCU. To reduce the environmental error of laser encoder with air index of refraction, temperature, humidity, a compensating algorithm was built up and displacement error was compensated to the UPCU. Four-type experimentations for environmental error compensation were conducted with insuring the stable zero point of laser encoder and stable frequency of laser as follows.

In the first test, the laser encoder was setup without considering environmental error compensation and the zero point was measured without displacement and constant temperature as shown in Fig. 3-12. In the second test, the encoder was compensated by environmental error without displacement and the zero point was measured under constant temperature. In the third test, the encoder was setup without environmental error compensation and the zero point was measured under no displacement as shown in Fig. 3-12. In the fourth test, the encoder was compensated by environment error and the zero point was measured without displacement.

The first test shows 0~23nm/℃ of error and the second test shows 0~4nm/℃ of error as shown in Fig. 3-13. The third test shows ±15.5ppb(Peak to Peak) of frequency response and the fourth test shows ±1.1ppb of frequency response as shown on Fig. 3-14.

As obtained above, ultra-precision machining with nm order could not be applied at 23 nm/℃ of zero point displacement variation due to no environmental error compensation ; thus it is thought that machining accuracy can not be applicable due to above displacement discrepancy.

Also, the environmental error compensation could be considered a factor, which can be considered to estimate reliability of position information on the side of frequency response; therefore, it was confirmed that the level of reliability of laser frequency was lower without considering environmental error compensation.

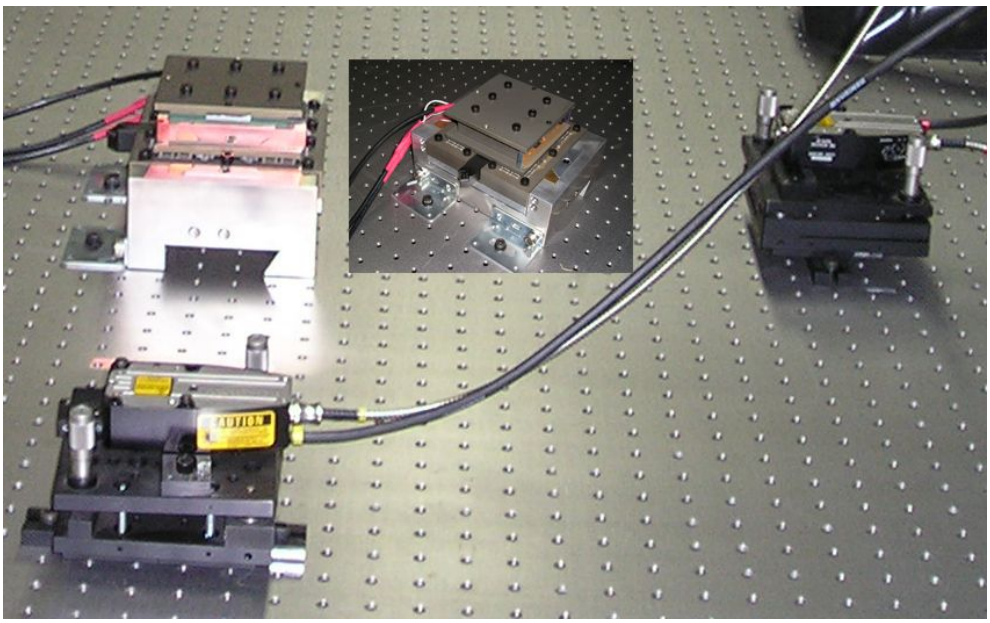

Fig. 3-12 A setting of laser encoder system

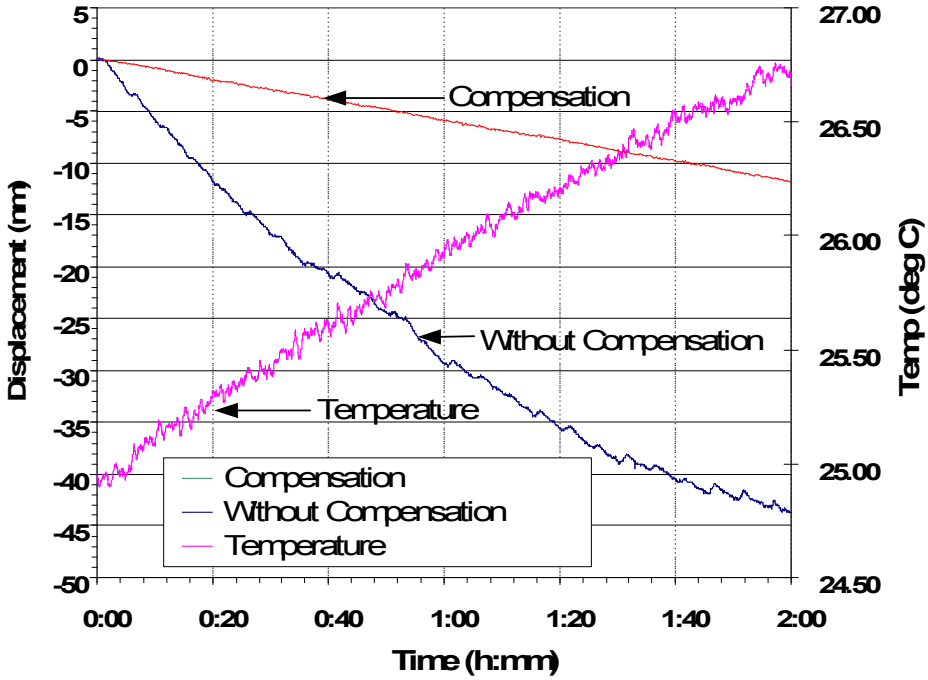

Fig. 3-13 Zero point drift and temperature over time

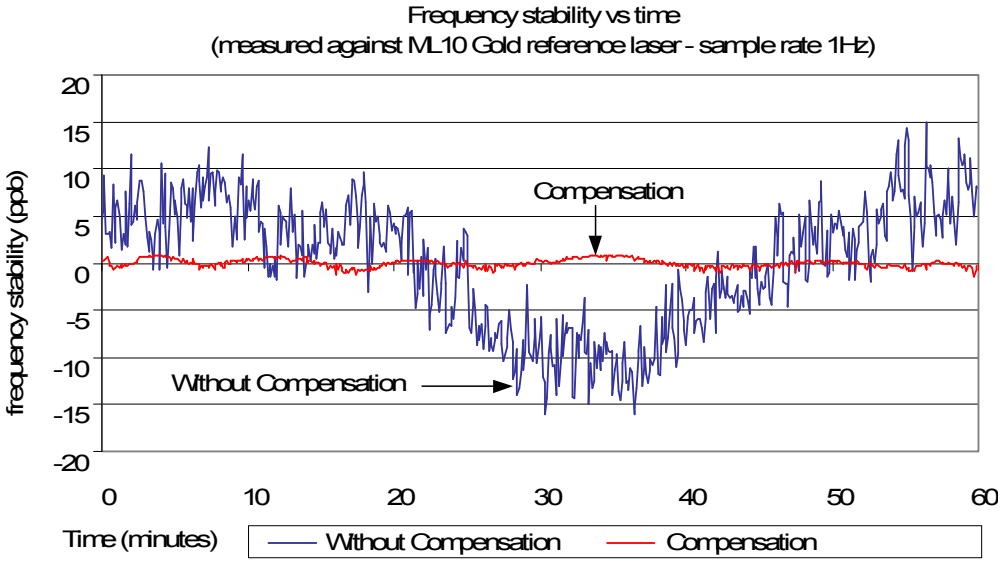

Fig. 3-14 Frequency stability comparison

E. Summary

This chapter focuses on the influence to the position information of the system under temperature variation and without/with considering environmental error compensation and stability of frequency in the laser encoder. The result obtained are as follows ;

1. In the case of no displacement without considering environment error compensation, it is found that the zero-point value is 0~23nm/℃ of error in temperature variation.
2. In the case of no displacement compensated by environmental error, it is found that the zero point value is 0~4nm/℃ of error in temperature variation.
3. The amplitude value is ±15.5ppb (Peak to Peak) of frequency response under no displacement not compensated by environmental error and room temperature.
4. The amplitude value is ±1.1ppb of frequency response under no displacement compensated by environmental error and room temperature.

IV. THE STABILITY ANALYSIS OF UPCU USING A FEM

A. Finite element formulation of 3-dimensional model

The 3-dimensional finite element analysis was conducted to observe the safety level and the deviation characteristics of the elasticity hinge in the micro stage. The material property was analyzed in terms of the degree of elasticity. Plus, the force attributed from the piezoelectric element was loaded by driving the contact of linings. The finite element equation considering these issues was displayed as followings[44)~45)].

1. Displacement function

Fig. 4-1 illustrates a tetrahedral element I. j, m p space defined the x, y and z coordinates. the state of displacement of a point is defined by three displacement components, u, v, and w, in directions of the three coordinates x, y, and z. thus equation (4-1).

$$u = \begin{Bmatrix} u \\ v \\ w \end{Bmatrix} \tag{4-1}$$

Just as in a plane triangle where a linear variation of a quantity was defined by its three nodal values, here a linear variation will be defined by the four nodal values.

$$u = \alpha_1 + \alpha_2 x + \alpha_3 y + \alpha_4 z \tag{4-2}$$

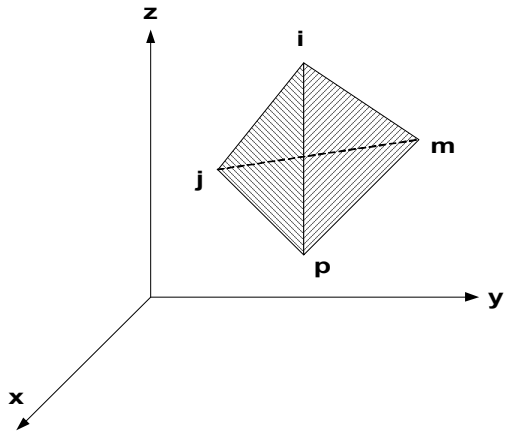

Fig. 4-1 A tetrahedral volume

Equating the values of displacement at the nodes we have four equations of the type from equation(4-3) form with α_1 to α_4 can evaluated.

$$\begin{cases} u_i = \alpha_1 + \alpha_2 x_i + \alpha_3 y_i + \alpha_4 z_i \\ u_j = \alpha_1 + \alpha_2 x_j + \alpha_3 y_j + \alpha_4 z_j \\ u_m = \alpha_1 + \alpha_2 x_m + \alpha_3 y_m + \alpha_4 z_m \\ u_p = \alpha_1 + \alpha_2 x_p + \alpha_3 y_p + \alpha_4 z_p \end{cases} \tag{4-3}$$

$$\begin{aligned} u = \frac{1}{6V}[&(a_i + b_i x + c_i y + d_i z)u_i + (a_j + b_j x + c_j y + d_j z)u_j \\ &+ (a_m + b_m x + c_m y + d_m z)u_m + (a_p + b_p x + c_p y + d_p z)u_p] \end{aligned} \tag{4-4}$$

$$6V = \det \begin{vmatrix} 1 & x_i & y_i & z_i \\ 1 & x_j & y_j & z_j \\ 1 & x_m & y_m & z_m \\ 1 & x_p & y_p & z_p \end{vmatrix} \tag{4-5}$$

In which, incidentally, the value V represent the volume of the tetrahedron. By expanding the other relevant determinants into their cofactors we have equation (4-6) with the other constants define by cycle interchange of the subscripts in the order p, i, j, m. The ordering of nodal numbers p, i, j, m must follow a 'right-hand' rule obvious from Fig. 4-1. In this the first three nodes are numbered in an anticlockwise manner when viewed from the last one.

$$a_i = \det \begin{vmatrix} x_j & y_j & z_j \\ x_m & y_m & z_m \\ x_p & y_p & z_p \end{vmatrix} \quad b_i = -\det \begin{vmatrix} 1 & y_j & z_j \\ 1 & y_m & z_m \\ 1 & y_p & z_p \end{vmatrix} \tag{4-6}$$

$$c_i = -det \begin{vmatrix} x_j & 1 & z_j \\ x_m & 1 & z_m \\ x_p & 1 & z_p \end{vmatrix} \quad d_i = -det \begin{vmatrix} x_j & y_j & 1 \\ x_m & y_m & 1 \\ x_p & y_p & 1 \end{vmatrix}$$

The element displacement is defined by the 12 displacement components of the nodes as equation (4-7) with equation (4-8).

$$a^e = \begin{Bmatrix} a_i \\ a_j \\ a_m \\ a_p \end{Bmatrix} \tag{4-7}$$

$$a_i = \begin{Bmatrix} u_i \\ v_i \\ w_i \end{Bmatrix} a_j = \begin{Bmatrix} u_j \\ v_j \\ w_j \end{Bmatrix} a_m = \begin{Bmatrix} u_m \\ v_m \\ w_m \end{Bmatrix} a_i = \begin{Bmatrix} u_p \\ v_p \\ w_p \end{Bmatrix} \tag{4-8}$$

we can write the displacement of an arbitrary point as equation (4-9) with shape functions defined as equation (4-10) and I being a three by three identity matrix.

$$u = [IN_i, IN_j, IN_m, IN_p]a^e \tag{4-9}$$

$$N_i = \frac{a_i + b_i x + c_i y + d_i z}{6V}, N_j = \frac{a_j + b_j x + c_j y + d_j z}{6V}, \tag{4-10}$$

$$N_m = \frac{a_m + b_m x + c_m y + d_m z}{6V}, N_p = \frac{a_p + b_p x + c_p y + d_p z}{6V}$$

Once again the displacement functions used will obviously satisfy continuity requirements on interfaces between various element. This fact is a direct corollary of the linear nature of the variation of displacement.

2. Strain matrix

Six strain component are relevant in full 3-dimensional analysis. the strain matrix can now be define as equation (4-11) following the standard notation of Timoshenko's elasticity text. Using equation (4-4) to equation (4-9) it is an easy matter to verify that equation (4-12) in which equation (4-13) with other sub-matrices obtained in a similar manner simply by interchange of subscripts.

$$\varepsilon = \begin{bmatrix} \varepsilon_x \\ \varepsilon_y \\ \varepsilon_z \\ \gamma_{xy} \\ \gamma_{yz} \\ \gamma_{zx} \end{bmatrix} = \begin{bmatrix} \frac{\partial u}{\partial x} \\ \frac{\partial v}{\partial y} \\ \frac{\partial w}{\partial z} \\ \frac{\partial u}{\partial y} + \frac{\partial v}{\partial x} \\ \frac{\partial v}{\partial z} + \frac{\partial w}{\partial y} \\ \frac{\partial w}{\partial x} + \frac{\partial u}{\partial z} \end{bmatrix} = Su \tag{4-11}$$

$$\varepsilon = Ba^e = [B_i, B_j, B_m, B_p]a^e \tag{4-12}$$

$$B_i = \begin{bmatrix} \frac{\partial N_i}{\partial x} & 0 & 0 \\ 0 & \frac{\partial N_i}{\partial y} & 0 \\ 0 & 0 & \frac{\partial N_i}{\partial z} \\ \frac{\partial N_i}{\partial y} & \frac{\partial N_i}{\partial x} & 0 \\ 0 & \frac{\partial N_i}{\partial z} & \frac{\partial N_i}{\partial y} \\ \frac{\partial N_i}{\partial z} & 0 & \frac{\partial N_i}{\partial x} \end{bmatrix} = \frac{1}{6V} \begin{bmatrix} b_i, & 0, & 0 \\ 0, & c_i, & 0 \\ 0, & 0 & d_i \\ c_i, & b_i, & 0 \\ 0, & d_i, & c_i \\ d_i, & 0, & b_i \end{bmatrix} \qquad (4\text{-}13)$$

3. Elasticity matrix

With complete anisotropy the D matrix relating the six stress components to the strain components can contain 21 independent constants. In general, thus equation (4-14).

Although no difficulty presents itself in computation when dealing with such materials, since the multiplication will never be carried out explicitly, it is convenient to recapitulate here the D matrix for an isotropic material. This, in terms of the usual elastic constants E and ν, can be written as equation (4-15).

$$\sigma = \begin{bmatrix} \sigma_x \\ \sigma_y \\ \sigma_z \\ \tau_{xy} \\ \tau_{yz} \\ \tau_{zx} \end{bmatrix} = D(\varepsilon - \varepsilon_0) + \sigma_0 \qquad (4\text{-}14)$$

$$D = \frac{E(1-\nu)}{(1+\nu)(1-2\nu)} \begin{bmatrix} 1 & \frac{\nu}{(1-\nu)} & \frac{\nu}{(1-\nu)} & 0 & 0 & 0 \\ \frac{\nu}{(1-\nu)} & 1 & \frac{\nu}{(1-\nu)} & 0 & 0 & 0 \\ \frac{\nu}{(1-\nu)} & \frac{\nu}{(1-\nu)} & 1 & 0 & 0 & 0 \\ 0 & 0 & 0 & \frac{(1-2\nu)}{2(1-\nu)} & 0 & 0 \\ 0 & 0 & 0 & 0 & \frac{(1-2\nu)}{2(1-\nu)} & 0 \\ 0 & 0 & 0 & 0 & 0 & \frac{(1-2\nu)}{2(1-\nu)} \end{bmatrix}$$

(4-15)

4. Stiffness, stress, and load matrices

Finally, the element stiffness matrix in the 3-dimension and the finite element formulation could be expressed as the equations (4-16)~(4-17).

The general ij sub-matrix of the stiffness matrix will be a three by three matrix defined as equation (4-16) where V^e represents the volume of the elementary tetrahedron.

$$K_{ij}^e = B_i^T D B_j V^e \tag{4-16}$$

$$f_i^e = - B_i^T D \varepsilon_0 V^e \tag{4-17}$$

B. Compliance equations of flexure hinge

The formulation that follows is based on the following simplifying assumptions .

(1) The flexure hinges consist of two symmetric cutouts, as illustrated in Fig. 4-2.

(2) The flexure hinges are modeled and analyzed as small-displacement fixed-free Euler-Bernoulli beams subjected to bending produced by force and moments ; axial loading is also considered (see Fig. 4-3) while shearing and torsional effects are not taken into account.

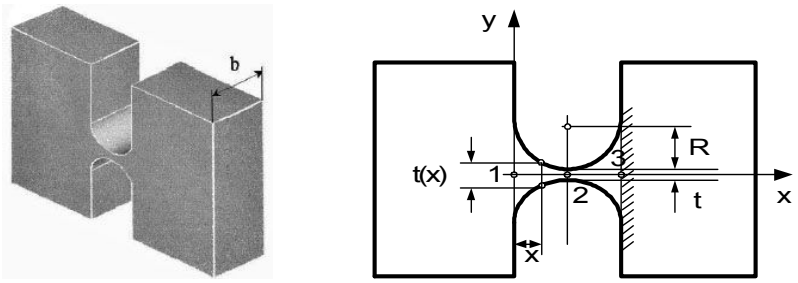

(a) Three-dimensional view (b) Front view with main parameters.

Fig. 4-2 Geometric configuration of a circular flexure hinge

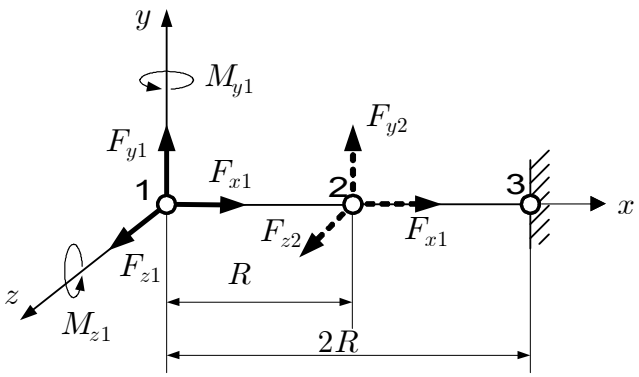

Fig. 4-3 Schematic representation of a flexure hinge with loading

A circular flexure hinge is defined by the geometric parameters indicated in Fig.1 Two sub-problems will be addressed in the following, namely the in-plane and out-plane compliant behavior of a flexure hinge. The in-plane compliant equations will be formulated with respect to translations along the y-and x-axes, and rotation about the z -axis. All the other degrees of freedom, namely : translation about the z-axis and rotation about the y-axis (torsional effects are neglected, as stated previously), will be analyzed as out-of-plane compliance equations. For displacement and loading components, the first subscript indicates the axis while the second one determines the point along the flexure longitudinal axis. For compliances, the first subscript points out the deformation and the second one indicates the load that produces that deformation[46].

1. In-of-plane compliance equations

The displacement-loading relationship at the free end 1 (see Fig.4-2) is of the from:

$$\begin{Bmatrix} \theta_{z1} \\ y_1 \\ x_1 \end{Bmatrix} = \begin{bmatrix} C_{\theta_z, M_z} & C_{\theta_z, F_y} & 0 \\ C_{y, M_z} & C_{y, F_y} & 0 \\ 0 & 0 & C_{x, F_y} \end{bmatrix} \begin{Bmatrix} M_{z1} \\ F_{y1} \\ F_{x1} \end{Bmatrix} \tag{4-18}$$

with $C_{\theta_z, F_y} = C_{y, M_z}$, according to the reciprocity principle. The Castigliano's second theorem is applied to evaluate the displacement vector in the left-hand side of equation (4-18) :

$$\begin{cases} \theta_{z1} = \dfrac{\partial U_{e,ip}}{\partial M_{z1}} \\ y_1 = \dfrac{\partial U_{e,ip}}{\partial F_{y1}} \\ x_1 = \dfrac{\partial U_{e,ip}}{\partial F_{x1}} \end{cases} \tag{4-19}$$

Where the in-plane elastic strain energy comprises bending and axial terms that are given in equation (4-20).

$$U_{e,i} = \frac{1}{2}\left(\int_t \frac{F_x^2}{EA(x)}dx + \int_t \frac{M_z^2}{EI_z(x)}dx\right) \tag{4-20}$$

$$F_x = F_{x1}, M_z = M_{z1} + F_{y1}x, A(x) = bt(x), I(x) = \frac{bt(x)^3}{12}$$

The formulation that follows is based on two non-dimensional parameters shown in Fig. 4-2, namely :

$$\beta = \frac{t}{2R} \tag{4-21}$$

The variable thickness $t(x)$, as shown Fig. 4-2, can be expressed as equation (4-22)

$$t(x)2(y) = 2R + t - [x(2R - x)]^{\frac{1}{2}} \tag{4-22}$$

Equation (4-22) is combined with equations (4-19)~(4-20) to formulate the compliance equations for circular flexure hinge.

$$C_{\theta_z, M_z} = \frac{6}{Ebt^2}\frac{1}{(2+\beta)}\left[\frac{3+4\beta+2\beta^2}{1+\beta} + \frac{6(1+\beta)}{\beta^{\frac{1}{2}}(2+\beta)^{\frac{1}{2}}}\arctan\left(1+\frac{2}{\beta}\right)^{\frac{1}{2}}\right] \tag{4-23}$$

$$C_{\theta_z, F_y} = -\frac{t}{2\beta}C_{\theta_z, M_z} \tag{4-24}$$

$$C_{y,F_y} = \frac{3}{2Eb}\frac{1}{(1+\beta)(2+\beta)^2\beta^3}[f_{e1}(\beta)+f_{e2}(\beta)] \quad (4\text{-}25)$$

$$f_{e1} = \beta\{3+\beta[6+\beta(11+8\beta+2\beta^2+\pi(1+\beta)(2+\beta^2))]\}$$

$$f_{e2} = 2\beta^{\frac{1}{2}}(2+\beta)^{-\frac{1}{2}}(2+\beta)^4(3-4\beta-2\beta^2)arctan(1+\frac{2}{\beta})^{\frac{1}{2}}$$

$$C_{x,F_x} = \frac{1}{Eb}[2(1+\beta)\beta^{-\frac{1}{2}}(2+\beta)^{-\frac{1}{2}}arctan(1+\frac{2}{\beta})^{\frac{1}{2}} - \frac{\pi}{2}] \quad (4\text{-}26)$$

2. Out-of-plane compliance equations

The out-of-plane compliance equations (4-27) are given in an equation similar equation (4-18). where, again, $C_{\theta_y,F_z} = C_{z,M_y}$, according to the reciprocity principle. The Castigliano's second theorem is applied again to evaluate the displacement vector in the left-hand side of equation (4-27). Further mathematical details are given in equation (4-28). It can be shown as equation (4-29) for the circular flexure hinge.

$$\begin{Bmatrix}\theta_{y1}\\ z_1\end{Bmatrix} = \begin{bmatrix}C_{\theta_y,M_y} & C_{\theta_y,F_z}\\ C_{z,M_y} & C_{z,F_z}\end{bmatrix}\begin{Bmatrix}M_{y1}\\ F_{z1}\end{Bmatrix} \quad (4\text{-}27)$$

$$\begin{cases}\theta_{y1} = \dfrac{\partial U_{e,o}}{\partial M_{y1}}\\ z_1 = \dfrac{\partial U_{e,o}}{\partial F_{z1}}\end{cases} \quad (4\text{-}28)$$

$$U_{e,o} = \frac{1}{2}\int_t \frac{M_y^2}{EI_y(x)}dx\ ,\ \begin{cases}M_y = M_{y1}+F_{z1}x\\ I_y(x) = \dfrac{b^3t(x)}{12}\end{cases}$$

$$C_{x,F_x} = \frac{b^2}{12}C_{\theta_y,M_y} \quad (4\text{-}29)$$

3. Precision of rotation

The relative rotation of two mechanical members that are connected by a conventional rotation joint is produced along an axis that passes through the geometric center of the joint, which is fixed provided one member is also fixed. In the case of a symmetric flexure hinge, the center of rotation (the geometric symmetry center of the flexure) is no longer fixed since the forces and moments acting on the flexure produce elastic deformations that alter its position.

The displacement of the rotation center of a flexure hinge (point 2 in Fig. 4-3), can be assessed by applying two fictitious loads, a horizontal one, F_{x2} and a vertical one, F_{y2} in addition to the actual load vector made up of M_{z1}, F_{y1} and F_{x1}.The Castigliano's second theorem is again utilized to find the displacements of the rotation center in the form:

$$\begin{aligned} y2 &= \frac{\partial U_{e,i}}{\partial F_{y2}} \\ x2 &= \frac{\partial U_{e,i}}{\partial F_{x2}} \end{aligned} \tag{4-30}$$

The elastic strain energy U_e is given in equation (4-20) and includes now the formal effects of F_{x2} and F_{y2}. The matrix-form equation that relates deformations to the load vector is similar to equation (4-18), namely;

$$\begin{Bmatrix} 0 \\ y_2 \\ x_2 \end{Bmatrix} = \begin{bmatrix} 0 & 0 & 0 \\ C_{12}' & C_{22}' & 0 \\ 0 & 0 & C_{33}' \end{bmatrix} \begin{Bmatrix} M_{z1} \\ F_{y1} \\ F_{x1} \end{Bmatrix} \tag{4-31}$$

The compliances in equation (4-31) define the offset of the rotation center and are calculated similarly to the 'full' compliance factors that were previously derived. The closed-form equations of $C_{12}^{'}$, $C_{22}^{'}$ and $C_{33}^{'}$ are given in the following for circular flexure hinge.

The closed-form compliance equations for circular flexures are equations (4-32)~(4-34).

$$C_{12,c}^{'} = -\frac{3}{2Ebt}\beta^{-1}(1+\beta)^{-1} \tag{4-32}$$

$$C_{22,c}^{'} = \frac{3}{4Eb}\beta^{-2}(2+\beta)^{-3}[f_{e1}^{'}(\beta) + f_{e2}^{'}(\beta)] \tag{4-33}$$

$$f_{e1}^{'}(\beta) = 12 + \beta\{2 - 2\beta[7 + \beta(5+\beta)] - \pi(2+\beta)^3\}$$

$$f_{e2}^{'}(\beta) = 2(1+\beta)[3(1+\frac{2}{\beta})^{\frac{1}{2}} + (1+\beta)^2(-3+4\beta+2\beta^2)]arctan(1+\frac{2}{\beta})^{\frac{1}{2}}$$

$$C_{33,c}^{'} = \frac{1}{4Eb}[4(1+\beta)\ \beta^{-\frac{1}{2}}(2+\beta)^{-\frac{1}{2}}arctan(1+\frac{2}{\beta})^{\frac{1}{2}} - \pi] \tag{4-34}$$

4. Stress considerations

The stresses can be evaluated from the displacement field, provided the latter is known, by either experimental measurement or prediction. Lobontiu et al.[51] mentioned that the maximum stress on a corner-filleted flexure hinge, when only the in-plane bending and axial effects are considered, can be expressed as

$$\sigma_{\max} = 6\frac{k_b}{bt^2}(M_{z1} + lF_{y1}) + \frac{k_a}{bt}F_{x1} \tag{4-35}$$

provided the stress concentration factors in bending kb and axial ka are specified (see,

for instance specialized textbooks like Peterson or Pilkey[55]~[56]). Equation (4-35) is also valid for both parabolic and hyperbolic flexure hinges. In order to express the load of equation (4-35) in terms of displacement, equation (4-18) can be written in terms of stiffness as

$$\begin{Bmatrix} M_{z1} \\ F_{y1} \\ F_{x1} \end{Bmatrix} = \begin{bmatrix} K_{\theta_z, M_z} & K_{\theta_z, F_y} & 0 \\ K_{y, M_z} & K_{y, F_y} & 0 \\ 0 & 0 & K_{x, F_x} \end{bmatrix} \begin{Bmatrix} \theta_{z1} \\ y_1 \\ x_1 \end{Bmatrix} \tag{4-36}$$

where the stiffness matrix can be determined by inverting the compliance matrix in equation (4-18). The stiffness factors are:

$$\begin{aligned} K_{\theta_z, M_z} &= \frac{C_{y, F_y}}{C_{\theta_z, M_z} C_{y, F_y} - C_{y, M_z}^2} \\ K_{y, M_z} &= \frac{C_{y, M_z}}{C_{\theta_z, M_z} C_{y, F_y} - C_{y, M_z}^2} \\ K_{y, F_y} &= \frac{C_{\theta_z, M_z}}{C_{\theta_z, M_z} C_{y, F_y} - C_{y, M_z}^2} \\ K_{x, F_x} &= \frac{1}{C_{x, F_x}} \end{aligned} \tag{4-37}$$

Substituting equations (4-36) and (4-37) into equation (4-35) results in

$$\sigma_{\max} = 6 \frac{k_b}{bt^2} \left[(K_{\theta_z, M_z} + l K_{y, M_z}) \theta_{z1} + (K_{y, M_z} + l K_{y, F_y}) y1 \right] + \frac{k_a}{bt} K_{x, F_x} x1 \tag{4-38}$$

Equation (4-37) and (4-38) can be utilized in evaluating the maximum normal stress at one end of the circular flexure hinge when the stress concentration factors are specified.

C. Finite element modeling

This research deals with stability of a super precision micro cutting machine that is a core unit of such a ultra-precision lathe, and analyzes the results depending on the hinge type and material change, using FEM analysis. By reviewing the stability, it is possible to achieve the effect of basic data collection for unit control and to reduce trials and errors in unit design and manufacturing.

In this research, The finite element modeling was proceeded with the well-distributed commercial program known as the MARC, and the MENTAT had carried out the finite element analysis for the pre/post-processing.

1. Mesh generation

We divided mesh densely in hinge surroundings. The elements of micrio stage are 3810 and the nodes are 2724, the elements of PZT are 234 and the nodes are 120, the elements of tool holder jig are 1672 and the nodes are 1740, the elements of tool holder are 606 and the nodes are 436, the elements of bite tip are 54 and the nodes are 42.

Element type is an eight-node, isoparametric, three-dimensional, arbitrary hexahedral. As this element uses trilinear interpolation functions, the strains tend to be constant throughout the element. The shear (or bending) characteristics can be improved by using alternative interpolation functions. This assumed strain procedure is flagged through the geometry option of software. This element is preferred over higher-order elements when used in a contact analysis. The stiffness of this element is formed using eight-point Gaussian integration. For nearly incompressible behavior, including plasticity or creep, it is advantageous to use an alternative integration procedure. This constant dilatation method which eliminates potential element locking is flagged through the geometry option of software. This element can be used for all constitutive relations.

2. 3-dimensional modeling

Each unit stage was completed with materials such as aluminum, copper, and steel. The modeling was completed with materials such as mild steel, tungsten, diamond for the tool holder jig, the tool holder, and the bite tip, respectively. The stage, the tool holder, and the bite tip were perceived as one rigid body. And the modeling of the piezoelectric element was estimated as the multi-layer being one rigid body. Table 4-1 displayed material properties of ultra-precision cutting unit. Moreover, the safety level standardized of the UPCU was evaluated through the analysis of the stress distribution and the characteristics of positioning depending on the general formations of the rectangular type and the round type of the elastic hinge. Fig. 4-4 shows the 3-dimensional modeling of the rectangular type and the round type illustrated from the MENTAT.

Table 4-1 Material properties of ultra-precision cutting unit

Material		E (kg/mm^2)	ν	ρ (kg/mm^3)	Nodes /Elements
Stage	Aluminum	7,000	0.32	2.70E-06	3810 / 2724
	Copper	9,800	0.3	8.60E-06	
	Steel	19,000	0.26	7.8 e-6	
AE0505D16(PZT)		4,400	0.34	2.50E-06	234 / 120
Mild steel (Tool Holder zig)		21,000	0.26	7.80E-06	1672 / 1740
Tungsten (Tool Holder)		68,730	0.22	1.48E-06	606 / 436
Diamond(Bite Tip)		114,550	0.2	3.50E-06	54 / 42

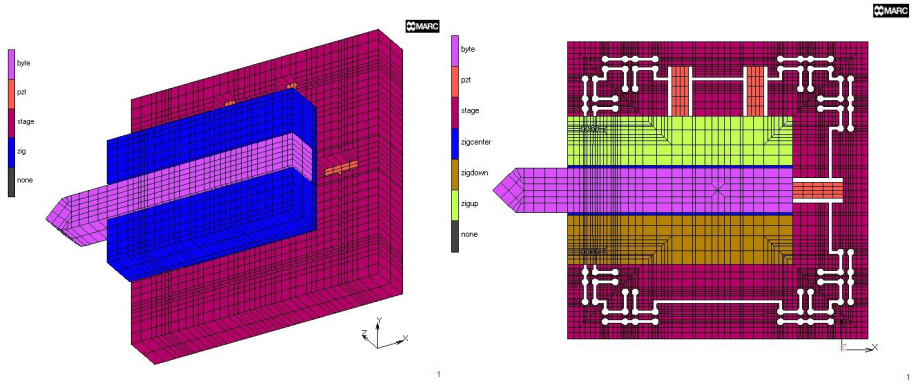

(a) Round type

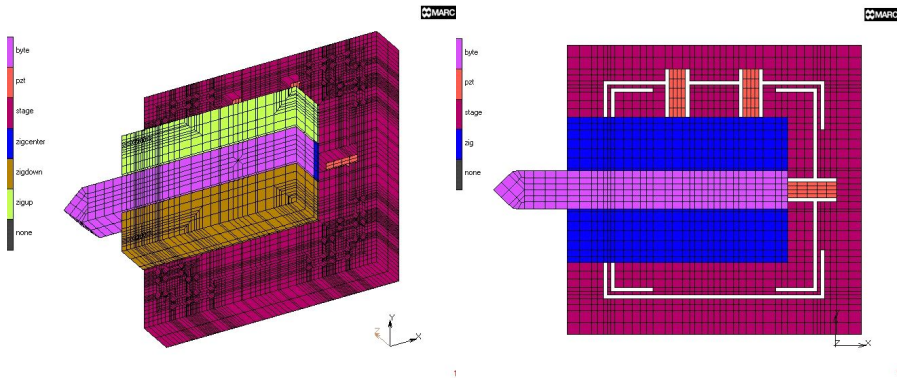

(b) Rectangular type

Fig. 4-4 FEM modeling of ultra-precision cutting unit.

3. The Measurement of three component cutting force

Since this system is intended to use in a ultra-precision lathe, there must be stability for three component cutting force generated in machining. (see APPENDIX B).

Therefore, FEM analysis was carried out by applying three-component force to the bite tip and the value, which was measured directly on the bite tip of a precision lathe, was applied. Since this system is used in ultra-precision machining, the amount of cutting is a very small value. But it was assumed that cutting was carried out to maximum 2mm with consideration of safety. Fig. 4-5 shows the value measured when the feed (f) amount was 0.3mm/rev, the speed (V) was 150 m/min, and work material was SM45C.

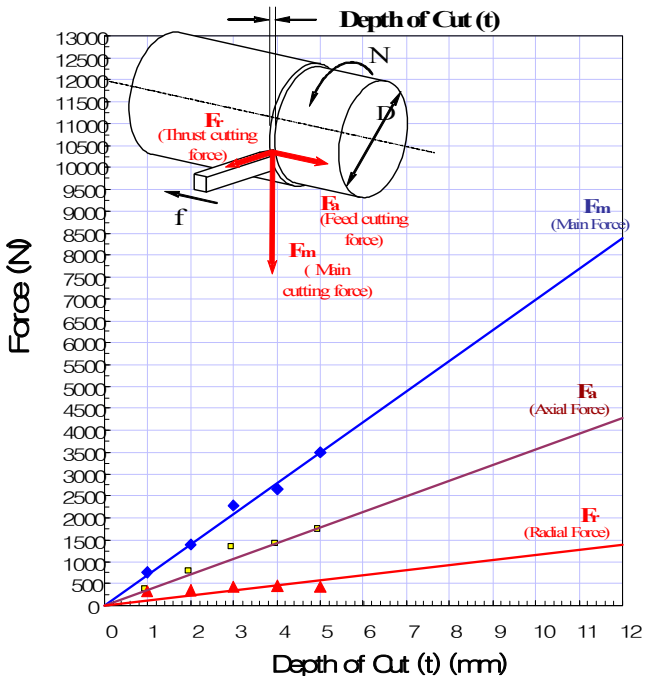

Fig. 4-5 Cutting force of micro cutting machine

D. Results and analysis of finite element interpretation

The hinge type is carefully designed for the elasticity and the stability. In this research, the round type and the rectangular type, rectangular type is simplified the round type, were designed and the elasticity and strength of a micro stage depending on the hinge type was analyzed using the FEM.

The micro stage for ultra-precision lathe must keep the hinge shape during cutting by which three-component force is applied to, and also minimize deformation by cutting force. The elasticity and strength depending on such a cutting force load was examined in this research.

Generally the material of the micro stage is duralumin with less thermal deformation. However, in this research it is aluminum of less strength, steel of more strength, and copper of intermediate strength to examine stability by checking elasticity and strength of the micro stage depending on material change, using the FEM.

The following three items were used to interpret stability.

(1) Examination of stability depending on the hinge type.
(2) Examination of stability depending on the cutting force load.
(3) Examination of stress distribution and displacement response capability depending on material change.

1. Examination of stability depending on hinge type

a. The boundary conditions

As shown in the Table 4-2, the boundary conditions of a model to examine stability depending on the hinge type were two states. The one was applied to the three components force, when cutting 2mm, at the bite tip of the aluminum micro stage model including the PZT in Figs. 4-6~4-7.

b. FEM results

The other was unloaded to PZT. Stress distribution and displacement on the hinge is shown in Figs. 4-6~4-7. Table 4-3 shows maximum shearing stress and displacement values depending on hinge types. When the hinge is a rectangular type, the PZT center displacement was maximum 32㎛ with 9.6㎛ for the round type, 28% of the rectangular type. Therefore, displacement control (maximum 18.6±2.0㎛) by the PZT was difficult because large displacement was represented in the rectangular type. It is considered as a secure structure because of, but the maximum shearing stress on the micro stage in the rectangular type was approximately twice that of the round type at the lower left or higher left, the safety coefficient was about 2.35~3.69. Therefore, it was confirmed that in terms of generated cracks at the hinge, both of the two types were secure, but the round type was stable. In order to check the above result, three-component force was applied to the byte tip and load of 85kg was given to the PZT, as shown in Fig. 4-8~4-9. Displacement control was difficult in the rectangular type when the maximum load of the PZT was 320kg, but it is considered that it can be controlled in the round type.

Also, when the PZT is loaded, the shearing stress tended to be reduced about 0.3~3.2% at the micro stage hinge. Such reduction of the shearing stress is considered to be. It is caused by loaded resistance of the PZT for the axial force of the bite tip (reduction of hinge deformation).

Table 4-2 Boundary conditions of stability depending on hinge type

Boundary conditions	
PZT outside	Fixed
Stage outside	Fixed
PZT/Stage contact area	Treated by Contact problem
Contact Problems	Applied the deformable body both PZT and Stage Friction coefficients : Coulum friction "1"
Loading at bite tip (kg)	Thrust cutting force (25), Feed cutting force (100), Main cutting force(-140)
Material	Aluminum
PZT load (kg)	0, 85

Table 4-2 FEM analysis results depending on the hinge type

Hinge Type		Rectangular		Round(Circle)	
PZT load (kg)		0	85	0	85
τ_{max} on Stage(㎏/㎟)		4.455	2.212	2.844	4.468
Crack (Safety Factor)		No (2.35)	No (2.36)	No (3.57)	No (-3.69)
Right-center PZT disp.(㎛)	X	2.42738	-6.14675	1.74979	-4.70866
	Y	18.3965	20.2603	6.27462	6.04134
	Z	-14.1908	-15.5782	-3.08502	-3.0668
Left-top PZT disp.(㎛)	X	-32.1401	-31.8275	-6.43469	-6.09568
	Y	11.8526	3.34388	9.58757	3.0348
	Z	5.16686	5.17251	0.366429	0.406138
Right-top PZT disp.(㎛)	X	0	0	0	0
	Y	0	-8.87839	0	-8.87839
	Z	0	0	0	0

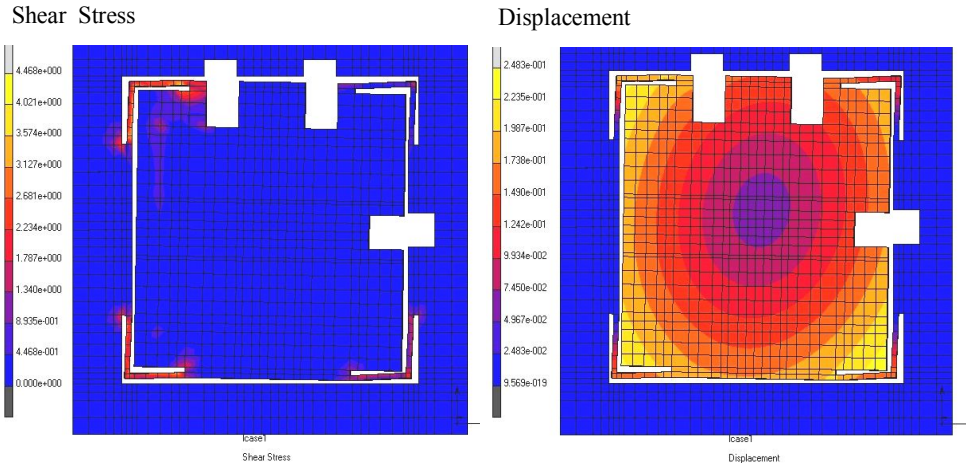

(a) Von-mises stress distribution (b) Deformation

Fig. 4-6 FEM analysis result of rectangular type (without PZT loading)

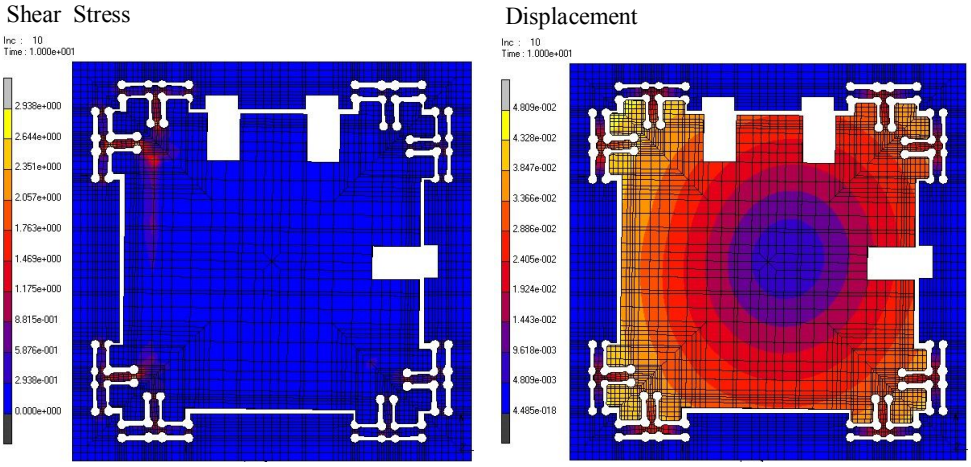

(a) Von-mises stress distribution (b) Deformation

Fig. 4-7 FEM analysis result of round type (without PZT loading)

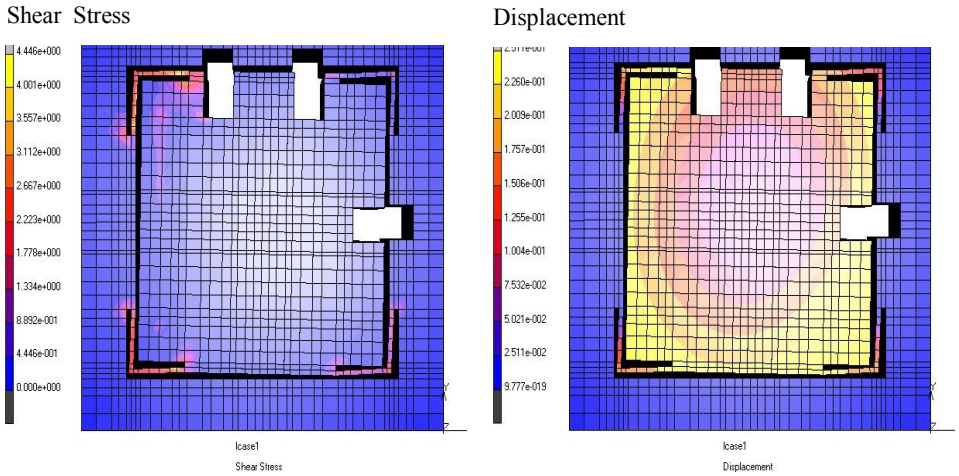

(a) Von-mises stress distribution (b) Deformation

Fig. 4-8 FEM analysis result of rectangular (Within PZT loading)

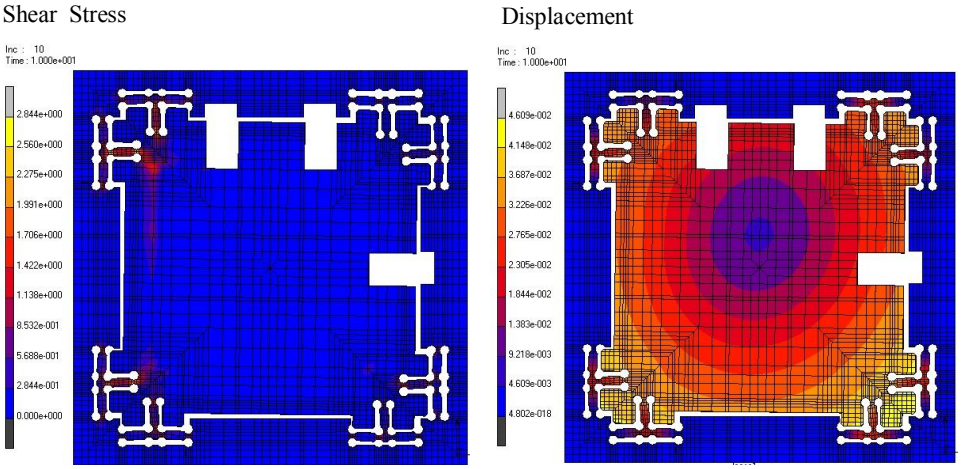

(a) Von-mises stress distribution (b) Deformation

Fig. 4-9 FEM analysis result of round type. (Within PZT loading)

2. Examination of stability of micro stage depending on cutting force load

a. The boundary conditions

As shown in the Table 4-4, the boundary conditions of a model to examine stability depending on the cutting force load at the bite tip. It is applied to the three components force, when cutting 2mm, at the bite tip of the aluminum, copper and steel micro stage model not including the PZT in Fig. 4-10.

b. FEM results

The following is about displacement properties of a micro stage when three component cutting force is applied in a model not including the PZT. As shown in Fig. 4-10(a) and Fig. 4-10(b), displacement was definitely stable in the round type. When the material of the micro stage was steel in Fig. 4-10(c), displacement stability was excellent depending on the cutting force load. Therefore, displacement in the rectangular type was approximately 8 times that in the round type. Since considerable deformation arises by the cutting force, it is considered that displacement control stability will be lowered by the PZT. Displacement stability was better with stronger materials. Table 4-5 shows displacement at the micro stage peak with which the PZT will get contact.

Table 4-4 Boundary conditions depending on the cutting force

Boundary conditions	
PZT	Excluded, No Mech
Stage outside	Fixed
PZT/Stage contact area	Treated by Contact problem
Contact Problems	Applied the deformable body both PZT and Stage Friction coefficients : Coulum friction "1"
Loading at bite tip (kg)	Thrust cutting force (25), Feed cutting force (100), Main cutting force(-140)
Material	Aluminum, Steel

Table 4-5 FEM analysis results depending on the cutting force

Stage hinge Type		Rectangular	Round	
Stage material type		Aluminum	Aluminum	Steel
Right-Center PZT disp.(㎛)	X	56.8241	6.43605	2.445
	Y	89.4994	1.4453	0.0566193
	Z	19.9862	3.0915	1.21577
Left-Top PZT disp.(㎛)	X	187.1	29.9456	11.6798
	Y	276.148	35.8934	13.9607
	Z	-102.494	-13.1903	-5.09165
Right-Top PZT disp.(㎛)	X	186.79	29.4776	11.4329
	Y	163.37	13.5308	5.2457
	Z	-39.2176	-3.94369	-1.572742

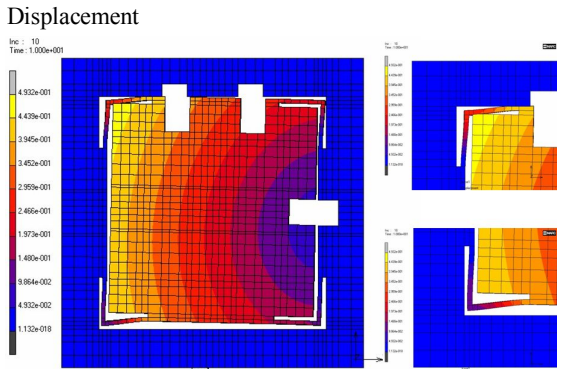

(a) Aluminum (rectangular type)

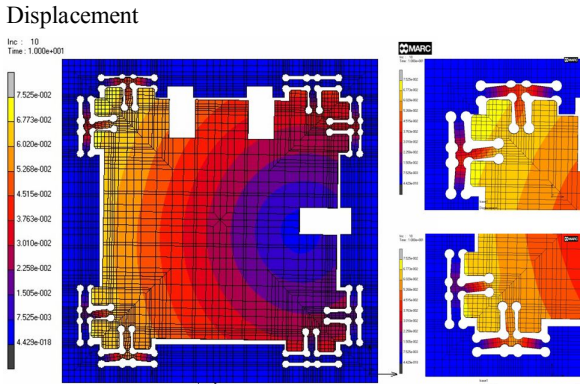

(b) Aluminum (round type)

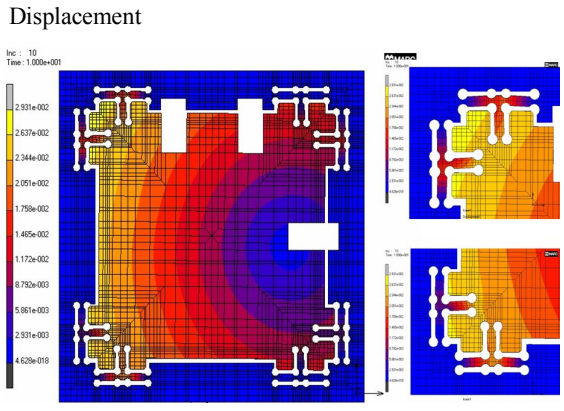

(c) Steel (round type)

Fig. 4-10 Deformation of rectangular type and round type

3. Examination of stability depending on material change (Without PZT)

a. The boundary conditions

As shown in the Table 4-6, the border condition was that the micro stage edge was fixed, the PZT was excluded in order to check stability of only the micro stage, and three component cutting force was applied to the bite tip.

b. FEM results

The micro stage materials were aluminum, copper and Steel. The material of a micro stage generally used is duralumin, but aluminum was applied whose physical properties are similar to duralumin in terms of strength. Therefore, aluminum for soft material, steel for strong material and copper for intermediate property were used for FEM interpretation to check their characteristics.

As a result of examination of stability depending on micro stage material, stress concentration occurred at the hinge, but the safety coefficient was 2.86~5.57. Cracks did not occur at the hinge in all of the three materials, which means they are safe. As the micro stage material was stronger, the maximum shearing stress across the micro stage increased by 2.6~7.1% as compared with aluminum. Therefore, in terms of strength, the stability of the micro stage for three component cutting force was more secure in stronger material, but there was no crack in aluminum, which is soft material. Fig. 4-11 shows FEM interpretation results of each material for stress distribution. Table 4-7 shows the result.

Table 4-6 Boundary conditions on stability depending on the material change

Boundary conditions	
PZT	Without PZT, No PZT mesh
Stage outside	Fixed
PZT/Stage contact area	Treated by Contact problem
Contact Problems	Applied the deformable body both PZT and Stage Friction coefficients : Coulum friction "1"
Loading at bite tip (kg)	Thrust cutting force (25), Feed cutting force (100), Main cutting force(-140)
Material	Aluminum, Copper, Steel

Table 4-7 Stress distributions depending on the material change

Hinge Type	Round(Circle)		
Material	Aluminum	Copper	Steel
τ_{max} on Stage(㎏/㎟)	3.676	3.771	3.936
Yielding stress(㎏/㎟)	21	42	40
Criterion Factor "Y"(㎏/㎟)	7.352 (-100%)	7.54(-102.60%)	7.872(-107.10%)
Safety Factor	2.86	5.57	5.08
Crack	No	No	No

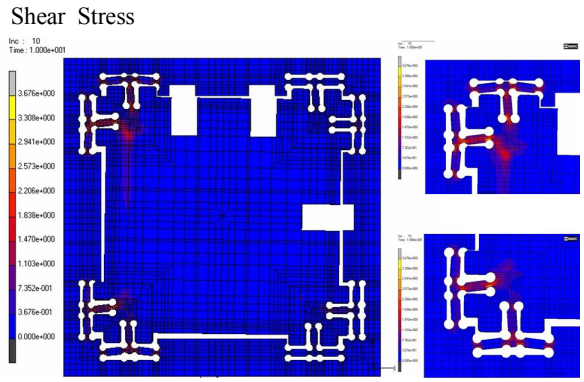

(a) Aluminum

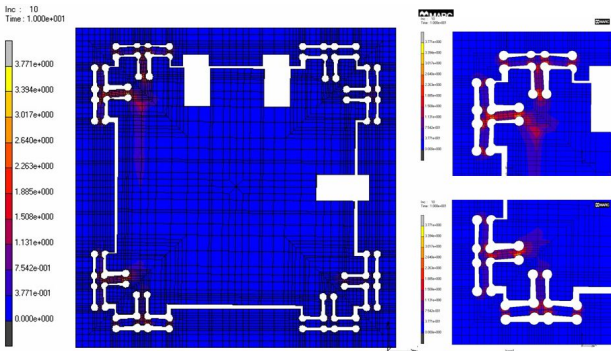

(b) Copper

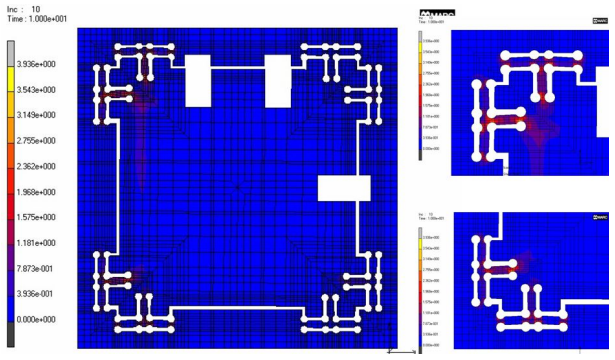

(c) Steel

Fig. 4-11 Max. shear stress distribution of micro stage

4. Examination of stability depending on material change (Within PZT)

a. The boundary conditions

As shown in the Table 4-8, the border condition was that the micro stage edge was fixed, it was applied load of 85kg to the PZT, and three component cutting force was not applied to the bite tip.

b. FEM results

The following describes displacement response at bite tips by applying load of 85kg to the PZT in the round type. This is intended to check how the response characteristics change depending on material change. As the result of examination of the displacement response at the bite tip depending on the weighted PZT, the stronger the material of the micro stage was, the less displacement response was obtained. Table 4-9 shows FEM interpretation result depending on the material change of the micro stage.

Fig. 4-12 shows displacement characteristics at the micro stage and the bite tip depending on material change. In terms of displacement response, it is required to select softer material than stronger material for a micro stage.

Table 4-8 Boundary conditions on stability depending on the material change

Boundary conditions	
PZT Side	Fixed
Stage outside	Fixed
PZT/Stage contact area	Treated by Contact problem
Contact Problems	Applied the deformable body both PZT and Stage Friction coefficients : Coulum friction "1"
Loading at bite tip (kg)	Thrust cutting force (25), Feed cutting force (100), Main cutting force(-140)

Table 4-9 Displacement responses depending on the material change

Hinge Type		Round (Circle)		
PZT load (kg)		85		
Disp. of bite tip	Material	Aluminum	Copper	Steel
	X(㎛)	-21.2377	-15.5298	-8.31574
	Y(㎛)	-41.9567	-30.6252	-16.339
	Z(㎛)	0.163368	0.078523	-0.0031655

Displacement

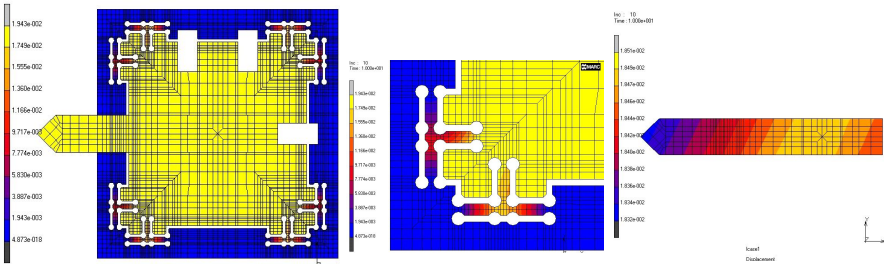

(a) Aluminum

Displacement

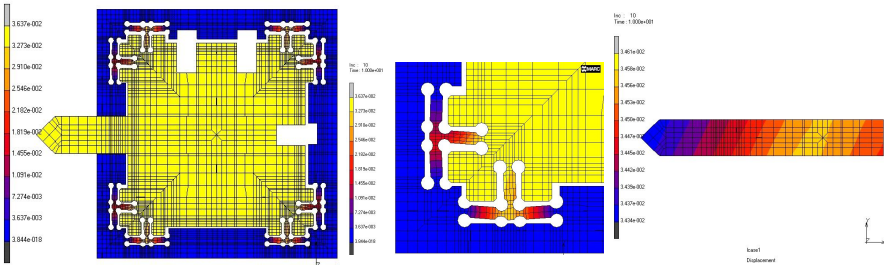

(b) Copper

Displacement

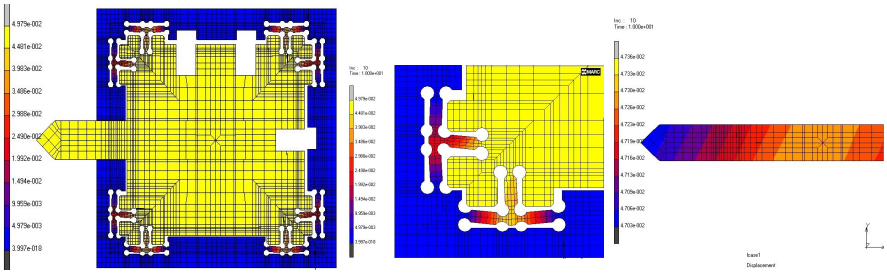

c) Steel

Fig. 4-12 Displacement response of micro stage

E. Validity verification of stability analysis through an experiment

We used the laser interferometer (Renishow RLE10) as the displacement sensor to micro position the micro-stage and the DSP Board (dSPACE ds1103) as the micro-stage control system. The schematic diagram of micro-stage displacement data acquisition system is shown in Fig. 3-8. Displacements of the PZT applied with voltages between 0V~100V were measured by the laser interferometer and the measured data were analyzed by FEM. The actual and FEM data of the micro-stage center displacement were compared and the results are shown in Fig. 4-13. Table 4-10 and Fig. 4-13 show the PZT displacements, which were input to the FEM micro-stage model, the resulting displacement at the bite tip of micro-stage, and FEM displacement results. They also show the deviation of the bite tip of micro-stage displacement between the actual data and FEM analysis data.

The results in Fig. 4-14 and Table 4-10 show that the FEM displacement data are similar to the actual displacement data obtained by operating the micro-stage; the error ratio was 3.53%. It is error ration, between experimental and numerical analysis calculated from the average of standard deviation. With these results, we were able to design the most reliable, optimal model of the micro-stage. Fig. 4-14 show the result of resolution experiment.

Table 4-10 Displacement data of PZT, FEM and micro-stage

Input	PZT Disp.(㎛)	Stage Disp.(㎛)	FEM Disp.(㎛)	FEM vs Stage Disp.(㎛)
0 V	0	0	0	0
10 V	0.563	0.389	0.32	0.0488
20 V	1.29	0.843	0.731	0.0793
30 V	2.11	1.34	1.2	0.099
40 V	3.02	1.88	1.72	0.113
50 V	4	2.45	2.28	0.12
60 V	5.05	3.04	2.87	0.12
70 V	6.12	3.64	3.47	0.12
80 V	7.18	4.22	4.08	0.099
90 V	8.23	4.79	4.68	0.0778
100 V	9.18	5.3	5.21	0.0636
90 V	8.7	4.98	4.94	0.0283
80 V	8.07	4.58	4.59	0.00707
70 V	7.34	4.15	4.17	0.0141
60 V	6.51	3.67	3.7	0.0212
50 V	5.59	3.14	3.17	0.0212
40 V	4.59	2.58	2.61	0.0212
30 V	3.51	1.97	1.99	0.0141
20 V	2.38	1.33	1.35	0.0141
10 V	1.2	0.662	0.681	0.0134
0 V	0	0	0	0

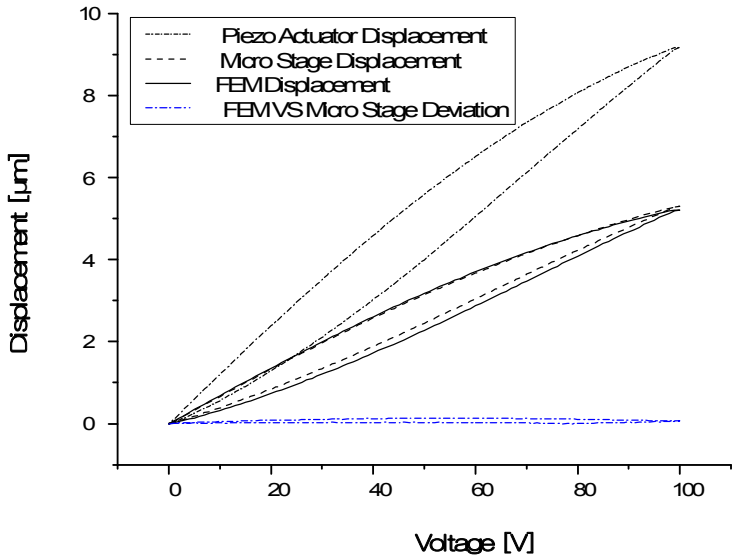

Fig. 4-13 Hysteresis curve of UPCU

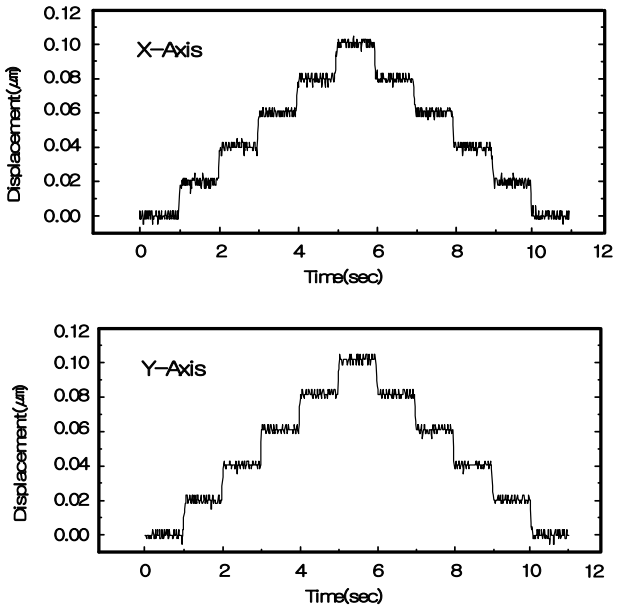

Fig. 4-14 The result of resolution experiment

F. Summary

The purpose of this research is to determine which hinge type and material to use when we design a micro stage for ultra-precision lathe. FEM interpretation was applied in order to reduce number of trials and errors in manufacturing UPCU, and it was intended to check the tendency. Also we wish to verify validity of stability analysis through experiment. The result is described below.

(1) The round hinge type was stable in terms of cutting force load.

(2) When applying three materials of aluminum, copper and steel, no crack occurred and it was secure for all the materials.

(3) When load was applied to the PZT and cutting force was not applied, better displacement response was obtained in softer material.

(4) The deviation between FEM data and actual data obtained by driving the micro stage was 3.53%, which was less than the allowable engineering deviation with use of FEM; this low deviation value verifies the validity of the FEM used in our study.

(5) We could construct system that have 10nm resolution performance. Based on result that stability analysis and an experiment execute Nano position control to basic.

V. THE MACHINING PRECISION IMPROVEMENT DUE TO THE REAL-TIME COMPENSATION FOR THE MOTION ERROR BY UPCU

The ultra-precision cutting based on the single crystal diamond tool would require the shaft and the transfer structure which enabled the ultra-precision nano motion unlike the general lathe installed with the tipped tools. Moreover, there is an increasing demand of the ultra-precision lathe requiring larger machining diameter along with more delicate machining precision. And as the stroke of the slide was elongated to the hundreds of mm range, the high resolution and the motion precision throughout the full stroke were required. This would be responsible for manufacturing finances to increase exponentially. However, even if the structural components had obtained high degree of the precision, the machining precision would have limitations, due to the massive ㎛ range of errors composed of the motion errors of the transferring system, the rotational error of spindles, and the thermal expansion of the workpiece. Viz., there should be more critical considerations in components such as the motion error of the nano order and the environmental error for the nm-ultra-precision lathe unlike that of the general lathe. The ultra-precision error compensation system was suggested in order to elevate the machining precision through the real-time observation of the error inducing agents and conducting compensation by the UPCU. The UPCU was able to precisely observe the spindle and the motion precision of the transferring system by the PZT, which real-timely compensated the motion error with the relatively small quantity of cutting unit and the tool holder that was driven minutely. Furthermore, the temperature compensation received a feedback from values of UPCU which real-timely compensated for the thermal deformation being affected by the spindle, the transferring system material types and corresponding structural changes.

A. The motion characteristics of the UPCU

1. The motion error

If the guide structure was utilized in the rigid body to aid the process of motion, there would be an motion process with 6-degrees of freedom. The stages were designed to limit the degree of freedom to control the direction of motion. Since the guide structure was incapable of locking 5 degrees of freedom adequately to have only 1 degree of freedom for the motion, thus 5 motion errors would be induced to all 6 motion errors as the positional errors of the transfer direction began to interfere. The 6 motion errors as shown in Fig. 5-1 could be labeled as the positional error, the straight error from the horizontal and the vertical directed 2-degrees of freedom, the roll error from the rotary coinciding with the transfer direction, the pitch error from the rotary being perpendicular to the horizontal direction, and the yaw error of the rotary being perpendicular to the vertical direction[45].

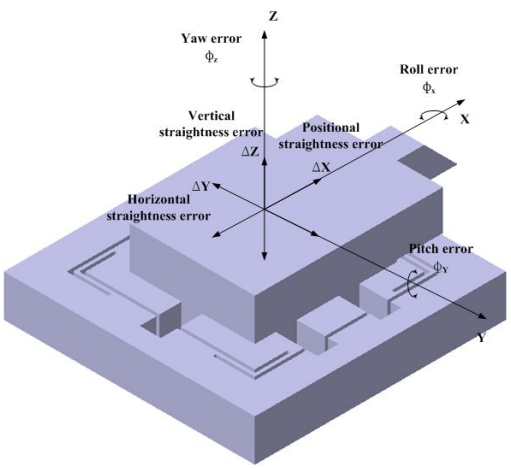

Fig. 5-1 Six motion error in a UPCU

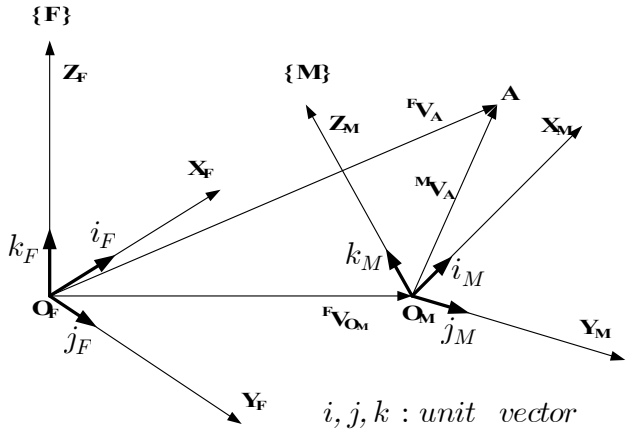

Fig. 5-2 Translational mapping

The equation (5-1) could be formulated from combination of the series of vectors such as the vector $\overrightarrow{{}^{F}V_{A}}$ from the origin of the fitted coordinate to the discretionary position 'A' of the kinetic coordinate, the rotational matrix ${}^{F}_{M}R$ regarding the fitted coordinate respect to the kinetic coordinate, the vector $\overrightarrow{{}^{M}V_{O}}$ of the kinetic coordinate from the origin and the vector $\overrightarrow{{}^{M}V_{A}}$ regarding the kinetic coordinate to the discretionary position 'A'. Furthermore, the equation (5-2) could be formulated by expressing the matrix of the sums of the rotation matrix plus all the vectors represented above. Ultimately, the modified matrix would be displayed as ${}^{F}_{M}T$ of the equation (5-3).

$$\overrightarrow{{}^{F}V_{A}} = \overrightarrow{{}^{M}V_{O_M}} + {}^{F}_{M}R \cdot \overrightarrow{{}^{M}V_{A}} \tag{5-1}$$

$$\begin{bmatrix} X_F \\ Y_F \\ Z_F \\ 1 \end{bmatrix} = \begin{bmatrix} i_F \cdot i_M & i_F \cdot j_M & i_F \cdot k_m & i_M + j_M + k_M \\ j_F \cdot i_M & j_F \cdot j_M & j_F \cdot k_m & i_M + j_M + k_M \\ k_F \cdot i_M & k_F \cdot j_M & k_F \cdot k_m & i_M + j_M + k_M \\ 0 & 0 & 0 & 1 \end{bmatrix} \begin{bmatrix} X_M \\ Y_M \\ Z_M \\ 1 \end{bmatrix} \tag{5-2}$$

$$[{}^{F}V_{A}] = [{}^{F}_{M}T][{}^{M}V_{A}] \tag{5-3}$$

There were 3 types of angular errors when the stage was transferred towards the direction of X axis, which were the roll error ϕ_X, the pitch error ϕ_Y, and the yaw error ϕ_Z as shown in Fig. 5-2. The associated rotational matrices were the equation (5-4)~(5-6) respectively.

$$R_X(\phi_X) = \begin{bmatrix} 1 & 0 & 0 \\ 0 & cos\phi_X & sin\phi_X \\ 0 & -sin\phi_X & cos\phi_X \end{bmatrix} \tag{5-4}$$

$$R_Y(\phi_Y) = \begin{bmatrix} cos\phi_Y & 0 & sin\phi_Y \\ 0 & 1 & 0 \\ -sin\phi_Y & 0 & cos\phi_Y \end{bmatrix} \tag{5-5}$$

$$R_Z(\phi_Z) = \begin{bmatrix} cos\phi_Z & -sin\phi_Z & 0 \\ sin\phi_Z & cos\phi_Z & 0 \\ 0 & 0 & 1 \end{bmatrix} \tag{5-6}$$

The Equation (5-7) represented the overall rotational matrices where the kinetic coordinate had rotated in the amount of the roll error ϕ_X surround the X axis, followed by the Y axis rotation in the amount of the pitch error ϕ_Y and ended the rotation sequence with the Z-axis rotation in the amount of the yaw error ϕ_Z.

$${}^{F}_{M}R_{XYZ}(\phi_{X,}\phi_{Y,}\ \phi_Z) =$$

$$\begin{bmatrix} c\phi_Z c\phi_Y & -c\phi_Z s\phi_Y s\phi_X + s\phi_Z s\phi_X & c\phi_Z s\phi_Y c\phi_X + s\phi_Z s\phi_X \\ s\phi_Z c\phi_Y & s\phi_Z s\phi_Y s\phi_X + c\phi_Z s\phi_X & -s\phi_Z s\phi_Y c\phi_X + c\phi_Z s\phi_X \\ -s\phi_Y & -c\phi_Y s\phi_X & c\phi_Y c\phi_X \end{bmatrix} \tag{5-7}$$

The $c\phi_X$ and $s\phi_X$ were abbreviation for the $cos\phi_X$ and $sin\phi_X$, respectively. As the roll

error ϕ_X, the pitch error ϕ_Y, and the yaw error ϕ_Z were completely defined, these error were only applicable in the same sequence rotation they were defined. However, due to the guide structure, the rotational errors would relatively insignificant where the rotational matrices of the equation (5-7) and the equation (5-11) would be presumed acceptable on the basis of the equation (5-8), the equation (5-9), and the equation (5-10).

$$sin\phi \ = \phi \tag{5-8}$$

$$cos\phi \ = 1 \tag{5-9}$$

$$sin\phi \ sin\phi \ = 0 \tag{5-10}$$

$$^{F}_{M}R_{XYZ}(\phi_X,\phi_Y,\phi_Z) = \begin{bmatrix} 1 & -\phi_Z & \phi_Y \\ \phi_Z & 1 & -\phi_X \\ -\phi_Y & \phi_X & 1 \end{bmatrix} \tag{5-11}$$

The origin of the kinetic coordinate could be perceived as the focal point of the transfer table where as the discretionary position 'A' could be a discretionary point on the transfer table, thus the vector $\overrightarrow{^{M}V_A}$ would have a consistent equation (5-12).

$$^{M}V_A = \begin{bmatrix} x_A \\ y_A \\ z_A \end{bmatrix} \tag{5-12}$$

The objective position vector $\overrightarrow{^{F}V_{R,O}}$ of the fixed focal point on the guide surface of the transfer table had coincided with its fixed coordinate axis and kinetic coordinate axis to the initial position when the vector expressed as the equation (5-13), thus the objective position vector of the discretionary point 'A' could be expressed as the equation (5-14).

$$^{F}V_{R,O} = \begin{bmatrix} X_R \\ Y_R \\ Z_R \end{bmatrix} \tag{5-13}$$

$$ {}^{F}V_{R,A} = \begin{bmatrix} X_R + x_A \\ Y_R + y_A \\ Z_R + z_A \end{bmatrix} \tag{5-14} $$

As the equation (5-15) had displayed, the positional error ΔX and the straightness error of horizontal and perpendicular directions ΔY,ΔZ determined the actual coordinate ${}^{M}V_O$ of the transfer table origin considering of the fixed coordinate.

$$ {}^{F}V_O = \begin{bmatrix} X_R - \Delta X \\ Y_R - \Delta Y \\ Z_R - \Delta Z \end{bmatrix} \tag{5-15} $$

The combinations of equations (5-2), (5-11), and (5-15) had regarded as the equation (5-16) for the coordinate of the discretionary point 'A' regarding the machining coordinate.

$$ {}^{F}V_O = \begin{bmatrix} X_R - \Delta X + x_A - y_A\phi_Z + z_A\phi_Y \\ Y_R - \Delta Y + x_A\phi_Z + y_A - z_A\phi_X \\ Z_R - \Delta Z - x_A\phi_Y - y_A\phi_X + z_A \end{bmatrix} \tag{5-16} $$

The value of errors from the equations (5-14) and (5-16) regarding the discretionary point 'A' was displayed as the equation (5-17).

$$ {}^{F}D_A = \begin{bmatrix} \Delta X + y_A\phi_Z + z_A\phi_Y \\ \Delta Y - x_A\phi_Z + z_A\phi_X \\ \Delta Z + x_A\phi_Y - y_A\phi_X \end{bmatrix} \tag{5-17} $$

Mainly, there are two types of errors, a systematic error which is recoverable by a software and an uncountable random error. The positional precision was able to measure

and control using the stiffness of the guide structure and the position sensitive detector of the transfer directions to correct only one of 6 error components, such as the positional error ΔX or only some of 5 other error components by the software support. However, the positional precision of the stage required the serve micron, thus the random errors could not be disregarded. In order to compensate for components in the random errors, the structural planning is required to enable 6 degrees of freedom in the table for simultaneous measurements and corrections.

The equation (5-18) was formulated depending upon the stiffness of X, the surface translating error Y, and the yaw error ϕ_Z regarding the angular error during the machining process.

$$ {}^{F}E_A = \begin{bmatrix} \Delta X + y_A\phi_Z \\ \Delta Y - x_A\phi_Z \\ \phi_Z \end{bmatrix} \tag{5-18} $$

2. The driving mechanism of the UPCU

The micro driving equipment manipulated the elastic deformation through the bending in many case because of the advance qualities to maintain the simple form, the flawless motion, the absence of frictions or backlash, and relatively rapid response.

Namely, the motions were fixed only by the direction initiated thus the other directions would not have to be counted for. In order to apply to 3 axial kinetic UPCU, the x and y directed translating motion and Θ directed rotational motion should be modified to activate simultaneously. This concept of modified bending structure was described as Fig. 5-3(a). Fig. 5-4 displayed the micro stage structure developed from the modified bending component in Fig. 5-3(b), and it composed of the PZT and the single structured elastic bending component (APPENDIX : Drawing of UPCU).

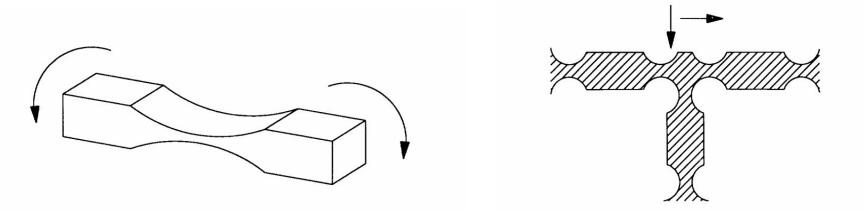

(a) Single- axis flexure (b) Modified flexure structure

Fig. 5-3 Basic flexure structure and its application for 3- axis fine motion mechanism

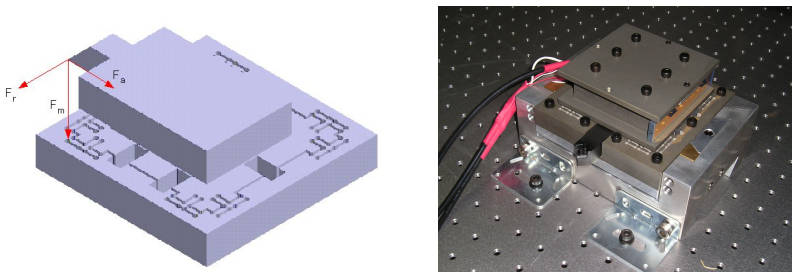

Fig. 5-4 Flexure structure of UPCU

The tool holder might experience relative positional changes due to the changes in elastic bending components originated from the positional changes of the PZT regarding the impressed voltage in UPCU. Table 5-1 displayed performance of PZT. The positional change of the tool holder could be calculated from the arrangements of each PZT and the values deviated at the corresponding position. Fig. 5-5 displayed the geometrical model of the above. More importantly, the relativity of the voltage input and the positional changes of output in the PZT should be verified. The vectors U_p, ${}^M U_p$ could be defined as the equations (5-19) and (5-20).

$$U_p = [u_{p1} \;\; u_{p2} \;\; u_{p3}]^T \tag{5-19}$$

$${}^M p_p = [x_p \;\; y_{p1} \;\; y_{p2}]^T \tag{5-20}$$

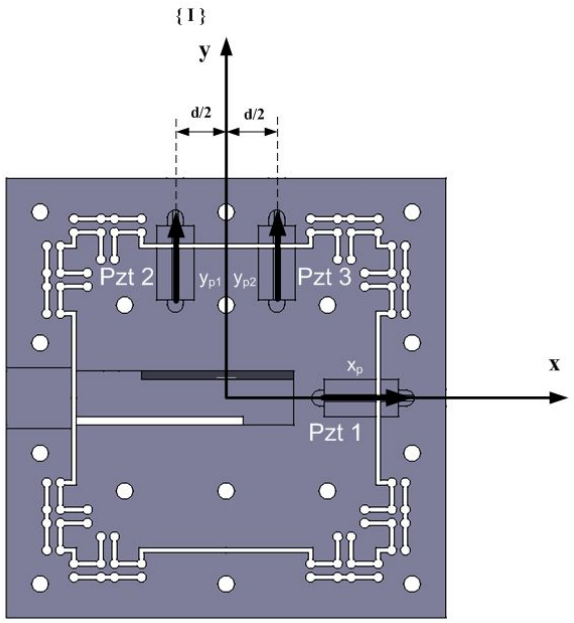

Fig. 5-5 Kinematic model of the UPCU

Table 5-1 Performance of PZT

Max. stroke (μm)	Length (mm)	El. capacitance (μF)	Stiffness (N/μm)	Resonance frequency (kHz)
40~50	46	3.6	25	20
Prestress force = Max. tensile force			300N	
Max. load force			1800N	
Max. force generation			1800N	
Open loop sensitive at 1μN noise for actuator			0.05nm	

Whereas, u_{pi} and ${}^{M}p_{pi}$ represented the "i" number of the positional change for the voltage input and the PZT respectively. Generally, the input voltage U_p and the output positional change ${}^{M}U_p$ of the PZT dynamically coupled and contributed mutual effects. This relationship could be represented as the equation (5-21).

$$ {}^{M}p_p(s) = A(s)U_p(s) \tag{5-21} $$

$$ {}^{M}p_{p,i}(s) = \sum_{j=1}^{3} a_{ij}(s)u_{pj}(s) \qquad (i = 1, 2, 3) $$

Whereas, $a_{ij}(s)$ was the coefficient for interconnecting the "j" number of impressed voltage due to the PZT and i number of output displacement of the PZT which could be further expressed as the equation (5-22).

$$ a_{ij}(s) = b_{ij}\, g_{ij}(s) \tag{5-22} $$

b_{ij} represented the legitimate benefit of the displacement of the PZT respect to the

impressed voltage, where as $g_{ij}(s)$ represented the common distinctive quality. Moreover, the displacement (x_p, y_{p1}, y_{p2}) of the PZT and the relative tool holder displacement could be geometrically defined as the equation (5-23).

$$M\begin{bmatrix} x \\ y \\ \theta \end{bmatrix} = \begin{bmatrix} 1 & 0 & 0 \\ 0 & \frac{1}{2} & \frac{1}{2} \\ 0 & -\frac{1}{d} & \frac{1}{d} \end{bmatrix} \begin{bmatrix} x_p \\ y_{p1} \\ y_{p2} \end{bmatrix}$$

$$^{M}P_O = {}^{M}_{p}J\ {}^{M}P_p \tag{5-23}$$

The relationship of the voltage input and the relative tool holder displacement could be as the equation (5-24) by considering the equations (5-21)~(5-23).

$$^{M}P_O(s) = {}^{M}_{p}JA(s)\ U_p(s) = {}^{M}_{p}JB\ G(s)\ U_p(s) \tag{5-24}$$

B. The control algorithm

The UPCU composed of the PZT and the hinge structure were dependent upon the PID controller which was shown in Figs. 5-6~5-7 after noticing the difficulty in modeling for the PZT and complex structured hinge.

The UPCU eliminated the vibrating disturbance as its first compensation. The disturbance originated from the lathe had the natural frequency ranging from approximately 10~ 40 Hz which was estimated originated within the low frequency area. The early stage of PID gain was analyzed based on the frequency response characteristics. Base on prior result, there were replicated experiments which the loop gain at the low frequency would be induced as the loop gain at the high frequency deduced in order to achieve the proper responses. Table 5-2 demonstrated corresponding PID gains prior to this method.

Each gain of PID could be represented as the equations (5-25)~(5-26), the relativity with output regarding the voltage input was defined as the equation (5-27). Thus the output of PID controller was defined as the equation (5-28).

$$\frac{Y_{\beta}(s)}{U(s)}=\beta,\quad \frac{Y_{\alpha}(s)}{U(s)}=\frac{\alpha s}{\alpha Ts+1},\quad \frac{Y_{\gamma}(s)}{U(s)}=\frac{\gamma}{s} \tag{5-25}$$

$$s=\frac{2}{T}\times\frac{z-1}{z+1} \tag{5-26}$$

$$y_{\beta}[i]=\beta\ u[i]$$

$$y_{\alpha}[i]=\frac{2\alpha-1}{T(2\alpha+1)}y_{\alpha}[i-1]+\frac{2}{T(2\alpha+1)}(u[i]-u[i-1]) \tag{5-27}$$

$$y_{\gamma}[i]=y_{\gamma}[i-1]+\frac{\gamma T}{2}(u[i]-u[i-1])$$

$$\frac{U_{AMP}}{E}=\beta+\frac{\gamma}{s}+\frac{\alpha s}{\alpha Ts+1} \tag{5-28}$$

Table 5-2 Control parameters of PID controller in micro servo for simulation

Definition	Symbol	Value
Proportional gain	β	0.01
Integral gain	ν	800
Differential gain	α	5×10^{-7}
Sampling time	T	0.0002 s
Converted constant by table position for voltage	Ka	$7.9\times10^{6}\ v/m$

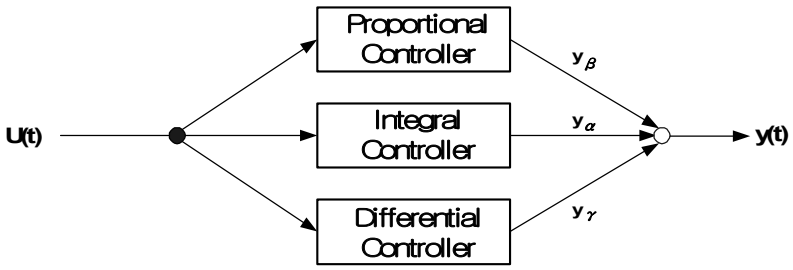

Fig. 5-6 Block diagram of PID controller

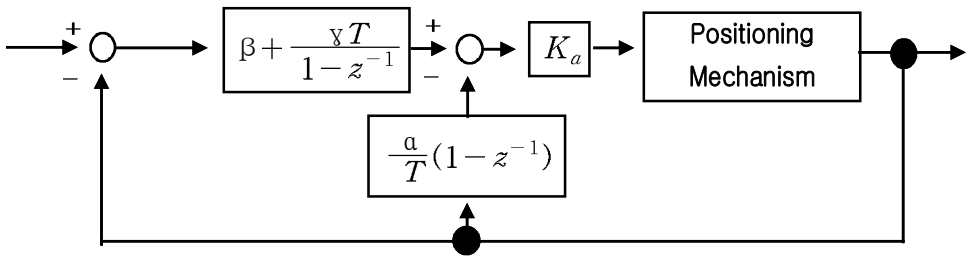

Fig. 5-7 Block diagram of PID controller in global servo for simulation

C. The systematic structure and the error measurement

The ultra-precision lathe studied for this research was UP-2 manufactured from Hwacheon machine tool company, which featured the performances including 0.05 ㎛ of the resolution and 0.5 ㎛ of the repeatability. As described in Fig. 5-8, UP-2 had each axial being independent formations and minimized the interference among slides during the transfer procedure.

Generally, the components which critically influenced the machining precision of the nm grade ultra-precision Cutting were the motion error due to the spindle rotations, the straightness of the X-axial transferring system which directly affected the product formation, and thermal expansion of the spindle and the transferring system caused by the temperature change.

In order to compensate the error components mentioned above, the system had real-timely measured the straightness of the X-axial transferring system by 10 nm resolution of the laser encoder and the spindle rotation. The measured errors were real-timely compensated by considering the thermal expansion coefficient of specific material type and corresponding structure by the temperature change followed by the UPCU feedback procedure to complete the compensation of the errors. Fig. 5-9 showed the systematic structure. Fig. 5-10 showed the measurements of the straightness error of the X-axial transferring system in the range of 200 mm using 1 nm resolution of the laser interferometer (ML10; Renishaw) to observe the X axial motion in a steady speed by considering the machining center as the origin. As the graph had indicated, 200 mm stroke had approximately 0.5 ㎛ of straightness error and this could be compensated through the error calculation regarding the absolute position in the control algorithm of UPCU. In order to measure the thermal expansion of the spindles, the laser nanogage (OPTRA Nanogage100) was installed with the jig and it was installed in the front of

spindle to avoid any interference. The measurement was made by rotating the spindles. Generally, the thermal expansion errors were composed of the low frequency components thus the formation error of the high frequency components were was extracted through the low frequency filter. Fig. 5-11 showed the result of the thermal expansion error created by the spindle of the ultra-precision lathe during machining.

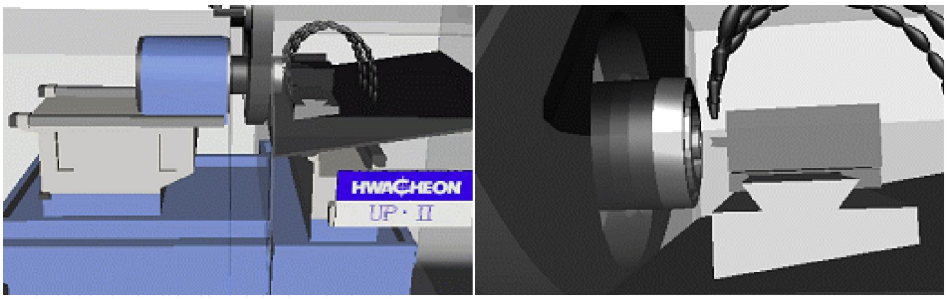

Fig. 5-8 The structure of UP-2

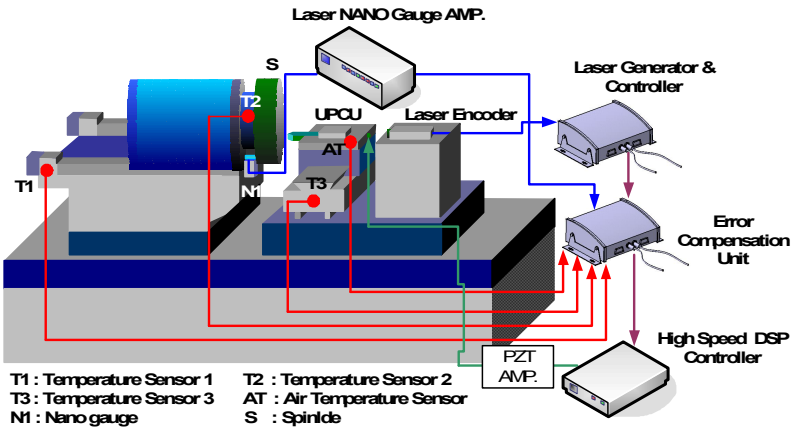

Fig. 5-9 Schematic diagram of error compensation system

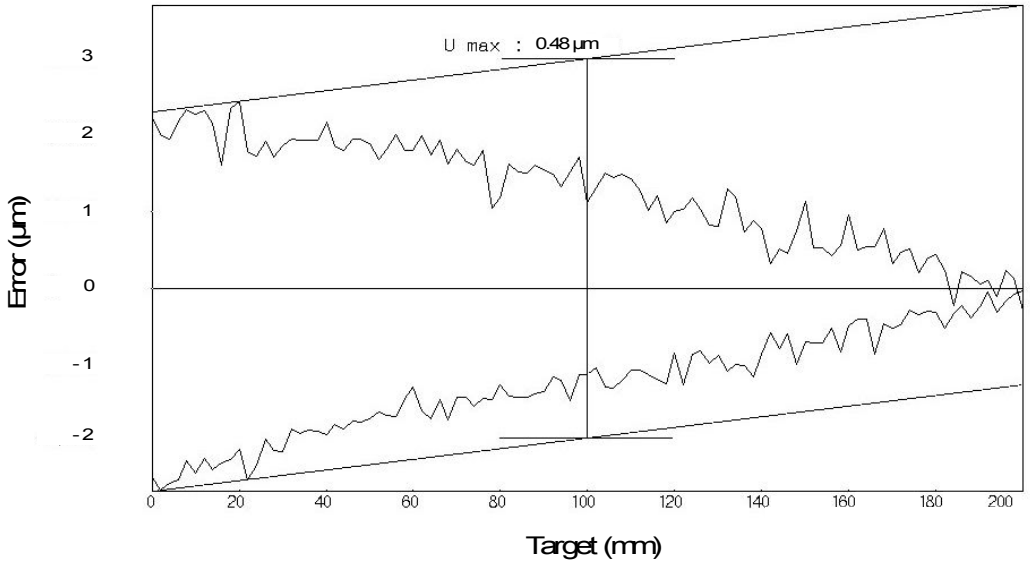

Fig. 5-10 The straightness error of X-axis motion

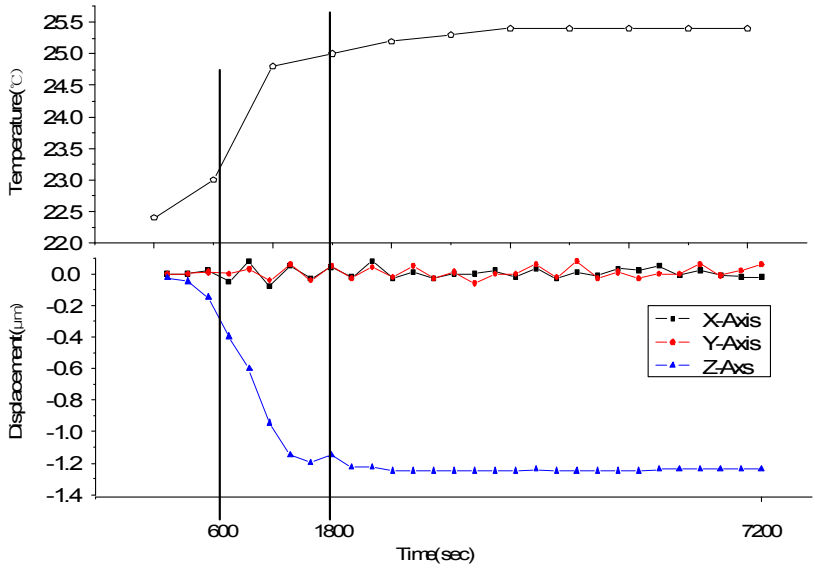

Fig. 5-11 The thermal displacement of spindle

D. The ultra-precision positioning performance of the UPCU

In order to evaluate the ultra-precision positioning capability of the UPCU, there were two position experiment conducted disregarding the error value measured earlier. In the first experiment, there was 20nm step pulse input as the linear displacement and enable to move up to 100 nm on the vibroisolating table where the external vibration was not notified to UPCU, which was then followed by addition 20nm step to reverse back to 0 nm. Each displacement was regulated to move 0.57 arcsec in 0.114 arcsec step. Fig. 5-12 confirmed that there was no problem observed in detailed driving of 20nm step and 0.114 arcsec step. Moreover, there were ±5nm and 0.114 arcsec for the linear displacement and the position determining capability, respectively. In the second experiment, the positioning test was conducted with UPCU attaching to the lathe and having all the other aspects consistent as above. As shown in the Fig. 5-12, the overall performance of the detailed driving was lower than that of the vibroisolating table presence. However, the UPCU had reduced the vibration peak value 800nm to 20nm range in the presence of 3000rpm spindle spinning, ; thus the compensation for the motion errors in the X, Y, Θ directions could be assumed as satisfactory for this experiment.

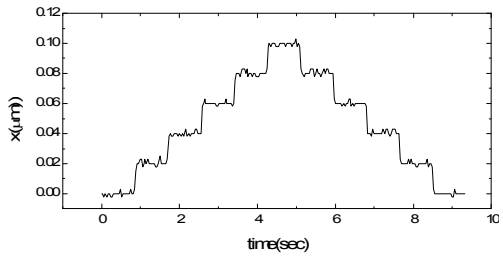

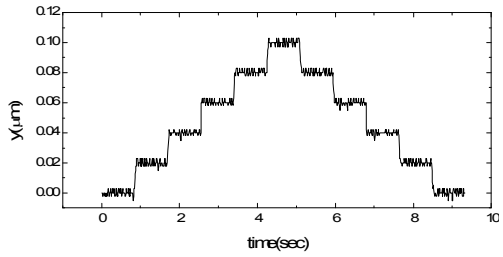

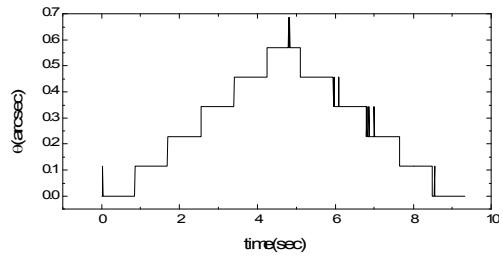

Fig. 5-12 20nm motion of UPCU (Vibroisolating table)

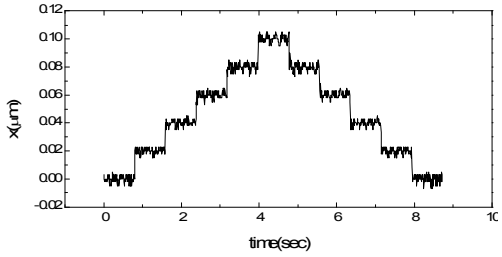

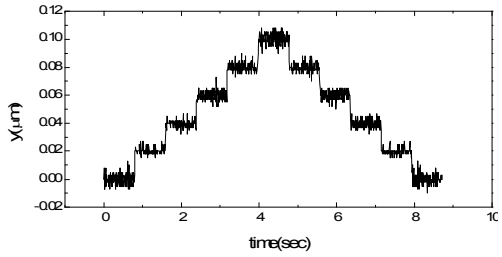

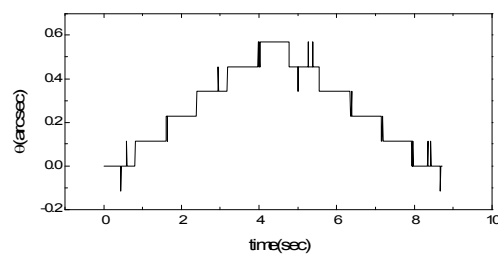

Fig. 5-13 20nm motion of UPCU (3000 rpm on spindle)

E. The tracking error test for UPCU

Prior to machining test, the X-axial straightness error which was pre-measured for this procedure and the thermal expansion error of the spindle were input for UPCU to conduct a tracking test. The DSP board (ds1103) from dSpace company was used as the controller with the application of PID control algorithm. The ultra-precision lathe conducted for this experiment had 1.5㎛ range of overall error component with the low frequency component. Therefore, the control was set up through the results of 1.5㎛, 3㎛ of the amplitude test and the sine input response test having 1 Hz as a period. The associated unit input response test was based on the control set up previously in order to determine the error compensation capability of UPCU.

Figs. 5-14, 5-15 showed the results of the experiment, where there was approximately 50 nm of the tacking error which could be perceived that the compensation was adequate. Therefore, this result would indicate that there would not be any problems in objective to develop the machining precision in the real machining experiment.

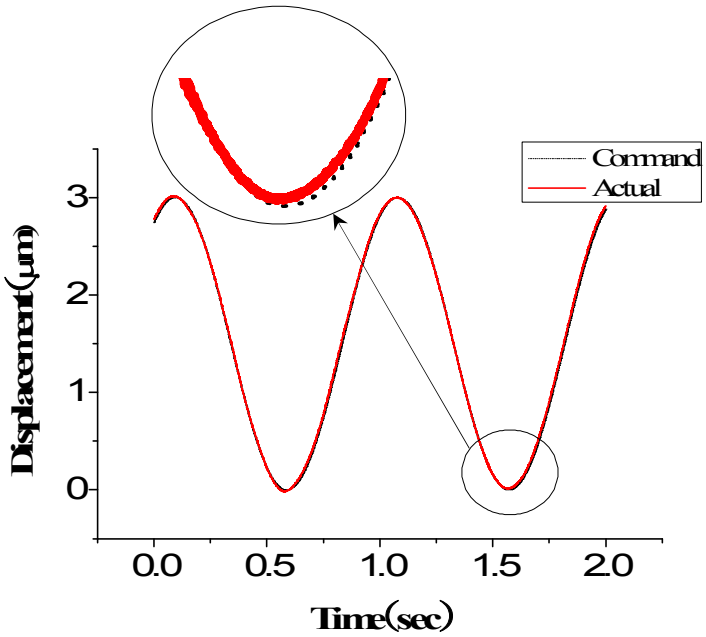

(a) Displacement

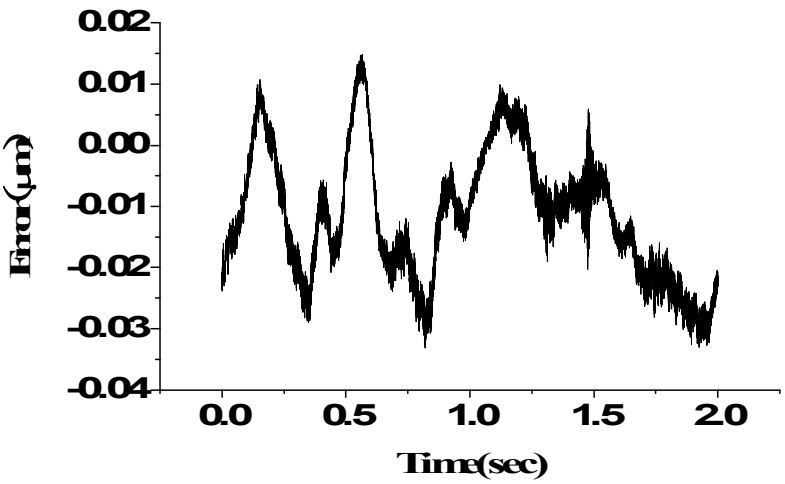

(b) Error

Fig. 5-14 The tracking error of UPCU (3㎛)

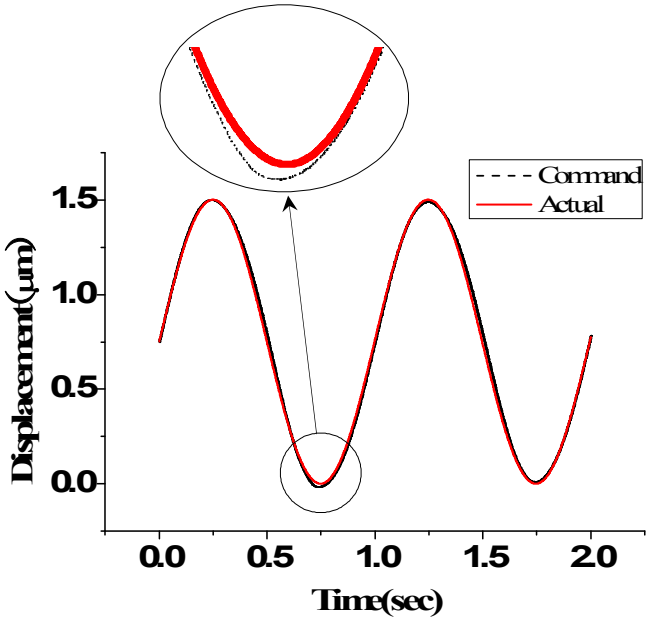

(a) Displacement

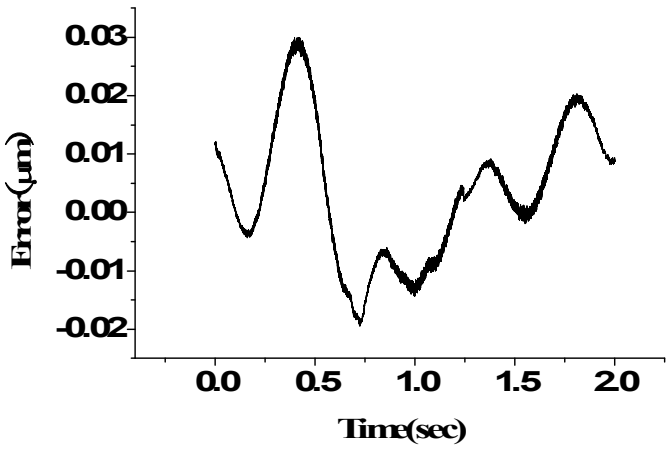

(b) Error

Fig. 5-15 The tracking error of UPCU (1.5㎛)

F. Summary

In this research we had suggested the system that allowed real-time measurements for the X-axial straightness error and the thermal expansion error of the spindle which was then followed by the feedback in UPCU to improve the machining precision extensively.

(1) The measurement for the thermal displacement of spindle had indicated that the thermal expansion period of spindle was 35min, and there was 0.5㎛ of error detected.

(2) The positional determining capability test of UPCU suggested that in the presence of the vibroisolating table, there were 10nm and 0.144 arcsec of resolutions for the X, Y direction and the Θ-direction, respectively. The UPCU installed lathe with 3000rpm spindle rotation demonstrated that there were 20nm and 0.144 arcsec of resolutions detected for the X,Y direction and the Θ-direction, respectively.

(3) The real-time error compensation result of UPCU had displayed approximately 50nm of the tracking error capability.

VI. CONCLUSIONS

In this research, the laser application instrument in order to measure the environmental and the operative errors have been developed and for employed for extensive developments in planning, safety analysis and control to complete UPCU application which was capable of collecting the series of errors mentioned earlier and providing real-time corrections.

This research was designed real-time measurement and correction of any deviations in variety of areas to achieve a compensation system through more effective optical fibre laser encoder than the encoder resolution which was currently used in the existing lathe. The deviations for a real-time correction were composed of followings; the surrounding air temperature, the thermal deviations of the machining materials, the thermal deviations in spindles, and the overall thermal deviation occurred due to the machine structures. And the main objective was to manufacture the UPCU by applying for the real machining condition and confirming the safety level with the FEM analysis, and to Improve the machining precision through the ultra-precision positioning and the real-time operative error compensation. In addition, there was to improve the machining precision of the existing lathe and concluded as following.

(1) In the case of no displacement without considering environment error compensation, it is found that the zero-point value is 0~23nm/℃ of error in temperature variation. In the case of no displacement compensated by environmental error, it is found that the zero point value is 0~4nm/℃ of error in temperature variation. The amplitude value is ±15.5ppb of frequency response under no displacement not compensated by environmental error and room temperature. The amplitude value is ±1.1ppb of frequency response

under no displacement compensated by environmental error and room temperature.

(2) The round hinge type was stable in terms of cutting force load. When applying three materials of aluminum, copper and steel, no crack occurred and it was secure for all the materials. When load was applied to the PZT and cutting force was not applied, better displacement response was obtained in softer material. The deviation between FEM data and actual data obtained by driving the micro stage was 3.53%, which was less than the allowable engineering deviation with use of FEM ; this low deviation value verifies the validity of the FEM used in our study. Based on result that stability analysis and an experiment execute nano position control to basic, we could construct system that have 10nm resolution performance.

(3) The measurement for the thermal displacement of spindle had indicated that the thermal expansion period of spindle was 35min, and there was 0.5㎛ of error detected. The positional determining capability test of UPCU suggested that in the presence of the vibroisolating table, there were 10nm and 0.144 arcsec of resolutions for the X, Y direction and the Θdirection, respectively. The UPCU installed lathe with 3000rpm spindle rotation demonstrated that there were 20nm and 0.144 arcsec of resolutions detected for the X, Y direction and the Θ-direction, respectively. The real-time error compensation result of UPCU had displayed approximately 50nm of the tracking error capability.

REFERENCES

1. Lee J. W, " 1 Nano Opened World, " 11th Science adventure, 2001.
2. Kim J. D, "A Study on the Waviness Compensation System of Ultra-precision Machining," KSMTE, Vol. 7. No. 6, pp. 132-140., 1998.
3. Kwac L. K., Kim J. Y., Cho Y. T., "FE Analysis According to Hinge Condition of Micro Stage for Micro Cutting Machine," Key Engineering Materials, Vols. 274-276, pp. 343-348., 2004.
4. Thomas J. R. Hughes, "The Finite Element Method," Prentice-Hall International Editions, pp. 90-91,, 1987.
5. Shiraishi M., Uehara K., "In-Process Control of Workpiece Dimension in Turning," Annal of The CIRP, Vol. 28, pp. 333-337., 1979.
6. Lee E. S., Lee J. K., Suto T., "A Simulation System for the Eatablishment of Grinding Operation Standards," JSPE, Vol. 54 No. 12, pp. 81-86., 1988.
7. Park K. H., Kim J. Yl., Kwac L. K., "Simulation and Control Performance Evaluation of Ultra-precision Single Plane X-Y Stage," KSMTE, Vol. 11 No. 5, pp. 65-72., 2002.
8. Kim J. Y., Kwac L. K., Han J. H., Kim H. W., Shimokobe A., "A Study on the Optimal Design using FEM for Micro Stage," KSPE, Vol. 19 No.10, pp. 60-65., 2002.
9. Kim H. S., Kim E. J., "Feed-Forward Control of Fast Tool Servo for Real-Time Correction of Spindle Error in Diamond Turning of Flat Surfaces," International Journal of Machine Tools & Manufacture, Vol. 43 , pp. 1177-1183., 2003.
10. "Future and Emerging Technologies," European Commission, 1999.
11. Kohno T., Okazaki Y., Ozawa N., Mitui K. and Omoda M., "In-Process Measurement and a Work-pice Referenced Form Accuracy Control

System(WORFAC):Concept of the Method and Preliminary Experiment," JSPE, Vol. 11 No.1, pp.9-11., 1989.

12. Peter J., "Diamond Turning of Non-rotationally Symmetric Surfaces," Ph. D Theses of North Carolina State University. 1990.
13. Patterson S. R., Matgab E. B., "Design and Testing of a Fast Tool Servo for Diamond Turing," JSPE, Vol. 7, No.3, pp.123-128., 1985.
14. Donaldson P. R., Patterson S. R., "Desing and Construction of a Large, vertical Axis Diamond Turning Machine.", Proc. SPIE, Vol. 433, pp.62-67., 1983.
15. Lubarsky S. V., Sobolev V. G., Shevtsov S. E., "Optical Surface Fabrication on Ultra Precision Machines," SPIE, Vol. 1266, pp.226-236., 1990.
16. Geyl R., "Design and Farication of Three Mirror Flat Field Anastigmat for High Resolution Earth Observation," SPIE, Vol.2210, pp.739-745., 1994.
17. Kim J. Y, Lee H. N, Kwac L. K, Han J. H, Cho Y. T, Jun C. G, "Control Performance Evaluation of Ultra Precision Positioning Apparatus," Proc. ISIM 2000 , pp. 252-255., 2000.
18. Shiraishi M., Uehara K., "In-Process Control of Workpiece Dimension in Turning," Annal of The CIRP, Vol. 28, pp. 333～337., 1979.
19. Becker P., Dorenwendt K. et al, "Absolute Measurement of the (220) Lattice Plane Spacing in a Silicon Crystal," Phys. Rev. Lett. 46, 1540., 1981.
20. Simokohbe A., "Control performance of Lead screw Positioning with Intelligent Control Methods," JSPE, Vol. 64. No. 11, pp. 1627～1632., 1998.
21. Furukawa E., Mizuno M., Hojo T.,"A Twin-Type Piezo-Driven Translation Mechanism," JSPE, Vol.28, No. 1, pp. 70-75., 1994.
22. P. E. Dupont, "Avoiding Stick-Slip Through PD Control," IEEE Transaction on Automatic Control, Vol. 39, No. 5, pp. 1302., 1994
23. Messner W., Horowitz R., "Identification of a Nonlinear Function in a Dynamical System," Journal of Dynamic Systems, Measurement and Control, Vol. 115, 1993.

24. Holmes M., Trumper D., "Magnetic/Fluid-Bearing Stage for Atomic-scale Motion Control," JSPE, Vol. 18 No. 1, pp. 38-49., 1996.
25. Bae D. S., Hwang R. S., Haug E. J., "A Recursive Formulation for Real-Time Dynamic Simulation of Mechanical Systems," ASME Journal of Mechanical Design, Vol. 113, pp. 158-166., 1991.
26. Lin T. C., Yae K. H., "Linearization of the Dynamics of Closed-Chain Mechanical Systems," Mechanics of Sructures and Machines, Vol. 25, Iss. 1, pp. 21-40., 1997.
27. Benjamin C. Kuo, "Automatic Control Systems," Prentice Hall. Englewood Cliffs. N. J 07632, pp. 689-699, 1994.
28. Sato K., "Performance Evaluation Lead screw Positioning System with Five Kinds og Control Methode(2nd Report)," JSPE Vol. 63. No. 12, pp. 1759～1763., 1997.
29. Nakazawa H., "Principles of Precision Engineering," Gordon and Breach Science Publishers, pp. 75-82, pp. 140-167., 1994.
30. Smith S. T., Chetwynd D. G., "Foundation of Ultra- Precision Mechanism Design," Gordon and Breach Science Publishers, pp.95-128., 1992.
31. Keith Bowen D., "Development in Nanotechnology," Gordon and Breach Science Publishers, pp. 95-129., 1992.
32. Sakuta S., Ogawa K., Ueda K., "Experimental Studies on Ultra-precision Positioning," JSPE, Vol. 27, No. 3, pp. 235～240., 1993.
33. Oiwa T., Kanko K., Kaneko T., Kyusojin A., "High-Rigidity Multi-Degrees-of-Freedom Fine Motion Mechanism using Piezoelectric Actuators," JSPE, Vol. 60 No. 9, pp. 1355-1359., 1994.
34. Nagaya K., Ishikawa M., "A Noncontact Permanent Magnet Levitation Table with Electromagnetic Control and its Vibration Isolation Method using Direct Disturbance Cancellation Combining Optimal Regulators," IEEE Transactions of Magnetics, Vol. 31 No. 1, pp. 885-896., 1995.
35. Franchi, Claudio G., "General Formulation in Rigid Multibody Dynamics," Int. J.

for Numerical Methods in Eng., Vol. 38 No. 12, pp. 1985-2016., 1995.

36. Nakanishi T., Yin X., Shabana A., "Dynamics of Multibody Tracked Vehicles Using Experimentally Identified Modal Parameters," ASME Journal of Dynamic Systems Measurements and Control, Vol. 118 Iss. 3, pp. 499-507., 1996.
37. Keltie R. F., Ozisik H., "Development and Implementation of a High Speed Loop Control Technique for Micro-positioning of Mechanical Structures," JSPE, Vol 58 No. 4, pp. 225., 1989.
38. Wada S., Henmi N., Ayoyama H., Osada H., Simokohbe A., "A Six-Degrees-of-Freedom Fine Motion Mechanism," JSPE, Vol. 58 No. 06, pp. 135-1040., 1992.
39. Otsuka J., Ilda N., Aoki Y., "Ultra-Precision Positioning by Using Lead Screw Drive(3rd Report)," JSPE Vol.59 No.10, pp. 1665-1661., 1993.
40. Waggener H. A., Peters D. W., Chen G., Rose C. M., Fowlis D. C., "Preliminary Analysis of Electron-Beam Positioning errors in Lepton EBES4," V. Vac. Sci. Technol. B 9(6), pp. 3033-3038., 1991.
41. Ogata K., " Moden Control Engineerig," Huijoungdang pub., pp. 660-865., 1993.
42. "ML10 Renishaw User Manual," 2001.
43. Eric B. Becker, Graham F. Carey, J. Tinsley Oden, "Finite Elements An Introduction," Texas Institute for Computational Mechanics The University of Texas at Austin, Vol. 1, pp. 242-245.
44. MARC Analysis Research Corporation manual, VOLUME A, VOLUME B, VOLUME C, VOLUME D, 1994.
45. Zienkiewicz O. C., Taylor R. L., "The Finite Element Method : Volume1 Basic Formulation and Linear Problems", McGAW-HILL BOOK Co., 1989.
46. Nicolae L., Jeffrey S.N. Paine, Edward O'Malley, Samuelson M., "Parabolic and Hyperbolic Flexure Hinges: Lexibility, Motion Precision And Stress Characterization Based on Compliance Closed-Form Equations," Precision

Engineering Journal of the International Societies for Precision Engineering and Nanotechnology, Vol. 26, pp. 183-192., 2002.

47. Paros J. M, Weisbord L. "How to Design Flexure Hinges Machine Design," pp. 151-156., 1965.
48. Ragulskis K. M., Arutunian M. G., Kochikian A. V., Pogosian M. Z., "A Study of Fillet Type Flexure Hinges and Their Optimal Design," Vibr Eng Vol. 3, pp. 447-452., 1989.
49. Smith T. S., Badami V. G., Dale J. S., Xu Y. "Elliptical Flexure Hinges" Rev Sci Instrum, Vol. 68 No. 3, pp. 1474-1483., 1997.
50. Smith S. "Flexures: Elements of Elastic Mechanisms". New York: Gordon and Breach Science, 2000.
51. Lobontiu N., Paine J. S. N., Garcia E, Goldfarb M. "Corner-Filleted Flexure Hinges" ASME J Mech Design, Vol. 123, 2001.
52. Xu W., King T. G., "Flexure Hinges for Piezo-Actuator Displacement Amplifiers: Flexibility, Accuracy and Stress Considerations," Precision Eng Vol. 19 No. 1, pp. 4-10., 1996.
53. Ryu J. W., Gweon D. G.. Error Analysis of a Flexure Hinge Mechanism Induced by Machining Imperfection," Precision Eng, Vol. 21, pp. 83-89., 1997.
54. Lobontiu N., Paine J. S. N., Garcia E., Goldfarb M. "Design of Symmetric Conic-Section Flexure Hinges Based on Closed-form Compliance Equations," Mechanism Machine Theory, 2002.
55. Peterson R. E., "Stress Concentration Factors," New York Wiley, 1974.
56. Pilkey W. D. "Peterson's Stress Concentration Factors," New York: Wiley, 1997.
57. Lee C.W., "3-Axis Dual-Servo Control of an XYTeata-Stage for Ultra-Precision Positioning," Ph.D Docter Theses of KAIST, 1997.
58. Ledsma R., Ma Z, D., Hulbert G., and Wineman A., "onlinear Viscoelastic Bushing Element in Multibody Dynamics," Computational Mechanics, Vol. 17 No. 5, Mac.,

pp. 287-296., 1996.

59. Bohn G., Steinmetz G., "The Electromagnetic Levitation and Guidance Technology of the TRANSRAPID Test Facility Emsland," IEEE Transactions of Magnetics, Vol. MAG-20 No. 5, pp. 1666~1671., 1984.
60. Iwasaki M. and Matsui N. , "Observer-Based Nonlinear Friction Compensation in Servo Drive System," Proc. of IEEE 5th International Workshop on AMC, pp. 344-348., 1996.
61. Johnson C. T., Lorenz R. D., "Experimental Identification of Friction and Its Compensation in Precise, Position Controlled Mechanism," IEEE Transaction on Industry Application, Vol. 28 No. 6, pp. 1392-1398., 1992.
62. Patnaik B. R., Heppler G. R., Wang D., "Stability Analysis of Piezoelectric Vibration Controller for an Euler-Bernoulli Beam," Proceeding of the American Control Conference, San Francisco, 1993.
63. Fanson J. L., Caughey T. K., "Positive Position Feedback Control for Large Space Structure," AIAA Journal, Vol. 28 No. 4, 1990.
64. Sim E. S., Lee S. W. "Active Vibration Control of Flexible Structures with Acceleration Feedback," Journal of Guidance and Control, Vol. 16 No. 2, 1992.
65. Clark R. L., Flemming M. R., Fuller C. R., " Piezoelectric Actuators for Distributed Vibration Excitation of Thin Plates: A Comparison Between Theory and Experiment," ASME Trans. Journal of Vibration and Acoustics, pp. 332-339., 1993.
66. Falangas E. T., Dcoorack J., Koshigoe A., "Controlling Plate Vibration Using Piezoelectric Actuator," IEEE Control System Magazine, Vol. 14 No. 4, pp. 34-41., 1994.
67. Lee C. K., Moon F. C., "Modal Sensors/Actuators," ASME Trans. Journal of Applied Mechanics, Vol. 57, pp. 434-441., 1990.
68. Gu R., Clark R. L., Fuller C. R., "Piezoelectric Actuators for Experiments on

Active Control of Plate Vibration Using Piezoelectric Actuators and Polyvinylidence Fluoride (PVDF) Modal Sensors," ASME Trans. Journal of Vibration and Acoustics, Vol. 116, pp. 303-308., 1994.

69. Inniss D. C., Williarms T., "Sensitivity of the Zeros of Flexible Structure to Sensor and Actuator Location," Proceeding of the 32nd Conference on Decision and Control, San Antonlo, Texas, pp. 1402-1403., 1993.
70. Dosch J. J., Inman D. J., "A Self-Sensing Piezoelectric Actuator for Collocated Control," Journal of Intell. Mater. Syst. and Struct, Vol. 3, 1992.
71. ADAMS User Manual, Mechanical Dynamics, Inc., Ann Arbor MI, 2001.
72. Using Matlab, The MathWorks, Inc. Dec. 2001.
73. Using SIMULINK, The MathWorks, Inc. Dec. 2001.
74. Real Time Workshop, The MathWorks, Inc. Dec. 2001.
75. Kwac L. K., "A Study on the Simulation and Control Performance Estimation of Ultra- Precision Positioning Apparatus," Theses of Chosun University Master, 2000
76. Debra D. et al, "Vibration isolation of precision machine tools and instruments," Annals of the CIRP Vol. 41 No. 2, pp. 711., 1992.
77. Ashkin A., "Acceleration and trapping of particles by radiation pressure," Phys. Rev. Lett. Vol 24, pp 156, 1970.
78. Bar-Cohen A., Kraus A., "Advanced in thermal modeling of electronic components and systems," ASME Press, Vol 3, 1993.
79. http://www.kimm.re.kr/
80. http://www.iea.re.kr/
81. http://scala.iae.re.kr/
82. http://pem.kaist.ac.kr/bupe/
83. http://www.kbsi.re.kr/
84. http://www.archforum.com/

85. http://www.postech.edu/

86. http://www.kordic.re.kr/~trend

APPENDIX A : Drawing of UPCU

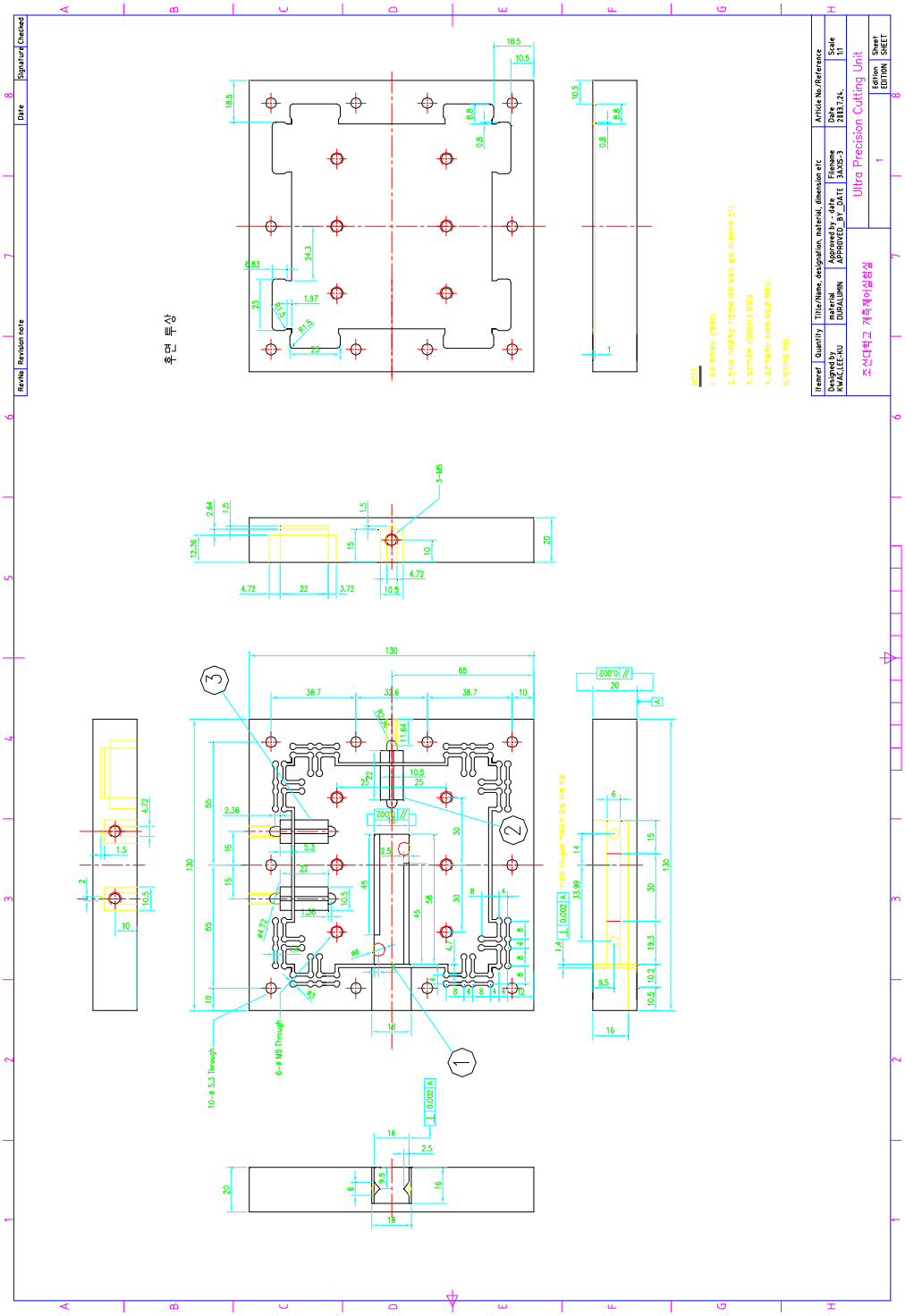
조선대학교 계측제어실험실
Ultra Precision Cutting Unit
측면 투상
10-ø 5.3 Through
6-ø M5 Through
3-M5
NOTE

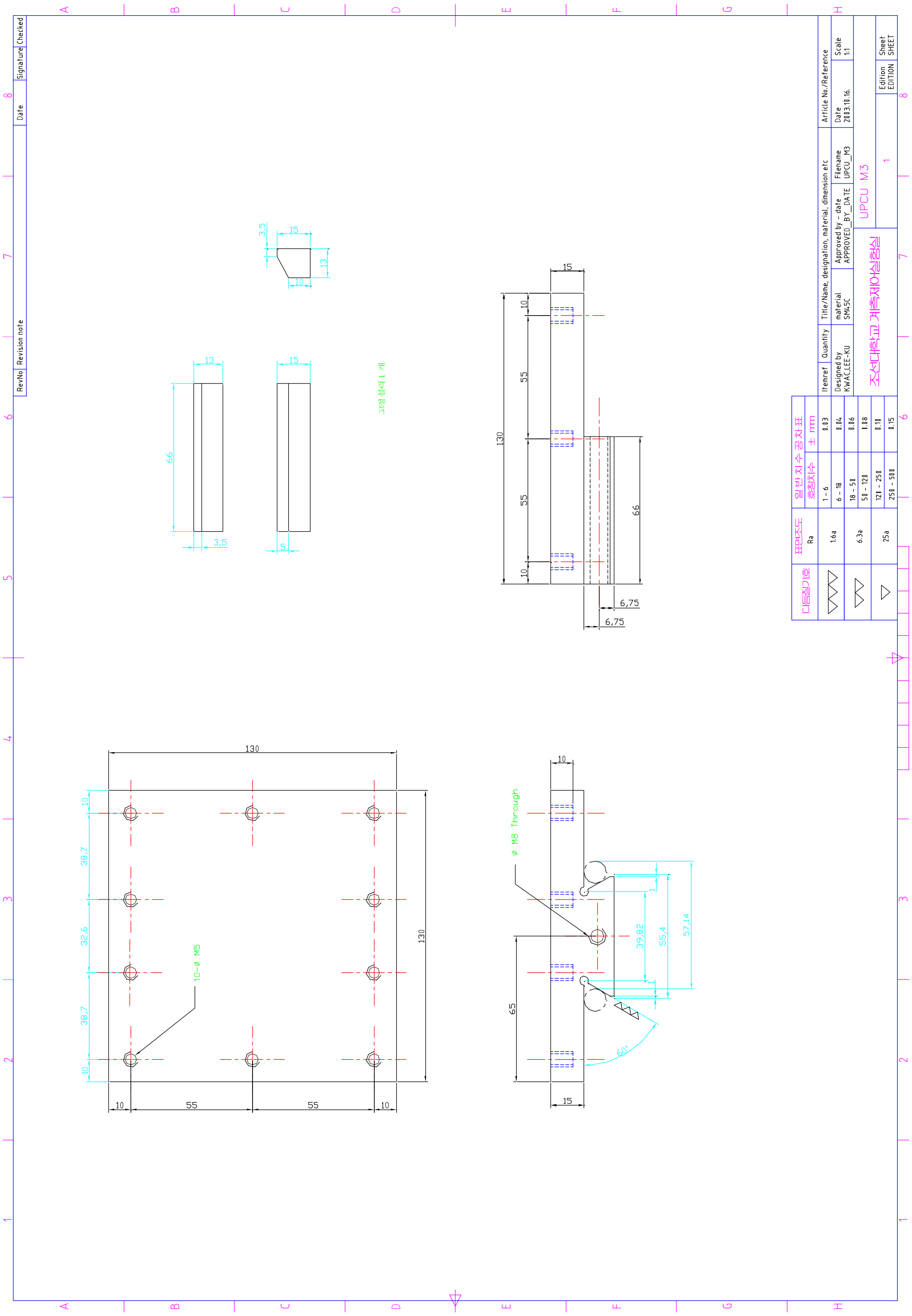

조선대학교 계측제어실험실
UPCU M3
Itemref
Quantity
Title/Name, designation, material, dimension etc
Article No./Reference
Designed by
KWAC,LEE-KU
material
SM45C
Approved by - date
APPROVED_BY_DATE
Filename
UPCU_M3
Date
2003.10.16.
Scale
1:1
Edition
EDITION
Sheet
SHEET
다듬질기호
표면조도
Ra
1.6a
6.3a
25a
일반치수 공차표
호칭치수
± mm
1 - 6
6 - 18
18 - 50
50 - 120
121 - 250
250 - 500
0.03
0.04
0.06
0.08
0.10
0.15
RevNo
Revision note
Date
Signature
Checked
10-ø M5
ø M8 Through

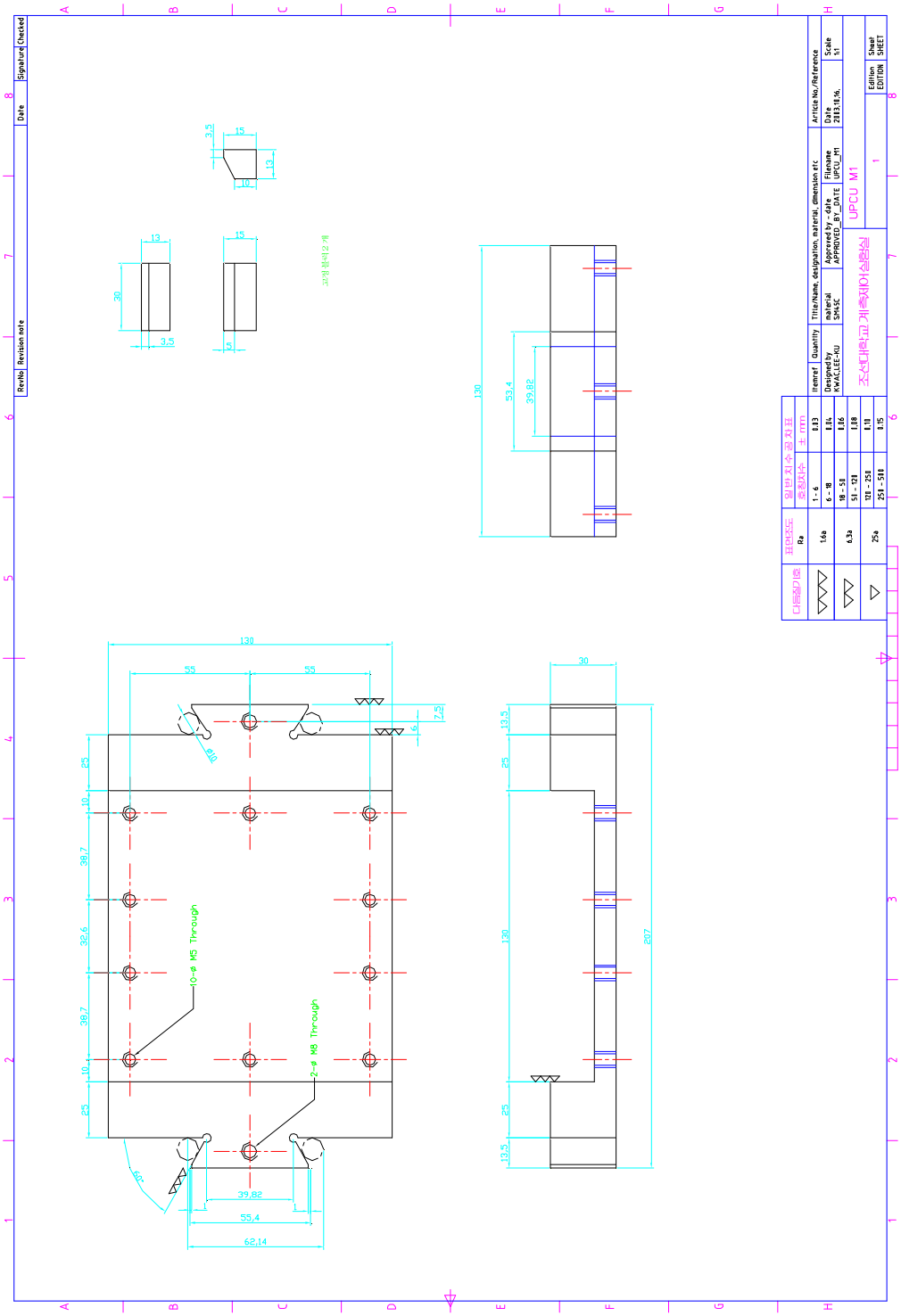
조선대학교 계측제어실험실
UPCU M1
10-ø M5 Through
2-ø M8 Through
130
55
55
7.5
6
10
25
10
38.7
32.6
38.7
10
25
30
13.5
25
130
207
13.5
39.82
55.4
62.14
53.4
39.82
130
13
15
3.5
13
15
10
38
3.5
5
3.5
15
13
10
고정 볼넛 2개

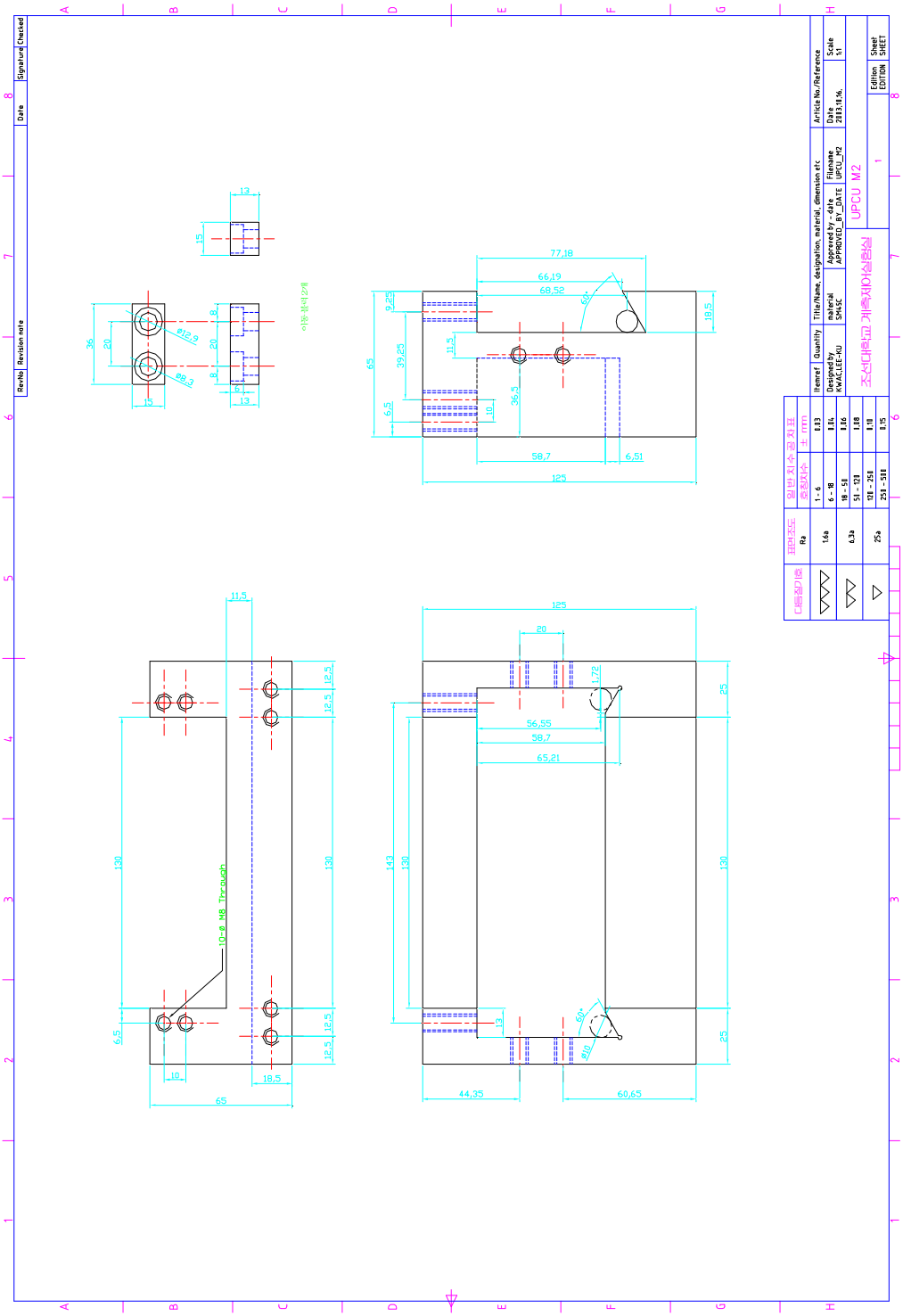
UPCU M2
조선대학교 계측자동화실험실
10-ø M8 Through

APPENDIX B : Cutting Force in Turning

Cutting Force in Turning

※ Effect element of Cutting Force in Turning

- Material of workpiece
- Material of cutting tool
- Geometrical shape of cutting tool
- Cutting oil

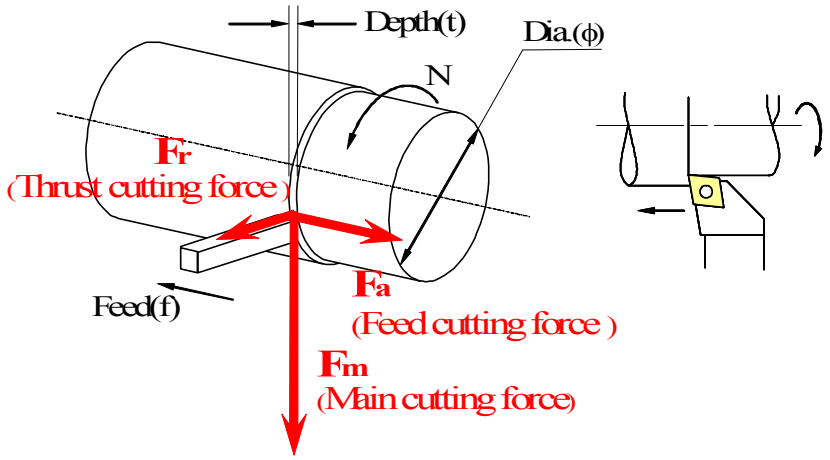

※ 3 Component Cutting Force

☑ Main Cutting Force Component (F_m)

$F_m = Ks \times t \times F$ (kg)

☑ Feed Cutting Force Component (F_a)

$F_a = 0.2 \times F_m$ [kg]

☑ Thrust Cutting Force Component (F_r)

$F_r = 0.3 \times F_m$ [kg]

Ks : Specific cutting resistance, t : cutting depth(mm),

f = F/N [mm/rev], F : feed (mm/min)

☑ Total Power Consumption

$N = N_l + N_e + N_f$

N_l = Loss power, N_e = Effective cutting power, N_f = Feed power

☑ Cutting Speed

$V = (\pi \times D \times N) / 1{,}000$ [m/min]

V : cutting speed (m/min), D : Diameter of workpiece (mm), N : rpm

☑ Feed per Revolution

$f = \ell / N$ [mm/rev]

f : feed (mm/rev), ℓ: cutting depth per minute (mm/min)

☑ . Cutting Time

$T = L / \ell$ [min]

T : Cutting time(min), L : Workpiece length (mm)

☑ Cutting Power

$N_e = (t \times f \times V \times Ks) / (6120 \times \eta)$ [kw]

$H_e = (N_e / 0.75)$ [Hp]

t : Cutting depth (mm), N_e : Cutting power [kw],

Ks : Specific cutting resistance(kg/㎟), H_e : Cutting power (Hp),

η : Mechanical efficiency (0.7~0.8)

※ Feed according to workpiece diameter

80 rpm (V = 150 M/min)												
D(Φ)	M/min	Ks	t	f	t	f	t	f	t	f	t	f
600	151	238	5	0.07	4	0.08	3	0.11	2	0.16	1	0.33
550	138	238	5	0.07	4	0.09	3	0.12	2	0.18	1	0.35
500	126	238	5	0.08	4	0.10	3	0.13	2	0.20	1	0.39
450	113	238	5	0.09	4	0.11	3	0.14	2	0.22	1	0.43
400	100	238	5	0.10	4	0.12	3	0.16	2	0.24	1	0.49
350	88	238	5	0.11	4	0.14	3	0.19	2	0.28	1	0.56
300	75	238	5	0.13	4	0.16	3	0.22	2	0.33	1	0.65
270	68	238	5	0.14	4	0.18	3	0.24	2	0.36	1	0.72
240	60	238	5	0.16	4	0.20	3	0.27	2	0.41	1	0.81
210	53	238	5	0.19	4	0.23	3	0.31	2	0.46	1	0.93
180	45	238	5	0.22	4	0.27	3	0.36	2	0.54	1	1.08
150	38	238	5	0.26	4	0.33	3	0.43	2	0.65	1	1.30
120	30	238	5	0.33	4	0.41	3	0.54	2	0.81	1	1.63
90	23	238	5	0.43	4	0.54	3	0.72	2	1.08	1	2.17
60	15	238	5	0.65	4	0.81	3	1.08	2	1.63	1	3.25
30	8	238	5	1.30	4	1.63	3	2.17	2	3.25	1	6.50

160 - 600 rpm												
D(Φ)	M/min	Ks	t	f	t	f	t	f	t	f	t	f
600	1130	238	5	0.10	4	0.13	3	0.17	2	0.25	1	0.50
550	1036	238	5	0.11	4	0.14	3	0.18	2	0.27	1	0.55
500	942	238	5	0.12	4	0.15	3	0.20	2	0.30	1	0.60
450	848	238	5	0.13	4	0.17	3	0.22	2	0.33	1	0.67
400	754	238	5	0.15	4	0.19	3	0.25	2	0.38	1	0.75
350	659	238	5	0.17	4	0.21	3	0.29	2	0.43	1	0.86
300	565	238	5	0.20	4	0.25	3	0.33	2	0.50	1	1.00
270	509	238	5	0.22	4	0.28	3	0.37	2	0.56	1	1.11
240	452	238	5	0.25	4	0.31	3	0.42	2	0.63	1	1.25
210	396	238	5	0.29	4	0.36	3	0.48	2	0.71	1	1.43
180	339	238	5	0.33	4	0.42	3	0.56	2	0.83	1	1.67
150	283	238	5	0.40	4	0.50	3	0.67	2	1.00	1	2.00
120	226	238	5	0.50	4	0.63	3	0.83	2	1.25	1	2.50
90	170	238	5	0.67	4	0.83	3	1.11	2	1.67	1	3.33
60	113	238	5	1.00	4	1.25	3	1.67	2	2.50	1	5.00
30	57	238	5	2.00	4	2.50	3	3.33	2	5.00	1	10.0

1500 rpm												
D(Φ)	M/min	Ks	t	f	t	f	t	f	t	f	t	f
600	2826	238	5	0.03	4	0.04	3	0.05	2	0.08	1	0.15
550	2591	238	5	0.03	4	0.04	3	0.05	2	0.08	1	0.16
500	2355	238	5	0.04	4	0.05	3	0.06	2	0.09	1	0.18
450	2120	238	5	0.04	4	0.05	3	0.07	2	0.10	1	0.20
400	1884	238	5	0.05	4	0.06	3	0.08	2	0.11	1	0.23
350	1649	238	5	0.05	4	0.06	3	0.09	2	0.13	1	0.26
300	1413	238	5	0.06	4	0.08	3	0.10	2	0.15	1	0.30
270	1272	238	5	0.07	4	0.08	3	0.11	2	0.17	1	0.33
240	1130	238	5	0.08	4	0.09	3	0.13	2	0.19	1	0.38
210	989	238	5	0.09	4	0.11	3	0.14	2	0.21	1	0.43
180	848	238	5	0.10	4	0.13	3	0.17	2	0.25	1	0.50
150	707	238	5	0.12	4	0.15	3	0.20	2	0.30	1	0.60
120	565	238	5	0.15	4	0.19	3	0.25	2	0.38	1	0.75
90	424	238	5	0.20	4	0.25	3	0.33	2	0.50	1	1.00
60	283	238	5	0.30	4	0.38	3	0.50	2	0.75	1	1.50
30	141	238	5	0.60	4	0.75	3	1.00	2	1.50	1	3.00

3000 rpm												
D(Φ)	M/min	Ks	t	f	t	f	t	f	t	f	t	f
600	5652	238	5	0.01	4	0.02	3	0.02	2	0.03	1	0.07
550	5181	238	5	0.01	4	0.02	3	0.02	2	0.04	1	0.07
500	4710	238	5	0.02	4	0.02	3	0.03	2	0.04	1	0.08
450	4239	238	5	0.02	4	0.02	3	0.03	2	0.05	1	0.09
400	3768	238	5	0.02	4	0.03	3	0.03	2	0.05	1	0.10
350	3297	238	5	0.02	4	0.03	3	0.04	2	0.06	1	0.12
300	2826	238	5	0.03	4	0.03	3	0.05	2	0.07	1	0.14
270	2543	238	5	0.03	4	0.04	3	0.05	2	0.08	1	0.15
240	2261	238	5	0.03	4	0.04	3	0.06	2	0.09	1	0.17
210	1978	238	5	0.04	4	0.05	3	0.06	2	0.10	1	0.19
180	1696	238	5	0.05	4	0.06	3	0.08	2	0.11	1	0.23
150	1413	238	5	0.05	4	0.07	3	0.09	2	0.14	1	0.27
120	1130	238	5	0.07	4	0.09	3	0.11	2	0.17	1	0.34
90	848	238	5	0.09	4	0.11	3	0.15	2	0.23	1	0.45
60	565	238	5	0.14	4	0.17	3	0.23	2	0.34	1	0.68
30	283	238	5	0.27	4	0.34	3	0.45	2	0.68	1	1.36

※ Cutting Torque (SM45C)

No.	D	V	N	T (Kg.m) Depth = 1.0 mm									
1	600	150	80	7.1	14.3	21.4	28.6	35.7	42.8	50.0	57.1	64.3	71.4
2	550	150	87	6.5	13.1	19.6	26.2	32.7	39.3	45.8	52.4	58.9	65.5
3	500	150	95	6.0	11.9	17.9	23.8	29.8	35.7	41.7	47.6	53.6	59.5
4	450	150	106	5.4	10.7	16.1	21.4	26.8	32.1	37.5	42.8	48.2	53.6
5	400	150	119	4.8	9.5	14.3	19.0	23.8	28.6	33.3	38.1	42.8	47.6
6	350	150	136	4.2	8.3	12.5	16.7	20.8	25.0	29.2	33.3	37.5	41.7
7	300	150	159	3.6	7.1	10.7	14.3	17.9	21.4	25.0	28.6	32.1	35.7
8	250	150	191	3.0	6.0	8.9	11.9	14.9	17.9	20.8	23.8	26.8	29.8
9	200	150	239	2.4	4.8	7.1	9.5	11.9	14.3	16.7	19.0	21.4	23.8
10	150	150	318	1.8	3.6	5.4	7.1	8.9	10.7	12.5	14.3	16.1	17.9
11	100	150	477	1.2	2.4	3.6	4.8	6.0	7.1	8.3	9.5	10.7	11.9
12	50	150	955	0.6	1.2	1.8	2.4	3.0	3.6	4.2	4.8	5.4	6.0
13	16	150	2984	0.2	0.4	0.6	0.8	1.0	1.1	1.3	1.5	1.7	1.9
Feed			1.0	0.1	0.2	0.3	0.4	0.5	0.6	0.7	0.8	0.9	1.0
Area				0.1	0.2	0.3	0.4	0.5	0.6	0.7	0.8	0.9	1.0

No.	D	V	N	T (Kg.m) Depth = 2.0 mm									
1	600	150	80	14.3	28.6	42.8	57.1	71.4	85.7	100.0	114.2	128.5	142.8
2	550	150	87	13.1	26.2	39.3	52.4	65.5	78.5	91.6	104.7	117.8	130.9
3	500	150	95	11.9	23.8	35.7	47.6	59.5	71.4	83.3	95.2	107.1	119.0
4	450	150	106	10.7	21.4	32.1	42.8	53.6	64.3	75.0	85.7	96.4	107.1
5	400	150	119	9.5	19.0	28.6	38.1	47.6	57.1	66.6	76.2	85.7	95.2
6	350	150	136	8.3	16.7	25.0	33.3	41.7	50.0	58.3	66.6	75.0	83.3
7	300	150	159	7.1	14.3	21.4	28.6	35.7	42.8	50.0	57.1	64.3	71.4
8	250	150	191	6.0	11.9	17.9	23.8	29.8	35.7	41.7	47.6	53.6	59.5
9	200	150	239	4.8	9.5	14.3	19.0	23.8	28.6	33.3	38.1	42.8	47.6
10	150	150	318	3.6	7.1	10.7	14.3	17.9	21.4	25.0	28.6	32.1	35.7
11	100	150	477	2.4	4.8	7.1	9.5	11.9	14.3	16.7	19.0	21.4	23.8
12	50	150	955	1.2	2.4	3.6	4.8	6.0	7.1	8.3	9.5	10.7	11.9
13	16	150	2984	0.4	0.8	1.1	1.5	1.9	2.3	2.7	3.0	3.4	3.8
Feed			2.0	0.1	0.2	0.3	0.4	0.5	0.6	0.7	0.8	0.9	1.0
Area				0.2	0.4	0.6	0.8	1.0	1.2	1.4	1.6	1.8	2.0